



HHS Public Access

Author manuscript

Prog Opt. Author manuscript; available in PMC 2021 August 04.

Published in final edited form as:

Prog Opt. 2010 ; 55: 199–283. doi:10.1016/b978-0-444-53705-8.00004-7.

Adaptive Lens

Guoqiang Li

University of Missouri – St. Louis, College of Optometry, Department of Physics and Astronomy,
St. Louis, USA

1. INTRODUCTION

Adaptive or varifocal lenses with variable focusing powers have attracted much attention in the last two decades because of their wide applications in vision care, consumer electronics such as digital cameras, aberration correction, optical interconnects, and three-dimensional biomedical imaging. The focal power of an optical system is usually changed by nonlinear movement of lenses with spherical or cylindrical powers along the optical axis and such a system consists of several lens components (Back & Lowen, 1954, 1958; Bergstein, 1958). It requires mechanic translation and might be bulky. Detailed discussion of optical zoom lenses is not covered here. In the late 1960s, Luis Alvarez and William Humphrey (Alvarez, 1967; Alvarez, 1978; Alvarez & Humphrey, 1970), and Adolf Lohmann (Lohmann, 1964) invented independently new types of varifocal composite lenses based on lateral rather than longitudinal shifts of two lenses with conjugate, rotationally asymmetric, aspheric surfaces. The Alvarez lens and the Lohmann lens contain two transmissive refractive plates, each having a plano surface and a surface shaped in a two-dimensional cubic profile. The sag or the z coordinate of the cubic-type surface can be represented by the following general expression

$$z_1 = A_x x^3 + A'_x x^2 y + A_y y^3 + A'_y x y^2 + B x^2 + C x y + D x + E, \quad (1.1)$$

where A_x , A'_x , A_y , A'_y , B , C , D , and E are the coefficients of the “ x^3 ,” “ $x^2 y$,” “ y^3 ,” “ $x y^2$,” “ x^2 ,” “ $x y$,” and “ x ” terms, respectively, while “ E ” is a term for constant thickness. In the case that the noncubic faces are planar surfaces, the second-order terms of Equation (1.1) (coefficients B , C , and D) are usually set to zero.

Alvarez lens satisfies: $A'_x = A_y = 0$, and Lohmann lens: $A'_x = A'_y = 0$.

Figure 1 illustrates two configurations for the Alvarez and Lohmann lenses (Barbero, 2009): the two cubic surfaces facing outward (the upper part) and the two cubic surfaces facing inward (the lower part). The two cubic surfaces are made to be the inverse of each other, so that when both plates are placed with their vertices on the optical axis, the induced phase variations cancel out and there is no power. This state is also called a “do-nothing machine” (Caulfield, 2002). However, if the two plates undergo a relative lateral translation, a phase variation is induced that is the differential of the cubic surface profiles, resulting in a quadratic phase profile – or, in other words, optical power. Relative movements in the x or y direction induce cylindrical power independently in orthogonal directions. Combined movements can produce circular, elliptical, or cylindrical phase profiles. For example, if

both lens components of the Alvarez lens are moved by a distance Δ in the opposite directions along the x coordinate and assume $A_x = A'_y = A$, it can be deduced (using Equation (1.1)) that all terms containing “ x ” and “ y ” cancel out leaving only the $(x^2 + y^2)$ term and some constants. The total thickness is equal to $2A\sqrt{(x^2 + y^2)}$, indicating that symmetrical movement of the two plates results in a varifocal spherical lens and the focal length is a function of the coefficient “ A ” and the displacement “ Δ ”. Based on the property of a thin lens in phase transformation (Goodman, 2005), the paraxial focal length can be written as

$$f = \frac{1}{4A\Delta(n - n')}, \quad (1.2)$$

where n is the refractive index of the lens material and n' is the refractive index of the surrounding medium. It should be noted that for the configuration with the cubic surfaces facing inward, there needs to be a space between the two components to avoid collision during the shifts.

The Alvarez lens has been applied to Humphrey analyzer (Humphrey, 1976), scanning microscope (Rege, Tkaczyk, & Descour, 2004), intraocular accommodative lens (Simonov, Vdovin, & Rombach, 2006), and spectacle lenses (Spivey, 2008). Recent analysis (Barbero, 2009) shows that for the same power and lateral shifts, the Lohmann lens is thinner and provides better optical performance. It also shows that the inner cubic surface configuration provides slightly better optical performance. Recent advances in microfabrication technologies allow us to make both refractive and diffractive Alvarez or Lohmann lenses.

In the late 1960s, Lohmann and Paris also described varifocal spherical zone plates as a moiré effect created by translations and rotations of the basic grids, as well as varifocal cylindrical zone plates formed by translations (Lohmann & Paris, 1967). By adding a linear carrier frequency to the basic grids described by curves of cube functions, the focusing power can be varied over a considerable range by relative translation of the grids, and it increases the clarity of moiré fringes by making their period more uniform (Burch & Williams, 1977; Lohmann, 1970). Elliptical and hyperbolic moiré patterns can be generated too. For binary amplitude basic grids, the light efficiency of the moiré diffractive optical elements is low ($1/\pi^4 \approx 1.03\%$) and it can be increased to $16/\pi^4 (\approx 16.43\%)$ if binary phase basic grids are used. Further improvement of the light efficiency to the values up to 100% by superposition of two conjugated kinoforms was first proposed by Lohmann (1970) and then realized experimentally (Barton et al., 2000; Kołodziejczyk & Jaroszewicz, 1993). Equilateral hyperbolic zone plates with variable focal length has been formed as moiré patterns by a mutual rotation of two identical basic grids by a proper choice of the basic grid's particular form (Jaroszewicz, Kołodziejczyk, Mira, Henao, & Bará, 2005). Advantages of this approach include a constant aperture of the created element during the mutual movement of basic grids, lack of aberrations because of their undesired mutual lateral displacements and high-diffraction efficiency of the binary phase version. Very recently optical power can be adjusted continuously by a mutual rotation of one diffractive optical element with respect to the other without eccentric displacements (Bernet & Ritsch-Marte, 2008).

Although the Alvarez and Lohmann lenses use only two conjugate lenses and the relative movement is linear and simpler in comparison with the traditional varifocal lens system based on longitudinal movements of the lenses, it is attractive to develop single-element adaptive lenses. There are two kinds of adaptive lenses: liquid crystal (LC) lens and liquid lens. The former is based on tuning the refractive index of the liquid crystal, and the latter is based on changing the shape of the liquid. These two kinds of adaptive lenses and their applications are reviewed below. Although the majority of the articles on adaptive lenses are covered here, the list is by no means complete.

2. ADAPTIVE LIQUID CRYSTAL LENS

2.1. Liquid Crystal Cell

Liquid crystals are mesophases between isotropic liquids and crystalline solids (Yang & Wu, 2006). They can flow and take the shape like regular liquids and exhibit optical birefringence like crystalline solids. The constituents are elongated rod-like or disc-like organic molecules. Nematic phase (Figure 2(a)) is the most common LC phase, and the molecules have orientational order but no positional order. Nematic LC cells consisting of rod-like molecules are most suited for phase modulation and high transmission of light. Orientational order is the most important property of the LCs. The orientation of the rod-like molecule can be represented by a unit vector \vec{a} , which is along the long axis of the molecule. It has preferred direction, and the average directions of the long axis of the rod-like molecules are parallel to each other at the macroscopic scale. The average direction of the long molecular axis is denoted by the unit vector \vec{n} and called LC director. There is no preferred direction for the short axes and hence the nematic LC is usually optical uniaxial. Because of this feature, nematic LC possesses optical anisotropy property manifested by different indices of refraction. The birefringence is defined by $n = n_e - n_o$, where n_e and n_o are refractive indices for the extraordinary and ordinary beams, respectively. The electrical properties of the LC are represented by the dielectric permittivities parallel and perpendicular to the long molecular axis \vec{a} , ϵ_{\parallel} , and ϵ_{\perp} . The difference $\epsilon = \epsilon_{\parallel} - \epsilon_{\perp}$ is the dielectric anisotropy, which can be either positive or negative. LCs respond to the rms value of an applied AC field. The elastic properties of the LC are characterized by the elastic constants K_{11} , K_{22} , and K_{33} for splay, twist, and bend, respectively, and they are temperature dependent.

Homogeneously aligned nematic LCs with positive dielectric anisotropy are most widely used for tunable devices based on phase modulation. Figure 2(b) shows a typical LC cell of this kind. LCs are sandwiched between two substrates coated with transparent conductive thin films such as indium tin oxide (ITO) and an alignment layer. The alignment layer can be polyimide, polyvinyl alcohol (PVA), or nylon. In the absence of external electrical fields, orientation of the LC in the cell is determined by the anchoring condition of the alignment layer. By rubbing the surface of the alignment layer, microgrooves along the rubbing direction can be generated, and the LCs will be homogeneously aligned along the grooves. The LC cell is assembled with antiparallel configuration of the alignment layer. At the boundary between the LC and the alignment layer, pretilt angles of a few degrees can be generated. An LC cell is usually driven by an ac electric field in the lower kHz regime.

When an external electrical field is applied to the two ITO electrodes, the LC will reorient because of their dielectric anisotropies. For LCs with positive dielectric anisotropy ($\epsilon > 0$), they tend to align parallel to the electrical field. For LCs with negative dielectric anisotropy ($\epsilon < 0$), they tend to align perpendicular to the electrical field. The field-induced reorientation is called *Freedericksz transition*. The reorientation of the LC happens when the amplitude of the applied voltage is higher than the threshold voltage given by

$$V_{\text{th}} = dE_{\text{th}} = \pi \sqrt{\frac{K_{11}}{\epsilon_0 \Delta \epsilon}}, \quad (2.3)$$

where E_{th} is the threshold field and ϵ_0 is the permittivity of free space. The orientation of the LC director in the applied electrical field determines the electric energy, which is part of the total free energy. The total free energy is the summation of the electric energy and the elastic energy. The equilibrium director configuration is obtained by minimizing the total free energy of the system. Finite difference method or finite-element method can be used to model the electric field distribution, and the LC director map across the LC cell based on the continuum theory. Details for the analysis are not discussed here. One important parameter for LC cells is the response time, including the turn-on time and the turn-off time. In a first approximation, the turn-on time can be approximated as

$$\tau_{\text{on}} = \frac{\gamma_1 d^2}{K \pi^2}, \quad (2.4)$$

where γ_1 is the rotational viscosity of the LC. And the turn-off time is

$$\tau_{\text{off}} = \frac{\gamma_1}{K} \frac{d^2}{\pi^2 [(V/V_{\text{th}})^2 - 1]}, \quad (2.5)$$

where V is the applied voltage. Equations (2.4) and (2.5) imply that the response and recovery time of LC cell is proportional to the square of the thickness of the cell. Typical nematic LC cells have a response time in the order of millisecond.

As shown in Figure 2(b), the original orientation of the liquid crystal molecule is determined by the buffing direction. The long axis (optic axis) of the liquid crystal molecule is close to the y axis (vertical direction in the figure). Light is normally incident to the LC cell and propagates along the z direction. When an appropriate voltage is applied, the LC director is tilted in the YOZ plane by an angle θ from the y axis. The LC director pattern is symmetric in the z direction. Based on the ellipsoid of the wave vector or the ellipsoid of the refractive index (Born & Wolf, 1999, Figure 2(c)), the effective refractive index of the extraordinary beam (with a polarization state parallel to the y axis) is given by

$$n'_e(\theta) = \frac{n_o n_e}{\sqrt{(n_e^2 \sin^2 \theta + n_o^2 \cos^2 \theta)}}. \quad (2.6)$$

For an extraordinary beam, initially it has the maximum refractive index n_e . With the increase of the applied voltage, the tilt angle θ at a particular location (r, z) increases and the effective refractive index n'_e decreases, and when a saturation voltage is reached, the optic axis of the molecule is aligned horizontally, and the effective refractive index of n'_e reaches the minimum and equals to n_0 . The refractive index for the ordinary beam (horizontally polarized) is always the same. So the electro-optic effect modulates the effective refractive index of the extraordinary beam. Because the effective refractive index n'_e is a spatially variant as a function of r and z , at a particular location with radius r from the center of the device, the average refractive index for the extraordinary beam is

$$n_{e_avg} = \frac{1}{d} \int_0^d n'_e(\theta(r, z)) dz, \quad (2.7)$$

and the average birefringence is given by

$$\Delta n_{avg} = \frac{1}{d} \int_0^d n'_e(\theta(r, z)) dz - n_0. \quad (2.8)$$

The phase retardation between the extraordinary beam and the ordinary beam takes the form

$$\Delta\phi(r) = k \left[\int n'_e(\theta) dz - n_0 d \right]. \quad (2.9)$$

2.2. Liquid Crystal Lens

The concept of LC adaptive lens was first published by Bricot, Hareng, and Spitz (1977) in their patent, where LCs are filled in the refractive lens chamber and the substrate has no power. Two uniform conductive electrodes and alignment layers are coated on the inner surfaces of the lens chamber, and the LCs are homogeneously aligned by rubbing the surfaces of the alignment layers. The LC lens power is determined by the effective refractive index. In 1979, Sato reported LC composite lens by immersing LC into a lens-shaped cell as shown in Figure 3 (Sato, 1979). The glass lens substrate can be either plano-convex or plano-concave shape, and the LC cell is processed in the same manner. In both cases, the focal length of the LC lens is given by

$$f_{LC} = \frac{R}{n_{e_eff} - 1}, \quad (2.10)$$

where R is the radius of the curved surface of the LC lens. Assuming n_{e_eff} can be tuned from n_e to n_0 for the extraordinary beam, the focal length of the LC lens can be varied from $f_e = R/(n_e - 1)$ to $f_o = R/(n_0 - 1)$, and the focal length of the composite lens equals to

$$f = \left(\frac{1}{f_{LC}} + \frac{1}{f_{glass}} \right)^{-1}. \quad (2.11)$$

These two LC lens structures are relatively simple. However, there are several disadvantages. The thickness of the LC lens becomes very large at the center of the plano-convex lens or the peripheral region of the plano-concave lens, and this increase in thickness results in very slow speed of the response and recovery properties. For example, for a typical plano-convex LC lens with an aperture of 20 mm and a focal length of 20 cm, the thickness at the center is about 0.5 mm. As a result of the large variation of the thickness of the LC layer from the center to the periphery, the electric field inside the LC lens is not uniform, and thus, the effective refractive index is not uniform across the lens aperture. This means that the focal length at the center may be different from that at the periphery. Furthermore, the transmission of the lens is reduced by absorption and scattering of the light when the LC lens is thick. These issues can be overcome by using a Fresnel lens as the substrate for the LC lens (Fowler & Pateras, 1990; Sato, Sugiyama, & Sato, 1985). If the thickness of the LC lens is reduced by 10 times, the response time can be improved by two orders of magnitude.

Since then various adaptive LC lenses have been demonstrated by using different techniques to generate the phase profile for the lens. The phase profile can be induced by homogeneous LC but inhomogeneous electric field using discrete electrodes, hole-patterned electrode, resistive control electrode, spherical-shaped electrode, or homogeneous electric field but inhomogeneous LC based on polymer/LC composites, patterned or hybrid alignment of LCs on the cell walls. By using inhomogeneous electric field and inhomogeneous LCs, polarization-independent lenses are made possible.

2.3. Refractive Liquid Crystal Lens Using Discrete Electrodes

Consider a material of thickness d and refractive index distribution $n(x, y)$ centered on the z axis. The phase retardation is given by

$$\varphi(x, y) = kdn(x, y), \quad (2.12)$$

In order to form a lens, we assume the refractive index can be varied as

$$n(r) = A + Br^2, \quad (2.13)$$

where $r^2 = x^2 + y^2$.

At the center of the cell ($r = 0$), the refractive index reaches the maximum value

$$n(r = 0) = n_e. \quad (2.14)$$

At the edge of the cell, the refractive index is an intermediate value between n_e and n_o :

$$n(r = r_0) = n_i, (n_o \leq n_i < n_e). \quad (2.15)$$

Using the boundary conditions in Equations (2.14) and (2.15), Equation (2.13) becomes

$$n(r) = n_e + \left(\frac{n_i - n_e}{r_0^2} \right) r^2 = n_e - \frac{n_e - n_i}{r_0^2} r^2. \quad (2.16)$$

Thus the transmission function is

$$\begin{aligned} t(r) &= \exp[jkdn(r)] = \exp\left[jkd\left(n_e - \frac{n_e - n_i}{r_0^2}\right)r^2\right] \\ &= \exp(jkdn_e)\exp\left(-jk\frac{n_e - n_i}{r_0^2}r^2\right). \end{aligned} \quad (2.17)$$

As we know, the phase transformation of a thin lens takes the following form (Goodman, 2005):

$$t(x, y) = \exp(jknd_0)\exp\left(-jk\frac{x^2 + y^2}{2f}\right), \quad (2.18)$$

where k is the wave number, n is the refractive index of the lens material, d_0 is the thickness of the center of the lens, and f is the paraxial focal length. The first term is a constant, and the second term represents the phase profile.

Comparing Equations (2.17) and (2.18), we have the focal length of the lens

$$f = \frac{r_0^2}{2d(n_e - n_i)}. \quad (2.19)$$

Because $n_o < n_i < n_e$, the range of the lens power is given by

$$0 < \frac{1}{f} \leq \frac{2d(n_e - n_o)}{r_0^2}. \quad (2.20)$$

Therefore, the power of the refractive lens is determined by the birefringence $n = n_e - n_o$. For the commonly used nematic LC material E7 (from Merck), at 20°C, $n_o = 1.5252$, $n_e = 1.7578$, and $n = 0.2326$ for the wavelength 546.1 nm. According to Equations (2.19) and (2.20), the focal length (power) of the refractive LC lens is limited by n . For large aperture (r_0) lens, the focal length is long, i.e., the power is small. Some high birefringence LCs exist, but their viscosity is too high, resulting in slow response. Therefore, LC lenses based on refractive principle are more suitable for small aperture cases such as microlenses.

The phase modulation of a homogeneously or homeotropically aligned LC cell can be measured by placing the cell in between two crossed polarizers. The normalized light transmittance is given by the general equation:

$$T = \cos^2\chi - \sin 2\beta \sin 2(\beta - \chi) \sin^2(\phi/2), \quad (2.21)$$

where χ is the angle between the polarizer and the analyzer, β is the angle between the polarizer and the initial orientation of the LC director, and $\phi = 2\pi d/n\lambda$ is the phase retardation. For crossed polarizer, $\chi = 90^\circ$. If $\beta = 0^\circ$ or 90° , $T = 0$. If $\beta = 45^\circ$, we have

$$T = \sin^2(\phi/2). \quad (2.22)$$

Therefore, the phase retardation ϕ can be calculated from the transmittance measurement.

Because

$$t(x, y) = \exp\left(-jk\frac{x^2 + y^2}{2f}\right) = \exp\left(-jk\frac{x^2}{2f}\right)\exp\left(-jk\frac{y^2}{2f}\right), \quad (2.23)$$

we can use a 1-D array of electrode strips to form a LC cell to achieve the phase transformation of a cylindrical lens and use two orthogonal array of electrodes to achieve the phase transformation of a spherical lens. But the two cylindrical lenses need to be carefully aligned. Both beam focusing and steering can be implemented by LC cells using discrete electrodes (Brinkley, Kowal, & Chu, 1988; Kowal, Cleverly, & Kornreich, 1984; Nouhi & Kowal, 1984).

Using the discrete isolated electrodes, there is a meshing phase error at the boundary of the electrodes because of the fringe field of the electrodes, especially when the interelectrode gap is relatively big. In order to make smooth phase profile and eliminate the need for complicated electronic drivers, several techniques based on resistive network have been proposed. In the article by Chan and Kowal (1997), conductive meshing and conductive ladder meshing methods were used. The conducting meshing design has a uniformly conducting electrode with multiple driving points, and a linear drop of voltage can be generated across the lens aperture. Conductive ladder meshing is a hybrid of conductive meshing and the conventional architecture. It divides a lens into sections, and each section is formed by two addressable electrodes and interpolating electrodes between these two addressable electrodes. A set of discrete linear voltage drops is yielded across the aperture of the lens. Circular electrodes based on conductive ladder meshing method were fabricated to produce a spherical lens (Sun, Nordin, Kowal, & Wang, 2003). Another nematic LC three-terminal device for optical beam focusing has been proposed by Riza and DeJule (1994). A thin-film-resistor network on the device substrate layer is used to control the voltages on the 98 internal lens electrodes by the use of only one variable external driver. By using a high-resistance thin-film layer of amorphous silicon under the 98-element parallel electrode structure layer, a near-continuous index distribution is generated to form a cylindrical lens. The focal length of this lens is continuously variable from infinity to 12 cm by the use of a variable 1–4-V-peak, 1-kHz square-wave, external terminal control signal. However, the area of the active device that has been demonstrated was only 1 × 1 mm. It is not easy to fabricate large aperture LC lenses using this technique. In addition, the concept of “hybrid electrode” was also proposed to generate gray-scale electric field and simplify both the electrode design and the requirements on the electrical driver (Klaus, Ide, Hayano, Morokawa, & Arimoto, 1999). A bundle of parallel, very narrow, transparent, low-resistive, stripe-shaped electrodes is connected by means of two lateral, narrow, high-resistive electrodes forming together a broad, stripe-shaped “superelectrode.” By applying two different voltages to each terminal of the lateral electrodes, a linear voltage gradient is generated along the lateral electrode as well as across the superelectrode. Two lateral electrodes with respect to a single superelectrode are connected in parallel to guarantee the uniform distribution of the voltage gradient anywhere within the superelectrode. Again only microlenses were fabricated, and it is difficult to apply this approach to LC lenses with larger apertures. It is possible to adopt simplified resistor network for locally linear phase modulation.

2.4. Diffractive Liquid Crystal Lens Using Discrete Electrodes

Recently we have successfully designed, fabricated, and characterized large-aperture, high-performance switchable LC diffractive lenses with discrete ring electrodes and bus lines for power supply.

2.4.1. Background and Analysis—The function of the diffractive lens is based on near-field diffraction by a Fresnel zone pattern. Each point emerging from the structure serves as an emitter of a spherical wave. The optical field at a particular observing point is a summation of the contributions of the emitted spherical waves over the whole structure. Constructive interference of the spherical waves coming from the various points creates a high intensity at the observation point, corresponding to high-diffraction efficiency.

The basic structure of a diffractive lens is illustrated in Figure 4. Figure 4(a) shows a part of a refractive lens. By removing the multiple 2π phase retardation from the refractive lens, we obtain a diffractive lens as shown in Figure 4(b). The phase jump at each zone boundary is 2π for the design wavelength λ_0 , and the blazing profile in each zone makes perfect constructive interference at the focal point. Figures 4(c) and 4(d) show fourth-level and eighth-level approximations of the desired phase profile in Figure 4(b), respectively.

The focal length of the diffractive lens is determined by the period of the zones. As shown in Figure 5, the optical path length differences are multiples of the wavelength. For the j th zone, we have

$$r_j^2 + f^2 = (f + j\lambda)^2. \quad (2.24)$$

For paraxial approximation, $f \gg j\lambda$, the radii of the zones are given by

$$r_j^2 = 2j\lambda f. \quad (2.25)$$

This determines the Fresnel zone pattern, which is periodic in r^2 . The period equals to r_1^2 .

The focal length of the diffractive lens is

$$f = \frac{r_1^2}{2\lambda}. \quad (2.26)$$

Usually, the blaze profile in Figure 1(b) is generated by controlling the thickness of the material and it can be reproduced by single-point diamond turning or laser pattern generation. The discrete-step phase profile shown in Figure 1(c) and 1(d) can be reproduced by binary or grayscale photolithography technology. With the rapid progress in microfabrication, high-diffraction lens can be made with these technologies. The diffraction efficiency of an ideal multilevel diffractive lens is given by (Kress & Mey, 2000)

$$\eta = \text{sinc}^2\left(\frac{1}{L}\right) = \left[\frac{\sin(\pi/L)}{\pi/L}\right]^2, \quad (2.27)$$

where L is the number of phase steps in each zone.

The most important performance parameter for a diffractive lens is diffraction efficiency, which is determined by the phase profile across the lens. Although high-efficiency liquid crystal-based diffractive devices have been demonstrated for beam-steering (e.g., Ferstl & Frisch, 1996; Jepsen & Gerritsen, 1996; Lester, Coulston, & Strudwick, 2006; McManamon et al., 1996; Resler, Hobbs, Sharp, Friedman, & Dorschner, 1996; Slinger et al., 1997; Wang, Wilson, Muller, Maker, & Psaltis, 2000), less effort was given to the development of switchable diffractive lenses. The diffraction efficiencies of the lenses achieved for imaging and other applications were too low, typically around 36% (Dance, 1992; Ferstl and Frisch 1996; Hain et al., 2001; McOwan, Gordon, & Hossack, 1993; Laude, 1998; Ren, Fan, & Wu, 2003; Patel & Rastani, 1991; Williams, Powell, & Purvis, 1989; Wiltshire, 1993). One of the most important applications of the adaptive LC lens is for vision correction. The use of nematic LCs to implement switchable lenses has been proposed earlier but had limited success for ophthalmic applications (Charman, 1993; Smith & Atchison, 1997). The ophthalmic lens has stringent requirements, including high light efficiency, relatively large aperture, fast switching time, low driving voltage, and power-failure-safe configuration. Power-failure-safe configuration means that a loss of electrical power should be safe for critical distance vision task such as driving. None of the previous demonstrations satisfies these requirements simultaneously. The lens-shaped LC cell described above has long response and recovery times resulting from the large thickness of the LC layers (typically >400 μm), and the surface-relief Fresnel lens is optically active in the electrically off-state. The other lens structures to be described later are mainly suitable for micro- or miniaperture lenses. Some of them require high driving voltages and some of them do not provide the range of focal length needed for ophthalmic applications. Here we use photolithographically patterned ring electrodes to form thin flat diffractive lens with large aperture, fast response time, and a power-failure-safe configuration and overcome these limitations. The first thing to consider is the phase profile of the LC cell formed by multiple discrete electrodes in each zone when each ring electrode is applied a different voltage and the corresponding diffraction efficiency.

The phase profile may be affected by various factors, including the number of phase levels in each zone, the gaps between the electrodes, fringing field effect in the transition area of neighboring zones (the elastic properties of the liquid crystal prohibit a sharp phase wrap between zones; Apter, Efron, & Bahat-Treidel, 2004; Brinkley et al., 1988; Wang et al., 2005), and fabrication errors. The effects of the gaps between the ring electrodes and the fringing field on the lens performance have been analyzed (Li, 2008). The amplitude (intensity) in the focal plane can be calculated using Fresnel diffraction integral:

$$U(x, y) = \frac{e^{ikz}}{i\lambda z} e^{i\frac{k}{2z}(x^2 + y^2)} \iint U(x_1, y_1) e^{i\frac{k}{2z}(x_1^2 + y_1^2)} e^{-i\frac{2\pi}{\lambda z}(xx_1 + yy_1)} dx_1 dy_1. \quad (2.28)$$

For axially symmetric system, the above expression becomes

$$U(r) = \frac{e^{ikz}}{i\lambda z} e^{i\frac{k}{2z}r^2} \cdot 2\pi \int_0^R J_0\left(\frac{2\pi r r_1}{\lambda z}\right) U(r_1) e^{i\frac{k}{2z}r_1^2} dr. \quad (2.29)$$

Here, we just show an example. Assume the focal length is 1 m, and the diameter of the lens is 10 mm. Figure 6(a) depicts the normalized intensity distribution around the main focal point for no gap and gaps of various values. When the aperture of the lens is large, the gaps distort the phase profile and hence reduce the diffraction efficiency. The gaps should be kept small. Figure 6(b) illustrates the deviation of the phase profile of one zone from the ideal case caused by the fringing field effect. Type B transition reduces the diffraction efficiency too. The phase modulation for type A and type B can be represented by

$$-\frac{\pi e^{a(r-R)} - e^{-a(r-R)}}{4 \frac{e^{a(r-R)} + e^{-a(r-R)}}{4} + c} \quad (2.30)$$

and

$$\frac{3\pi e^{a(r-R)} - e^{-a(r-R)}}{4 \frac{e^{a(r-R)} + e^{-a(r-R)}}{4} + \frac{3\pi}{4}} \quad (2.31)$$

respectively.

With this model, we estimated that for eighth-level LC diffractive lens, if the gap between the neighboring ring electrodes is 1 μm , the diffraction efficiency can be more than 91% for 10-mm aperture. Detailed analysis and experimental verification of the effect of the interelectrode gaps will be published elsewhere. In order to eliminate the gaps between the electrodes, the odd- and even-numbered electrodes can be interleaved into two layers, which are separated by a SiO_2 insulator layer.

Correspondingly, lenses with three different designs have been demonstrated:

1. All the ring electrodes for modulating the multilevel phase profile are patterned in one layer with a 1- μm gap between the neighboring electrodes. Lenses with eight phase levels, 10-mm diameters, and focal lengths of 1 m and 0.5 m (+1.0 diopter and +2 diopter of add power, respectively) have been demonstrated (Li et al., 2006).
2. In order to avoid the lateral gaps between the electrodes and allow high-diffraction efficiency, the odd- and even-numbered ring electrodes are separated in two layers. A preliminary experiment with interleaved electrode pattern has been performed for a fourth-level, 15-mm aperture, 2-diopter lens with the expected performance (Li et al., 2006).
3. A robust design is given with three-layer electrode pattern and two-layer via structures for flexible interconnection and no-gap pattern (Li, Valley, Äyräs, Honkanen, & Peyghambarian, 2007). The microfabricated transparent concentric ring electrodes are distributed in two layers and different voltages are applied to each electrode through bus lines in another layer. Connection between the electrodes and the bus lines is achieved by vias in the third dimension. This design makes it easier to fabricate lenses with higher-level phase steps and larger aperture and overcome the shorts between the electrodes. This method can be used for design of LC lens of any phase levels. It should be noted that, unlike the

conventional binary optics, in this design the increase of the phase levels (e.g., to 16 levels) in each zone does not increase the fabrication steps.

2.4.2. Switchable Electro-Optic Diffractive Lens with High Efficiency Based on One-Layer Patterned Electrodes—Here we report on new switchable, flat, liquid crystal diffractive lenses that can adaptively change their focusing power. The operation of these spectacle lenses is based on electrical control of the refractive index of a 5- μm -thick layer of nematic liquid crystal using a circular array of photolithographically defined transparent electrodes. It operates with high transmission, low voltage (<2 V_{RMS}), fast response (<1 s), diffraction efficiency exceeding 90%, small aberrations, and a power-failure-safe configuration. These results represent significant advancement in the state-of-the-art in liquid crystal diffractive lenses for vision care and other applications (Li et al., 2006).

The phase jump at each zone boundary is 2π for the design wavelength. The outer radius of each zone is given by

$$r_m = \sqrt{2m\lambda f}, \quad m = 1, 2, \dots, M, \quad (2.32)$$

where m is a counting index that refers to successive Fresnel zone starting in the center, λ is the wavelength, and f is the focal length. To digitize the process, the continuous phase profile in each zone is divided into multiple subzones with a series of discrete phase levels (“staircase” structure, Figure 4(d)). The outer radius of each subzone is given by

$$r_{m,n} = \sqrt{2[(m-1) + n/L]\lambda f}, \quad n = 1, 2, \dots, L, \quad (2.33)$$

where L is the number of phase levels per zone and n is the counting index of the individual phase levels. Diffraction efficiency increases by increasing the number of subzones L , reaching maximum values of 40.5, 81.1, and 95.0% for lenses with 2-, 4-, and 8-phase levels per zone, respectively.

Diffractive lenses with eight subzones, 10-mm diameters and focal lengths of 1 m and 0.5 m (+1.0 diopter and +2 diopter of add power, respectively) were demonstrated at the peak of the human photopic response, 555 nm. The schematic drawing of the electrode pattern is shown in Figure 7, and the fabrication procedure is shown in Figure 8. Using photolithographic techniques, concentric and rotationally symmetric transparent indium tin oxide (ITO) electrodes (50 nm in thickness), whose radii were determined by Equation (2.33), were patterned on a float-glass substrate. A 1- μm gap was required between adjacent electrodes to maintain electrical isolation and ensure a smooth transition of the phase profile introduced by the liquid crystal. Over the patterned ITO, a 200-nm-thick electrically insulating layer of SiO_2 is sputtered into which small via openings ($3 \times 3 \mu\text{m}$) were etched, allowing electrical contact to be made to the underlying electrodes. An electrically conductive layer of Al is subsequently sputtered over the insulating layer to fill the vias and contact the electrodes and patterned to form eight independent electrical bus bars (6- μm wide within the lens). Each bus bar connects the discrete phase level electrodes of equal

counting index n in all Fresnel zones (as shown in Figure 7) such that only eight external electrical connections (plus one ground connection) are required per lens.

The patterned substrate, as well as an additional substrate with a continuous ITO electrode that acts as the electrical ground, were spin coated with poly(vinyl alcohol) to act as liquid crystal alignment layer. The alignment layers were rubbed with a velvet cloth to achieve homogeneous alignment, and the two substrates were assembled. The commercial nematic liquid crystal E7 (Merck) was used as the electro-optic medium and was filled by capillary action into the empty cell at a temperature more than the clearing point (60°C) and then cooled at $1^{\circ}\text{C}/\text{min}$ to room temperature. The cell was then sealed with epoxy and connected to the drive electronics. The drive electronics consist of custom fabricated integrated circuits that contain eight independently controlled output channels. Each channel generates a modified square waveform with variable peak-to-peak amplitude between 0 and 5 V.

The lens showed excellent performance (because of space limitations, we only describe the results for 1-diopter lens). In the optically inactive state (voltage off) in which the lens has no focusing power, optical transmission is 85% over the visible spectrum, a value that can be increased by the use of ophthalmic quality substrates and antireflection coatings. A computer-interfaced polarized optical microscope with a laser source at 543.5 nm (Figure 9) was constructed on the optical bench and used to inspect the lenses on a microscopic scale and to verify that all electrodes were operating properly. The lens was placed between crossed polarizers where the transmission axes are oriented at angles of 45° and -45° with respect to the liquid crystal alignment layer rub direction. For each position on the lens, the intensity seen by the CCD camera is a function of the voltage-dependent phase retardation $\phi(V)$ between the ordinary and extraordinary wave components at the exit surface of the lens. Therefore, the voltage-dependent phase retardation of each electrode can be inspected by observing the intensity variations over its area. Monochromatic polarized microscopy images of the lens under operation indicate that all eight electrode sets operated properly and provided discrete phase changes (Figure 10).

Eight optimized drive voltages with amplitudes between 0 and $2V_{\text{rms}}$ produced a maximum first-order diffraction efficiency of 91%, near the 95% predicted by scalar diffraction theory. The measured diffraction efficiency as a function of lens area reaches 94% near the center of the lens, decreasing monotonically as the area is increased (Figure 11). The decrease is because of the fact that phase distortion caused by the fringing field at the zone boundaries has more significant effect at the outer zones as the width of each electrode becomes smaller. At the edges of the electrodes, the electric field lines are not perpendicular to the liquid crystal lens substrate and the fringing fields cause the phase transitions at the zone boundaries to be not as sharp as in the ideal case; thus inducing phase distortions and reducing the diffraction efficiencies. The diffraction efficiency as a function of incidence angle is related to practical application of the adaptive lens for vision correction. The measurement is depicted in Figure 12. It drops about 3% when the incidence angle is 20° . The focused spot size is about 135 μm , which is also close to the diffraction-limit value of 133 μm . The lens shows subsecond switching time.

The performance of the diffractive lenses was also evaluated using a computer-interfaced, phase-shifting Mach-Zehnder interferometer with a linearly polarized 543.5-nm laser source (Figure 13). The lens under test was placed in the object arm of the interferometer and then imaged onto a CCD camera such that the captured interference patterns are formed by the converging wavefront generated at the exit face of the lens and the reference plane wave. A small aperture was placed between the imaging lens and the camera at the point of focus in order to isolate and test only the wavefront generated by the first-diffracted order. Multiple $\pi/2$ phase shifts are generated in the reference arm using a PZT-actuated mirror, and a phase-unwrapping algorithm is then used to generate a phase map of the diffracted wavefront. The data is processed using IntelliWave (Engineering Synthesis Design, Inc). From this unwrapped phase map of the wavefront immediately behind the diffractive lens, the focal length (f) of the diffractive lens is calculated using

$$f = \frac{\rho^2}{2\text{OPD}}, \quad (2.34)$$

where OPD is the peak-to-valley optical path difference from center to edge and ρ is the radius of the test area (Born & Wolf, 1999). As the lenses were designed for operation at 555 nm but tested at 543.5 nm, correction of the extracted focal length value was made by

$$f(\lambda) = f_0 \frac{\lambda_0}{\lambda}, \quad (2.35)$$

where f_0 and λ_0 are the design focal length and wavelength, respectively, and λ is the measurement wavelength. Measurement of the peak-to-valley and RMS errors in the wavefront were made subsequent to removing the best fit sphere and any tilt from the phase map.

The imaging performance of the lens can be evaluated in terms of the modulation transfer function, which represents the ratio of the image modulation to the object modulation at all frequencies. The wavefront of the first-order diffraction can be expressed by a sum of Zernike polynomials (Born & Wolf, 1999), and the modulation transfer function can, thus, be calculated by normalized autocorrelation of the generalized pupil function.

Interferometric measurements at 543.5 nm show excellent imaging capability of the lens. Strong modulation of the optical power is observed in interferogram of the lens in the optically active state (Figure 14). The unwrapped phase map of the lens is shown in Figure 15(a) with a peak-to-valley optical path length of 23.05λ . The focusing power was estimated to be 1.002 diopter in excellent agreement with the design value. Very good spherical profiles were obtained in both x and y cross sections, indicating small aberrations. Higher-order aberrations were estimated by analyzing the difference between the measured wavefront and a best-fit spherical wave and tilt (Figure 15(b)). The peak-to-valley range of the difference is 0.241λ and the RMS value is 0.039λ , which is comparable with a high-quality reading glass. The modulation transfer function indicated near diffraction-limited performance (Figure 15(c)). All properties of the lens, as shown in Figures 11 and 14, make the switchable lens suitable for ophthalmic applications.

For vision correction of presbyopic eyes, polarization insensitive switchable lenses are needed. As homogeneously aligned nematic liquid crystals are polarization sensitive, two lenses with orthogonal alignment directions were used in series to create a single polarization insensitive lens. Two such lenses were aligned and cemented together. Figure 16 depicts the alignment of the two lenses. The two lenses are mounted on translation stages. The incident light is linearly polarized at 45°. A CCD detector is put at the focal plane. When the two lenses are displaced, the two focal spots are separated (see upper right of Figure 16). When the two lenses are well aligned, the two focal spots are overlapped (see lower right of Figure 16) and the lenses are cemented together.

For real application, the lenses will be centered on the line of sight when the user is looking at a near object, i.e., the locations of the centers of the LC lenses should be made to coincide with where the optical axes of the eyes pass through the spectacles when viewing a near object. In this way, any off-axis component is minimized, and the optical performance is maximized. Optical simulation showed that the two lenses and the human eye model can generate good image spots. To demonstrate vision correction, a model eye was constructed using a fixed +60-diopter achromatic doublet glass lens and a CCD with a filter to match the human photopic response. The chromatic aberration of this system is ~0.5 diopter. To simulate a typical near vision task such as reading, a double-element lens was placed in front of the model eye and used to image a test object illuminated with unpolarized white light placed 30 cm in front of the lens. As can be seen in Figure 17(a), the model eye has insufficient power to form a sharp image, but by switching on the diffractive lens the image is brought into focus (Figure 17(b)). The double-element lens has excellent optical transmission. When the electro-optic lenses are both in the inactive state, there is no noticeable degradation in the quality of the distant vision. For chromatic aberration, an achromatic diffractive lens can be designed by introducing $p2\pi$ ($p > 1$, integer) phase jump at the zone boundaries for the design wavelength (Faklis & Morris, 1995). In practice, the ocular lens itself has a chromatic aberration, which is less than the diffractive lens. Assuming the brain is adapted to a certain degree of chromatic aberration, balancing the dispersion of the diffractive lens and the eye is less desirable. More clinical study will be performed on this.

In this section, we have demonstrated switchable liquid crystal diffractive lenses with high-diffraction efficiency, high optical quality, rapid response time, and diffraction limited performance. These flat lenses are highly promising to replace conventional area division refractive, multifocal spectacle lenses used by presbyopes. They have the potential of revolutionizing the field of presbyopia correction when it is combined with automatic adjustable focusing power. Negative focusing powers can also be achieved with the same lenses by changing the sign of the slope of the applied voltages. The use of these lenses is not limited to ophthalmology but can be extended to numerous other applications where switchable lens elements with relatively large diameters are desirable.

2.4.3. Switchable Electro-Optic Diffractive Lens with High Efficiency Based on Two-Layer Patterned Electrodes for Ophthalmic Applications—In order to develop various approaches that allow large aperture, fast response time, low-operating voltages, high-diffraction efficiency, and power-failure-safe configuration, we presented a

design for high-efficiency switchable diffractive lens by separating odd- and even-numbered ring electrodes into two layers and thus eliminating the gaps between the neighboring electrodes (Li et al., 2006). Compared to the design with the one-layer electrode pattern, another advantage of this concept is that it is easier to overcome shorts between neighboring conductive electrodes and fabricate lenses with larger aperture and smaller feature size. The thickness of the LC is only 5 μm . Diffraction efficiency of 75% has been achieved in fourth-level phase modulation lenses with 15 mm diameter and a focusing power of two diopters. The response time and the decay time were measured to be 180 and 120 ms, respectively. The operating voltages are less than 2 V.

Figure 4(c) shows a fourth-level approximation (solid line) of the desired phase profile (dashed line). In each zone, multiple steps are used to approximate the desired phase profile. The structure is periodic in r^2 (r is the radius), and the period is equal to r_1^2 , where r_1 is the radius of the first zone. Each zone (subzone) has the same area as r_1^2 (r_1^2/N , where N is the discrete phase levels). Here we consider the nematic LC lens (Figure 18(a)), where the phase profile is obtained by the electrically controlled birefringence effect. A nematic LC layer (E7 from Merck with birefringence greater than 0.2) is sandwiched between a patterned electrode substrate and a ground electrode substrate. The patterned electrode is fabricated by photolithographic processing of an indium-tin-oxide (ITO) film deposited on a glass substrate, and the ground electrode substrate contains a uniform conductive ITO layer. The patterned electrodes consist of a circular array of rings. Both of the two electrode surfaces are coated with polyvinyl alcohol (PVA) as an alignment layer and are treated by rubbing to give a homogeneous molecular orientation. The refractive index experienced by the extraordinary beam is changed because of the reorientation of the LC molecule when a voltage is applied to the medium. The phase profile across the lens is tailored by applying proper voltages to the patterned electrodes and as such, determines the diffraction efficiency. The phase profile may be affected by various factors, including the quantization error (number of phase levels in each zone), the gaps between the electrodes, fringing field effects in the transition area of neighboring zones, and fabrication errors. The quantization error can be reduced by increasing the number of phase levels in each zone. For instance, an ideal diffractive lens with 2- and 4-level digitization corresponds to efficiency of 40.5 and 81.1%, respectively. Simulations show that the gaps between the electrodes and different types of phase distortion at the electrode boundaries greatly affect diffraction efficiency and other performance parameters. To alleviate this effect, the odd- and even-numbered rings can be interleaved into two layers that are separated by an insulating layer such as SiO_2 . In this demonstration, all the subzones having the same counting index n ($n = 1, 2, \dots, N$) are connected together by a bus line, i.e., applied the same voltage, and thus have the same phase value. Figure 18(b) shows the cross section of the two-layer electrode pattern, where odd- and even-numbered rings are distributed in two layers, and there are no gaps between two neighboring electrodes. The schematic diagrams for the pattern of the odd-numbered electrodes and for the pattern of the even-numbered electrodes are shown in Figure 18(c). The fabrication procedure for the interleaved electrode pattern is illustrated in Figure 19. With this design, it is easier to avoid shorts between neighboring ITO electrodes and fabricate lenses with larger aperture and smaller subzones.

Here, we demonstrate a fourth-level, 15-mm-aperture lens with a 2-diopter focusing power at 555 nm, the peak of the human photopic vision response. The width of the last subzone at the edge is 9.2 μm . After the lens is fabricated, various optical characterizations are performed. In the off state, transmission of the lens over the visible spectrum is more than 85% if there is no antireflection coating on the surfaces. A polarized microscope is used to check the electro-optic function of each electrode. The lens is placed between two crossed polarizers, which are aligned with their transmission axes at 45° and -45° , respectively, to the horizontal axis. For each position, the intensity at the detector changes with the change of the phase difference (ϕ) between the ordinary and extraordinary components at the exit surface of the lens. The operation of each electrode can be inspected by observing the intensity variations over the area of said electrode. Figure 20 shows the intensity variation on electrode 1 when electrodes 2, 3, 4 were set to certain voltages, respectively, and the voltage applied to electrode 1 was adjusted. The electrode boundaries can be clearly observed in the images.

To determine the diffraction efficiency as a function of lens area, an iris is placed at the center of the lens and the diffraction efficiency is measured for various beam sizes. Variation of the diffraction efficiency is depicted in Figure 21(a). The efficiency for the 15-mm-diameter area is more than 75%. As we expect, the lens without gaps has only a little decrease in efficiency when the activated area increases. The decrease is because the phase distortion caused by the fringing field has more significant effect on the outer zones. The efficiency of the center area is close to the theoretical value as the fringing field effect is negligible in this area. Dependence of the diffraction efficiency on the incidence angle is related to the field-of-view effect for normal use of the spectacle lenses. From the experiment, the diffraction efficiency decreases monotonically as the increase of the incidence angle. It drops about 4% when the lens is tilted 20° about the lateral axis.

A Mach-Zehnder interferometer operating at 543.5 nm was used to measure wave-front quality immediately behind the lens and to determine the focal length. The technique is based on interference between the spherical wave after the lens and a reference plane wave. Figure 21(b) shows an example of the measured interferograms. Five interferograms were taken with a phase shift between each interferogram and the wrapped phase map can be produced. The unwrapped phase map represents the actual optical path difference profile generated by the diffractive lens. It is generated from the wrapped phase by removing the 2π discontinuities. The unwrapped phase map of the lens is shown in Figure 21(c). A good spherical wave was obtained with very few higher-order aberrations as indicated by an RMS wave front error of 0.0889λ . The focal length was found to be 50.855 cm and by using Equation (2.35), the focal length at 555 nm was calculated as 49.80 cm, which corresponds to a focusing power of 2.008 diopter and indicates that accurate focusing power can be achieved. The focused spot size was also measured and found to be 47.9 μm , close to the diffraction-limited spot size of 45.1 μm . The response time and the decay time were measured to be 180 and 120 ms, respectively. All these parameters indicate high performance of the lens. In addition, we also verified that, by changing the slope of the applied voltages to each zone, a negative 2-diopter focusing power can be obtained with the same lens, and the diffraction efficiency is the same as the positive 2-diopter case.

As nematic liquid crystal is polarization sensitive, two LC lenses with orthogonal alignment directions are required to form a complete lens that works for randomly polarized light. The double-element complete lens has been demonstrated to provide near vision correction for an accommodation free model eye consisting of a 60-D refractive lens, an iris, and a CCD array. A white light source illuminates the object placed at a typical reading distance of approximately 30 cm. When the diffractive lens is not activated, the image is blurred (Figure 22(a)) but when the diffractive lens is turned on, the object is imaged clearly (Figure 22(b)). The ON- and OFF-state of the lens allow near- and distance-vision, respectively.

In this section, we have demonstrated a high-performance switchable electro-optic adaptive diffractive lens for vision correction of presbyopia. By interleaving the odd-numbered and even-numbered electrodes into two layers, there is no gap between the neighboring electrodes. This helps to maintain the desired diffraction efficiency, and it makes it easier to fabricate lenses with large aperture and small feature size without shorts between the ring electrodes. Diffraction efficiency of more than 75% has been achieved for fourth-level lenses with 15-mm aperture. This design methodology can be extended to phase steps larger than four, where the electrodes can be addressed from an additional layer through vias. However, more fabrication steps are required. The focusing power of the lens can be adjusted to be either positive or negative, depending on the voltages applied to the patterned electrodes. Other advantages of this lens include compact, lighter weight, low cost, and easier operation with low voltages and low-power dissipation. For people those who also need correction for distance vision, an additional refractive lens can be integrated with the switchable diffractive lens. Using nematic LC, two LC lenses set in orthogonal direction are required to make it polarization insensitive. In order to avoid light loss as a result of back reflections at the substrate interfaces, antireflection coating is necessary.

2.4.4. Robust Structure with Three-Layer Electrode Pattern and Two-Layer via Structures for Flexible Interconnection and No-Gap Pattern—In Section 2.4.3, we demonstrated a switchable diffractive LC lens with high performance. In that design, the ring electrodes for modulating the eighth-level (number of phase digitization) phase profile are patterned in one layer with a 1- μm gap between the neighboring electrodes. In order to avoid the lateral gaps between the electrodes, we did a preliminary experiment with interleaved electrode pattern. However, with that design, the number of phase levels is limited only to four. Here we show a novel and general design for flat thin diffractive lens with high performance and powerful functions for vision care. It has three-layer microfabricated electrode pattern and two-layer via structures for flexible interconnection and no-gap pattern (Li, Valley, Äyräs, Honkanen, & Peyghambarian, 2007). It allows any even-numbered phase levels greater than four and provides the capability of correction for near-, intermediate-, and distancevision. Such a lens has potential of revolutionizing the field of presbyopia correction.

The diffractive lens is designed at the peak of the human photopic response, 555 nm. The radii of each zone and subzone are given by Equations (2.32) and (2.33). A nematic LC layer is sandwiched between a ground electrode substrate and a patterned electrode substrate. The ground electrode substrate contains a uniform conductive indium-tin-oxide (ITO) layer and the patterned electrodes are fabricated by photolithographic processing. For

higher diffraction efficiency and ease of control, the patterned electrodes have a ring shape defined by Equation (2.33). If all the ring electrodes for tailoring the refractive index are patterned in one layer, there must be gaps between neighboring electrodes. When the aperture of the lens is large, the gaps will distort the desired phase profile and hence reduce the diffraction efficiency. In order to avoid this effect, the odd- and even-numbered electrodes are interleaved into two layers. The discrete electrodes for equal phase level in different zones are connected by a bus line through vias. The module was fabricated from the bottom to the top. All the bus lines are distributed in one layer in the bottom, and the number of the bus lines is equal to the number of phase levels in each zone. Therefore, there are three layers of electrodes and two layers of vias in total, as shown in Figure 23. The layer for the bus lines, the layer for the odd-numbered electrodes, and the layer for the even-numbered electrodes are isolated by two insulator layers of SiO_2 , where vias are made for conduction between the bus lines and the ring electrodes. The fabrication procedure for the module is illustrated in sequences in Figure 24. The etching time for SiO_2 is optimized by checking the conductivity between ITO test structures, while the etching time for ITO is optimized by eliminating the electric shorts between different electrodes, i.e., electrodes for different phase levels. The new design makes it easier to fabricate lenses with higher-level phase steps and larger aperture and overcome the shorts between the electrodes. This method can be used for design of LC lens of any phase levels. It should be noted that, unlike the conventional binary optics, in this design, the increase of the phase levels (e.g., to 16 levels) in each zone does not increase the fabrication steps. The lens assembly procedure has been described earlier. The initial orientation of the molecules is parallel to the polarization of the incident beam, which is an extraordinary beam, and its effective refractive index can be changed in the range from n_e to n_o due to the reorientation of the LC molecule when a voltage is applied. The material has a positive dielectric anisotropy (>0.2), which provides enough phase modulation for the visible wavelength with the 5- μm -thick cell.

The polarized optical microscope (Figure 9) was used to inspect the lenses on a microscopic scale. Images of the eighth-level 1-diopter lens under operation indicate that all eight electrode sets operated properly and provided discrete phase changes (Figure 25(a)). Eight drive voltages with amplitudes between 0 and 2 V_{rms} were optimized and the maximum first-order diffraction efficiency (ratio of first-order diffracted power to the total transmitted power) of 92.5% was obtained for the whole lens area. The diffraction efficiency was measured as a function of the beam diameter. It reaches 94% near the center of the lens and decreases monotonically as the beam diameter is increased (Figure 25(b)). The diffraction efficiency at different location of the lens is shown in Figure 25(c). Although there is a small decrease due to the phase distortion caused by the fringing field at the zone boundaries, it is flatter than that of the design with gaps between the electrodes. The diffraction efficiency as a function of incidence angle is depicted in Figure 25(d). It drops about 4% when the incidence angle is 20°. As shown in Figure 25(e), switching of the lens is relatively fast. The rise time between 10 and 90% of the diffraction efficiencies was 150 ms and the full decay time was 134 ms. The wavefront immediately behind the lens can be measured using a phase-shift interferometer. Figure 25(f) shows one interferogram formed by the test wave and the reference wave. The RMS error of the spherical wavefront was measured to be 0.0688 waves. The parallelism between the two substrates of the lens may cause variation of

the RMS error. In addition, for the same lens, negative focusing power (-1 diopter) can also be achieved with the same diffraction efficiency by changing the sign of the slope of the applied voltages.

To demonstrate the vision correction capability, the double-element LC lens was put in front of the model eye and an object was placed ~ 35 cm in front of the lens with unpolarized white light illumination. When the complete LC lens is off, the model eye has insufficient power to form a sharp image (Figure 26(a)). But by switching on the diffractive lens, the image is brought into focus with excellent contrast (Figure 26(b)).

Based on the current design, the focal length of the lens can be switched between a few digital values by reducing the zone period digitally, and each corresponds to different diffraction efficiency. Assume an 8-level lens with the design focal length $f=F$ (Figure 26(c)). If each zone is divided into two, and voltage V_1 is applied to all the first and the fifth subzones, V_2 to all the second and the sixth subzones, V_3 to all the third and the seventh subzones, and V_4 to all the fourth and the eighth subzones, then the lens has a focal length of $F/2$ with an efficiency corresponding to 4-level phase digitization (lower part of Figure 26(c)). Actually every four subzones form a new zone for the lens with the focal length $F/2$. Furthermore, if each zone is divided into four, the lens has a focal length of $F/4$ with an efficiency corresponding to a 2-level device. In this case, every two subzones form a new zone. With the 8-level 1-diopter lens described earlier, diffraction efficiency of 78% was obtained when it is optimized for the 4-level 2-diopter case. The diffraction efficiency as a function of the lens aperture is shown in Figure 25(b), and hybrid imaging with the model eye is shown in Figure 26(d). For the same condition, the 2-diopter LC lens would allow the model eye to see objects at a closer distance than the 1-diopter lens. The main effect on the image is the brightness. Therefore, the same electro-optic LC lens can be switched for near-, intermediate-, and distant-vision with each using the whole lens aperture.

Similarly, the focal length F of a 12-level diffractive lens can be adjusted to $F/2$, $F/3$, $F/4$, and $F/6$, with diffraction efficiency corresponding to a 6-, 3-, 4-, and 2-level device, respectively. For 6-level case, all the subzones of (1 and 7), (2 and 8), (3 and 9), (4 and 10), (5 and 11), (6 and 12) from each zone are applied the same voltages, respectively. For the 4-level case, all the subzones (1, 5, and 9), (2, 6, and 10), (3, 7, and 11), (4, 8, and 12) from each zone are applied the same voltages, respectively. For the 3-level case, all the subzones of (1, 4, 7, and 10), (2, 5, 8, and 11), (3, 6, 9, and 12) from each zone are applied the same voltages, respectively. For the 2-level case, all the subzones (1, 3, 5, 7, 9, and 11), (2, 4, 6, 8, 10, and 12) from each zone are applied the same voltages, respectively.

In this section, we have demonstrated flat, thin, switchable LC diffractive lens with three-layer-patterned electrodes and two-layer via structures, which is a general design for multilevel phase modulation. The lens has high-optical quality, good response time, and this design allows larger aperture. The focusing powers of the whole aperture can be switched between different values. This kind of lens may afford an alternative to replace area division multifocal spectacle lenses. Antireflection coatings can be used to avoid light loss at the substrates. Usually correction of presbyopia needs an add power less than 3 diopters, and a 15-mm aperture for the center area is enough. In this case for an eighth-level lens, the

smallest subzone is $\sim 3.1 \mu\text{m}$. With the state-of-the-art facilities, it is feasible to make such lenses. For correcting a residual refractive error for myopia or hyperopia, a curved substrate can be used or the lens can be used together with a contact lens for eyes that need minor correction for distance vision. The other concern is the temperature dependence of the lens performance. The refractive indices of the LC change as a result of the temperature variation (n_e has a larger change than n_o). A temperature sensor and a variable voltage circuit are needed for compensation. The birefringence disappears above the clearing point in the isotropic phase.

2.4.5. Improved Design with Individually Addressed Electrode Pattern—

Although connecting the corresponding subzones together is easy to operate at the design focal length, it results in some disadvantages for ophthalmic application. First, if the design focal length F is for near-vision correction, it cannot provide intermediate vision because the switchable focal lengths are F and a few values smaller than F . Second, the diffraction efficiency is different for each switchable focal length. When the lens is adjusted to work with second- or third-level phase modulation within each zone, the efficiency is relatively low for vision.

In order to overcome the above-mentioned disadvantages, each electrode (subzone) must be individually addressed, as shown in Figure 27 (Li, Ayras, & Peyghambarian, 2006). Assume the geometry of the electrode pattern is designed for focal length F with L-level phase modulation. The flexibility of this architecture is to increase the zone period. For instance, based on Equations (2.32) and (2.33), if the zone period r_1^2 is increased to $2r_1^2$ by grouping every two neighboring subzones into one, i.e., applying the same voltage to the two neighboring electrodes, then the focal length is changed to $2F$ without change of diffraction efficiency (Figure 28). Similarly, with the fixed electrode pattern, the focal length can be varied to $3F, 4F, \dots$, by increasing the zone period to $3r_1^2, 4r_1^2, \dots$, respectively. This provides the lens with the adaptive capability to near, intermediate (e.g., computer screen), and distance vision for presbyopia eyes. Because the F value cannot be too small (when F is small, the feature size of the electrodes becomes very small for a 15-mm-aperture lens, and it is impossible to make them with low cost), one design can only be used by subjects who need the corresponding correction.

It will be more attractive to design the adaptive lens that can be used by all the subjects. This requires the lens have the capability to quasi-continuously change the focal length. Here we propose a new general design that allows continuous change of the focal length. The patterned electrodes are a circular array of rings of particular size. A proper resolution of the ring can be determined by the focal length range to be adjusted. Each ring can be individually addressed. For each desired focal length, the size of each subzone of all the zones can be calculated using Equation (2.33). A certain number of rings can be chosen to form each subzone and appropriate voltage can be applied. If the resolution of the rings is good enough, the lens can always have high efficiency with no significant change. With this design, lenses of various powers can be obtained using the same electrode pattern. To avoid the gaps between the electrodes, even- and odd-numbered electrodes can be interleaved into two layers. Because the zones that are close to the center have larger size, sparser electrodes

can be used in that area (the size of the electrodes close to the center can be bigger than those in the other area). With current fabrication technology, the array of ring electrodes with a small feature size (less than 5 μm) can be made. The proposed structure is easier to control than the spatial light modulator. Simplified resistor network may be used to generate locally linear drops of voltage so that a small number of electrodes can produce the desired phase modulation.

2.5. Liquid Crystal Lens Based on Hole-Patterned Electrode

2.5.1. Basic Structure—Axially symmetric, continuous inhomogeneous electric field can be generated by a hole-patterned electrode and a uniform counter-electrode, and homogeneously aligned LC cell can be used to function as an adaptive lens (Nose & Sato, 1989). Figure 29(a) shows the cross section of the nonuniform electric field inside the cell. The hole-patterned electrode (top view shown in Figure 29(b)) was made photolithographically from thin aluminum film deposited on the glass substrate. Both electrode surfaces were treated with homogeneous alignment layers for LCs with positive dielectric anisotropy. The optical property of the LC cell would depend on the orientation of the LC directors resulting from the nonuniform electric field. In Figure 29(a), the electric field is represented by arrows. The length of each arrow corresponds to the field strength and the direction coincides with that of the local electric field. It should be noted that the strength of the electric field reaches the maximum at the edge of the hole pattern and becomes smaller at the center of the hole. The angle between the direction of the field and the normal to the substrates also approaches the maximum at the edge of the hole.

When there is no electric field applied, the directors of the LC are uniformly parallel to the substrates and the refractive index is equal to n_e . When a voltage more than the threshold is applied, the directors near the edge of the hole start to reorient and the directors close to the center remain parallel to the substrate. Therefore, the refractive index near the edge is smaller than n_e . This leads to a gradient refractive index distribution across the hole with the maximum value at the center and the LC cell operates as a converging lens. When the applied voltage increases, the gradient of the refractive index decreases and the focal length becomes longer according to Equation (2.19). If the applied voltage further increases to a high value, the refractive index profile can be opposite, and the LC cell functions as a diverging lens. By changing the shape of the hole from a circle to a rectangle or an ellipse, cylindrical, and anamorphic lenses can be achieved, respectively (He, Nose, & Sato, 1995; Honma, Nose, & Sato, 1999; Ren, Fan, Gauza, & Wu, 2004b). By dividing the electrode with circular hole into several subelectrodes and applying appropriate potentials to each subelectrode, anamorphic lens can also be obtained (Ye & Sato, 2005). Besides homogeneous LC cell, adaptive microlens formed by homeotropic aligned LC with positive dielectric anisotropy has also been studied (Scharf, Fontannaz, Bouvier, & Grupp, 1999). Comparative study of the lens with different alignment was conducted by Gvozdarev and Nevskaia (1999, 2001a, 2001b). It turns out that under low voltages the LC microlenses with a homeotropical alignment possess defocusing properties and the microlenses with planar and hybrid alignments possess focusing properties. With the increase of the ratio of lens diameter to the LC thickness, the applied voltage increases. At higher voltages, planar- and hybrid-aligned microlenses become defocusing.

The above LC cell is termed as the asymmetric electrode structure. With homogeneous alignment of the LC, a disclination line is usually observed in the direction perpendicular to the director of the LC. Such a disclination line can be eliminated by hybrid alignment of the LC (Nose, Masuda, & Sato, 1991a), where the surface of the hole-patterned electrode is treated with homeotropic alignment while the surface of the continuous electrode is still treated with homogeneous alignment. But the lens properties are not improved much because the center of the lens shifts. To overcome these issues, homogeneous LC lens with a symmetric electrode structure has been proposed where cocentered hole-patterned electrodes are used for both substrates (Nose, Masuda, & Sato, 1991b, 1992). Yanase, Ouchi, and Sato (2002) also investigated the effect of the ratio of the diameter of the hole in the bottom electrode to that of the hole in the top electrode on the lens property under various applied voltages. Interestingly, when the ratio is about 1:2 and the applied voltage is above certain value, the phase profiles at the center and the outer regions are approximated by near-parabolic curves of different coefficients, which mean bifocal lengths. With these symmetric and nonsymmetric hole-patterned LC structure, the ratio D/t of the lens diameter (D) to the thickness of the LC layer (t) should be less than 10 for good optical performance. The optimum ratio of D/t is about 2:3. Diffraction-limited LC microlenses with lens diameters 120 and 110 μm and D/t ratio about 2.4 have been demonstrated (Scharf, Kipfer, Bouvier, & Grupp, 2000). Because the thickness is typically limited to a few tens of micrometers for fast response time, the lens diameter can only be a few hundred micrometers. This limitation has been broken by inserting a dielectric slab between the hole-patterned electrode and the LC layer (Ye & Sato, 2002).

2.5.2. Liquid Crystal Lens with Circular Hole-Patterned Electrode Detached from the LC Layer—As shown in Figure 30 (Ye & Sato, 2002), LC is sandwiched between two glass substrates and treated with homogeneous alignment. The top surface of the lower glass is coated with conductive thin film, and the top surface of the upper glass substrate is coated with a circular hole-patterned electrode. The difference between this structure and the structure described above is that there is an insulating glass layer between the LC layer and the hole-patterned electrode, and because there is distance between the hole-patterned electrode and the LC layer, a nonuniform electrical field produced by the free electric charges in the electrodes and the induced electric charges at the glass surfaces is distributed over a larger area in the LC, allowing a larger aperture of the lens. Experiment with a 7-mm-lens aperture, 130- μm -thick LC layer, and 1.3-mm-thick glass substrate has been demonstrated. The phase profile can be adjusted by the diameter of the lens and the thickness of the substrate. However, the required voltage is 70 V_{rms} . It is also possible to use the symmetric two hole-patterned electrodes structure, but the driving voltage will be doubled.

However, as the directions of the LC directors are spatially variant, the boundary of the different domains of rotation appears as a disclination line that greatly degrades the optical quality of the lens. A new driving method has been proposed, which allows all the directors in the cell to rotate in the same direction (Ye, Wang, & Sato, 2003). In this approach, an electric current flows in one of the electrodes for a short time interval at the beginning of voltage application. The electric field associated with the current tilts the electric field lines

in the LC to one side, making the angles between the directors and the electric lines acute in most locations in the cell. The directors then tend to align with the electric field in the same direction. Defects therefore do not appear. With this driving technology, the application of a temporal high voltage to accelerate the response of an LC lens to the applied voltage is also realized (Ye & Sato, 2005).

In order to increase the tunable range of the lens power, two LC layers can be incorporated into this structure by putting the hole-patterned electrode in the center of the device, as shown in Figure 31 (Ye, Wang, & Sato, 2004a). The power enhancement is because of the electrical interaction between the components at two sides of the Al electrodes through the open hole. The focusing power of the lens becomes much larger than two times that of the LC lens with one LC layer. If the buffering directions of the alignment layers for the two LC layers are perpendicular to each other, the lens becomes polarization independent, i.e., the lens can focus incident light of arbitrary polarization state (Ye & Sato, 2003). To further enhance the tunable range, a new design that drives the LC cell using two voltages has been proposed (Ye, Wang, & Sato, 2004b). With reference to Figure 30, another ITO electrode is placed on the hole-patterned Al electrode with a 70- μm -thick glass slide between them (Figure 32). The geometrical sizes of the components in the cell are the same as those in Figure 30, except that the diameter of the circular hole becomes 4.5 mm. Two voltages V_1 and V_2 drive the cell. V_1 is maintained to be 70 V_{rms} , and V_2 changes from 0 to 70 V_{rms} to tune the lens power. The spatial variation of E in the hole area decreases with increasing V_2 , and hence so does the power. The range of the variable power is very wide, covering 0.8–10.7 D . When $V_1 < V_2$, the electric field in the LC layer increases from the edge to the center of the hole area, and so does the refractive index, and then the cell becomes a negative lens. So by adjusting V_1 and V_2 , the power of the LC cell can be variable from negative to positive values (Wang, Ye, & Sato, 2005a, 2006a). An example is presented here. For the cell with 75- μm -thick LC layer, 3-mm-lens aperture, 1.3-mm-thick glass between the hole-patterned electrode and the LC layer, and 50- μm -thick thin glass slide between the hole-patterned electrode and the upper ITO electrode, when V_1 is maintained at 35 V_{rms} and V_2 is tuned in the range from 0 to 40 V_{rms} , the LC cell works as a positive lens. However, when V_2 is maintained at 60 V_{rms} and V_1 is tuned in the range from 0 to 50 V_{rms} , the cell works as a negative lens. The data is shown in Figure 33. Aberrations of the two-voltage-driven LC lens were measured using a Fizeau interferometer and optimum conditions for operation as positive or negative lens were discussed (Takahashi, Ye, & Sato, 2007). If the LC layer in Figure 24 is replaced by two thin LC layers as shown in Figure 34 (Wang, Ye, & Sato, 2005b, 2006b), the operation speed of the lens will be improved and the focus range will be wider. Experiments show that the lens power of the two-LC-layer lens is approximately twofold larger than that of the single-LC-layer lens. On this basis, if two more LC layers are added to the other side of the hole-patterned electrode but with orthogonal homogeneous alignment, a polarization-independent LC lens with a large tenability can be produced (Ye, Wang, & Sato, 2006).

There are two additional LC lens structures that are driven by two voltages and they allow increased focusing power for mini aperture lenses. One structure is shown in Figure 35 with (a) for the cross section of the lens and (b) for the patterned electrode (Ye, Wang, & Sato,

2008). The lens has two layers of LC for higher power. For the patterned electrode, the outer part has a hole (6 mm in diameter in the example) in the center and the inner part is a circular electrode (5.92 mm in diameter). There is a gap between the two parts so that two different voltages V_1 and V_2 can be applied to the outer and inner electrodes, respectively. Similar to the structure described earlier, both positive and negative powers can be obtained. In the positive lens state, V_1 is maintained to 120 V_{rms} and V_2 varies from 30 to 120 V_{rms} , and in the negative lens state, V_2 is maintained to 120 V_{rms} and V_1 varies from 40 to 120 V_{rms} . The power is tuned from 1.5 to -1.1 diopter. To increase the focusing capability of the conventional hole type lens, one approach is to improve the intensity of electric field at the central hollow area. Correspondingly, Chiu, Lin, Chao, and Fuh (2008) proposed a new hole-and-ring type electrode (Figure 36) to improve the distribution of electric field, and it requires lower applied voltage than the conventional one. In the example, the diameter of the hole of the outer electrode is 4 mm, and the ring electrode is inside and cocentered with the hole. The outer radius of the ring electrode is 1 mm. The overall thickness of the LC lens can be as thin as 1.2 mm and the shortest focal length of the 4-mm-aperture lens occurs at 20 cm (5 diopter) under an applied voltage of 30 V at 1 kHz. The inner ring electrode requires only 40% of applied voltage of the external hole electrode.

Using the above hole-pattern electrode structure, although it is possible to increase the lens aperture by increasing the thickness of the substrate between the hole-patterned electrode and the top surface of the LC layer (the ratio of the two parameters are kept between 2 and 3, e.g., 2.6), it is not a practical approach because the driving voltages are almost linearly proportional to the thickness of the substrate, making the voltages too high. A higher dielectric constant substrate may help, but the voltages are still high for lens apertures close to 10 mm. The problem can be alleviated by inserting a layer of material of weak conductivity between the patterned electrode and the LC layer (Ye et al., 2008). The nonuniform electric field induced by the patterned electrode in the cell generates a radial electric current that redistributes the electric charges in the weakly conductive layer. An electric field resulting from the charge redistribution then occurs in the conductive layer in the direction opposite to that of the radial component of the nonuniform electric field created by the patterned electrode. As a result, the abruptly changing potential caused by the patterned electrode is smoothed by the conductive layer. With this structure, for a 15-mm-aperture lens, the thickness between the patterned electrode and the LC layer was reduced from 6 to 0.475 mm (Ye et al., 2008). However, the power of the lens was too low and was tunable only from plano to 0.2 diopter.

2.6. Liquid Crystal Lens Formed by a Glass/Polymer Lens/Shell and Flat LC Layer(s)

When a glass/polymer lens and a LC layer are sandwiched between two electrodes, the thickness variance of the glass/polymer lens gives rise to an inhomogeneous electric field in the LC layer. Different geometries can be used.

Figure 37 shows the LC lens where LC is sandwiched between a flat glass substrate and a plano-convex glass lens (Wang, Ye, Honma, Nose, & Sato, 2002; Wang, Ye, & Sato, 2005c,d). ITO is coated on the top surface of the flat substrate and the spherical surface of the lens. The LC is homogeneously aligned. The spherical electrode generates a gradient

Author Manuscript

Author Manuscript

Author Manuscript

Author Manuscript

electric field distribution in the LC layer. The field is the smallest at the center and the largest at the edge. The tilt of the LC directors near the edge is larger than that of the directors at the center, and the effective refractive index for an extraordinary incident beam is smaller at the edge, producing a parabolic phase profile. The advantage of this structure is that the LC lens aperture can be much larger than that of the lens based on the hole-patterned electrodes. The power tunable range is relatively small, but it can be increased by using thinner substrate between the LC layer and the plano-convex lens, thick LC layer, and spherical electrode of smaller radius of curvature. If the spherical electrode is covered by another substrate with the same curvature and the refractive indices of the materials on both sides are matched (Ren, Fan, Gauza, & Wu, 2004b), the power of the plano-convex lens will be canceled, leaving only the tunable power of the LC cell. Very recently Asatryan et al. (2010) adopted this structure and deliberately selected the dielectric constants of two materials, composing the doublet to improve the performance of the lens with an aperture of 2.5 mm.

An alternative structure based on a plano-concave glass lens is shown in Figure 38 (Wang, Ye, & Sato, 2004). The concave lens is placed on a LC cell with another flat glass substrate between them. The LC directors are homogeneously aligned parallel to the x axis. One electrode is in the LC cell, and the other one is on the top of the glass lens. When a voltage V_0 is applied across the electrodes, an electric field builds up between the electrodes. In the LC, the electric field is weakest at the center and strongest around the aperture edge and is nearly symmetrical about the center. Analogous to the above analysis, the bell-like shape of the phase retardation changes with the applied voltage V_0 . If it takes a quadratic form, then the LC cell behaves as an optical lens with a focal length that is electrically tunable. To enforce the effect, two identical LC layers are used. The structure of the system is shown in Figure 39 (Wang et al.). The LC directors are then aligned homogeneously in one direction. The applied voltage is relatively high and the tunable range of the power is limited (about 1 diopter for a 10-mm aperture with a voltage higher than 100 V).

In the lens structure shown in Figure 37 and that in Ren, Fan, Gauza, and Wu (2004), there is a dielectric material (glass or polymer) between the spherical electrode and the flat glass above the LC layer. The effect of the dielectric material on the electric field is the increased strength of the electric field at the center of the lens, and this reduces the gradient of the electric field within the LC layer. This limits the maximum power of the LC lens for a fixed LC layer thickness. Of course, the lens power can be increased by increasing the thickness of the LC layer for larger phase retardation between the center and the edge of the lens, but that increase results in slower response. The ideal case is that when the LC directors at the border start to reorient with an initial voltage, the distributed voltage at the center is less than or near the threshold. When the voltage gradually increases, the reorientation of the LC directors spread toward the center. In order to achieve this, the region between the spherical electrode and the flat glass (0.55-mm thick) is kept empty (Ren & Wu, 2006), and the ITO electrode is coated on the inner surface of a spherical glass shell. For a 6-mm-aperture lens and 25- μm -thick LC layer, the shortest focal length was 0.96 m at 140 V_{rms} with a response time in the order of 1 s. However, the glass shell is fragile. To improve the mechanic stability, another approach was proposed (Ren, Fox, Wu, & Wu, 2007), where a droplet of UV curable optical adhesive forms a parabolic shape, and a thin layer of conductive polymer is coated on

its surface. In this approach, although region between the curved electrode and the flat substrate is still filled with the polymer, the sag of the polymer was increased, and the thickness of the flat substrate was reduced to 0.2 mm, simultaneously. For a lens with 4.2-mm diameter and 60- μm -thick LC layer, the shorted focal length was 15.4 cm at a much reduced voltage 23 V_{rms} . The response time was about 4 s.

2.7. Modal Liquid Crystal Lens Based on Resistive Electrode

Apart from the hole-patterned electrode, another modal approach to generate smooth continuous electric field distribution and hence the refractive index profile is to use resistive electrode. This method is referred to modal addressing or modal control, which is characterized by a high-resistance transparent electrode (control electrode) and a low-resistance contact at the periphery of the control electrode. Lenses made based on this approach are called modal LC lenses (MLCLs) (Naumov, Loktev, Guralnik, & Vdovin, 1998; Vdovin, Gural'nik, Kotova, Loktev, & Naumov, 1999a,b; Yu et al., 2000).

Figure 40(a) shows the schematic drawing of the MLCL. The LC layer is sandwiched between two glass substrates on which the resistive electrode and the continuous electrode are deposited respectively. The surface resistance of the control electrode is much higher than the resistance of the continuous electrode. The initial uniform orientation of the LC layer is determined by the alignment coatings. The control voltage is applied to contacts located at the control electrode periphery. The contact configuration determinates the type of lens. For spherical lenses, an annular contact is used, and for a cylindrical lens, two linear parallel contacts are used, as shown in Figure 40(b). The control voltage is applied to a low-resistance annular electrode around the active area of the lens. The resultant system with distributed resistance (control electrode) and capacitance (LC layer) is reactive. This makes it possible to control the parameters of an LC cell utilizing both the amplitude and the frequency of the applied voltage. When an AC control voltage is applied to the contacts, the changes in the voltage at the center of the control electrode lag behind the changes in the voltage applied to the contact electrodes because of the resistive-capacitative nature of the system. An increase in the frequency of the applied voltage increases the delay and reduces the rms value of the voltage at the center of the aperture. Under steady-state conditions, the distribution of the rms voltage in the LC layer decreases radially toward the center of the lens because of the potential divider that is formed by the high-resistance control electrode and the capacitance of the LC layer, and the refractive index for the incident extraordinary beam increases from the periphery to the aperture center, forming the phase profile for a lens. In contrast to the lens based on hole-patterned electrode, MLCL responds to both amplitude and frequency of the control voltages, and this offers additional freedom in optimizing the performance of the lens. However, these values need to be carefully selected in order to minimize phase aberrations, caused by both the nonideal distribution of the electrical field across the lens aperture, and the nonlinear electro-optical response of the LC against the applied field. Algorithms for optimization of the applied voltages are presented in Loktev et al. (2000) and Naumov, Love, Loktev, and Vladimirov (1999). For a 5-mm-aperture lens, the focusing power can be tuned from 0 to 3D. Possibility of using the MLCL for intraocular lens has been considered with wireless control (Simonov, Vdovin, & Loktev, 2007; Vdovin, Loktev, & Naumov, 2003; Zhang, Loktev, & Vdovin, 2005). Using this

method, large-aperture lenses can be made. However, the maximum power of the lens that can be realized is limited. It should also be noted that the transmission of the high-resistance electrode may affect the light efficiency of the LC lens.

If the high-resistance control electrode is replaced by a photoconducting layer, whose surface resistance depends on the intensity of the incident radiation, the shape of the wavefront of the new lens can be controlled by varying not only the amplitude and frequency of the applied voltage, but also by changing the profile of the incident intensity. A circular contact can be used to generate a spherical lens while a rectangular contact can be used for a cylindrical lens. Such a lens is called optically addressable modal LC lens (Gural'nik & Samagin, 2003).

2.8. Lens Using Polymer/Liquid Crystal Composites

Addition of a small amount of monomer (about 3%) into LC cell and its in-situ photopolymerization allows controlling the spatial orientation of LC molecules. Such polymer-stabilized LC (PSLC) can be used to fabricate tunable lens with circular-hole-patterned electrodes on one or both substrates of the cell. There is another kind of PSLC that can be used for tunable focus using nonuniform illumination and uniform electric field (Presnyakov, Asatryan, Galstian, & Tork, 2002). In this case, the mixture is homogeneous oriented LC (E7) and few percent (about 3%) of photopolymerizable monomer (e.g., bisphenol-A-dimethacrylate) doped with photoinitiating complex. Homogeneous LC cell with alignment layer was prepared. Exposition of a UV or green laser beam with Gaussian spatial intensity distribution to such a mixture induces a spatially inhomogeneous polymer network (Figure 41, Presnyakov & Galstian, 2005). The higher exposure region results in a higher polymer concentration and smaller LC domains, so the threshold voltage in that region is higher. The electro-optical response of this system to a uniform electrical field creates a nonhomogeneous, centrally symmetric character, and a gradient refractive index lens can be obtained. The Gaussian spatial intensity distribution gives a convex lens. In the previous study, for a lens with 1.5-mm aperture and 10- μm -thick cell, the minimum values of the focal length are 1.6 and 0.8 m for the field frequencies 1 kHz and 60 Hz, respectively. The applied voltage is only a few V_{rms} . In another experiment (Ren & Wu, 2003), a circularly symmetric, continuously variable optical density filter was used as the photomask for illumination. Three percent UV-curable monomer BAB6 (containing 2 wt% photoinitiator IRG184) was mixed in a LC host and the mixture is also named polymer network LC (PNLC). The transmission at the center was the lowest, so a concave phase profile was formed. The radius of the lens was 0.8 cm and the focal length of the lens was very long, ~310 m. Binary Fresnel zone plate using polymer-stabilized LC was also reported (Fan, Ren, & Wu, 2003).

Polymer-dispersed LC (PDLC) is a composite material consisting of LC droplets dispersed in a polymer matrix. The principle of a PDLC lens is based on inhomogeneous droplet size distribution, which is also obtained by exposing the LC/monomer mixture with a gradient UV light. In this case, the UV-curable monomer has a much larger concentration. In one example (Ren & Wu, 2002), monomer NOA-81 (Norland) and LC (E7) was mixed at 70:30 wt% ratio. The area exposed to higher irradiance generates smaller LC droplet size. The

driving voltage of PDLC is inversely proportional to the square root of the LC droplet size. When a uniform voltage is applied to the cell, the LC directors have different degrees of reorientation, and a gradient phase profile can be generated. Depending on the pattern of the irradiance, both positive and negative lens can be formed. If the photomask has the transmission like a binary amplitude Fresnel zone plate, when a uniform voltage is applied, a switchable phase Fresnel zone plate can be formed. Because the nanoscale LC droplets in the polymer matrix are randomly distributed, the lens is polarization independent and exhibits a fast switching time.

Another mechanism of adaptive lens using LC/polymer composite is based on electrically induced LC monomer concentration redistribution (Ren, Lin, & Wu, 2006). LC/monomer mixture consisting of 50 wt% negative nematic LC (ZLI-4788-000, $\epsilon = -5.7$) and 50 wt% liquid monomer (N-vinylpyrrollidone, NVP) was injected into the homogeneous cell. This structure avoids any electric-field induced molecular reorientation. In the absence of an electric field, the LC/monomer mixture is homogeneously distributed. Application of an inhomogeneous electric field causes the LC molecules to diffuse toward the high-field region and the liquid monomer toward the low field region. However, the LC molecules tend to diffuse from high to low concentration direction in order to balance the concentration change. A gradient LC concentration is thus obtained. In the LC-rich region, the surface rubbing aligns the LC molecules and gives an increased refractive index, while the monomer-rich region exhibits a lower refractive index. A tunable-focus lens can be produced. Spherical electrode was used to generate inhomogeneous electric field. However, the focus tunable range is small and the response time of a 25- μm -thick cell has a response time about 3 min for a 9-mm aperture.

A switchable Fresnel zone plate lens was demonstrated using a phase-separated composite film (Fan, Ren, & Wu, 2005). UV curable prepolymer (e.g., NOA 65, Norland) is mixed with a nematic LC (e.g., E48, Merck) with a ratio of 70:30 wt%. The mixture is illuminated by a uniform UV light through an amplitude chromium mask. Phase separation is executed at a temperature of around 100 °C. The phase retardation between the neighboring zones is determined by the effective refractive index of the LC, the thickness of the LC layer, and the thickness of the polymer layer. The effective refractive index of the LC is tuned by the applied voltage. Since the LC and polymer are separated completely to become two layers, there is no light scattering and a relatively low operating voltage is required.

2.9. Microlens with Hybrid Alignment

Two groups developed microlenses based on the patterned orientations of the LC on cell walls (Cheng, Chang, Liu, & Yeh, 2006; Ye, Yokoyama, & Sato, 2006). In the design by Ye et al., the LC lens is prepared using a thin LC layer sandwiched between two planar glass substrates with a transparent electrode on each. The alignment films on the cell walls are treated so that the LC molecules in the overlapped circular areas on both walls align parallel, while those outside the circular areas are perpendicular, to the cell walls (Figure 42). The LC directors inside the layer then gradually change their direction of alignment between the parallel and perpendicular states; a spatially inhomogeneous distribution of refractive index that is nearly axially symmetrical for an incident extraordinary light wave is consequently

formed and a spherical lens is produced. An applied voltage changes the refractive index distribution and hence the optical powers. This method is suitable to make LC lenses of very small size from several to several tens of micrometers with planar LC layers of thickness of approximately 100 μm . Calculated director orientations in plane $y=0$ at $V=0$ and $V=1 \text{ V}$ are shown in Figure 43.

In the design by Cheng, Chang, Liu, and Yeh (2006), hybrid alignment of the LC in the central region is processed with micro-imprinting technology. The imprinted hybrid alignment, which was surrounded by homogeneous (homeotropic) alignment (Figure 44), resulted in spatial refractive-index distribution of liquid-crystal molecules in the microlens. With different hybrid-alignment configurations, the microlens functioned either as a convex (Figure 44(a)) or concave (Figure 44(b)) lens. The focal length of the microlens was electrically controlled at applied voltages of less than 4 V. The focal length was adjusted from 7.8 to 8.6 mm and from -10 to -35 mm for a convex and a concave lens, respectively. The rising response time was 0.5 s, and the falling response time was 5 s.

2.10. Polarization-Independent LC Lens

We have shown that high-performance, polarization-independent lens can be achieved by using orthogonal alignment of two LC layers. For binary phase Fresnel zone plate, several articles have addressed this issue by using orthogonal alignment of the LCs in the neighboring subzones. One technique is to control the alignment layer of the neighboring subzones for the side of patterned electrode and use homeotropic alignment on the other side with continuous electrode (Kim, Yu, Kim, Kim, & Lee, 2006; Patel & Rastani, 1991). The other technique is based on double-side photoalignment of azo-dye (Methyl Red) doped LCs (e.g., E7) (Lin, Jau, Lin, & Fuh, 2007). Before the LC cell is assembled, the two ITO-coated glass substrates are slightly rubbed with cloth. Methyl Red dyes may undergo photo-isomerization between the trans-isomer and the cis-isomer. Azodyes are usually in the stable trans-state in the dark. When the dye-doped LC cell is excited by light in the absorption spectrum range at the room temperature, the dyes are transformed from the trans to the cis form, inducing the diffusion, and adsorption onto the substrate facing the incident pump beam with the long axes of dyes being perpendicular to the pump-beam polarization after many trans-cis transformation cycles. The adsorbed dyes then align LCs. The adsorption of dyes can be made onto both of the two substrates of the cell, if the cell is optically excited at a temperature just above the clear temperature of LC. Detailed procedures can be found in Lin et al. (2007). Other materials such as polymer-dispersed LCs and cholesteric LCs may be used for polarization-independent lens. However, the required voltage is high and the general performance is not good enough.

3. ADAPTIVE LIQUID LENS

Adaptive liquid lens offers the variable focus by changing the shape of the liquid. Based on the operation mechanism, adaptive liquid lenses can be classified into four types: fluid-membrane interaction, electrowetting effect, dielectrophoretic effect, and thermal effect.

3.1. Liquid Lenses Based on Fluid-Membrane Interaction

This kind of liquid lens consists of a liquid-filled chamber, which is formed by two elastic membranes or one membrane and one support frame. The principle of this lens is similar to that of the accommodating lens inside the human eye or other animal eyes, and sometimes it is called bioinspired fluidic lens. By changing the pressure of the liquid, the shape of the liquid lens is changed as a result of the deformation of the membrane and hence the focal length can be varied. The most widely used flexible polymer membrane material is poly(dimethyl siloxane) (PDMS, 10:1 mixing ratio of the monomer and a curing agent, Sylgard 184, Dow Corning, MI). In 1968, Wright proposed the idea of liquid-filled varifocal lens (Wright, 1968). Shortly after that Knollman, Bellin, and Weaver (1970) investigated theoretically the shape of the membrane-encapsulated liquid-filled lens and it is a parabola. Later on Sugiura and Morita (1993) analyzed the effect of gravity on the lens shape and the aberration of the lens. The effect of gravity and the aberration can be negligibly small by selection of optimized materials and parameters such as the lens diameter, hydraulic pressure, and liquid density. Rawicz and Mikhailenko (1996) developed a mathematical model that calculates the absolute value of the tension in the membrane and experimentally verified it. Chronis, Liu, Jeong, and Lee (2003) fabricated tunable liquid microlens array by soft lithographic technique, and simultaneous control of the focal length of all the microlenses was accomplished by pneumatically regulating the pressure of the microfluidic network. Tunable microdoublet lens array capable of creating dual modes of biconvex or meniscus lens was demonstrated (Jeong, Liu, Chronis, & Lee, 2004). Zhang, Lien, Berdichevsky, Choi, and Lo (2003) demonstrated a 20-mm-aperture lens with wide range focal length (41–172 mm) adjusted and controlled by a syringe pump. Lenses based on the similar mechanism were also reported in Marks, Mathine, Peyman, Schwiegerling, and Peyghambarian (2009). In 2004, Zhang also demonstrated plano-convex and biconvex lenses with a tunable focus range from 30 mm to infinity (Zhang, Justis, Lien, Berdichevsky, & Lo, 2004). Chen, Wang, Fang, and Varahramyan (2004) designed a polymer microlens with higher numerical aperture (up to 0.24) by using a thin PDMS diaphragm with 3D convex lens, a silicon chamber, and a PDMS chamber block with an inlet channel. For 1.4-mm aperture, the focal length can be tuned from 3.8 to 10.6 mm. Agarwal, Gunasekaran, Coane, and Varahramyan designed and fabricated microlenses with a wide field-of-view (FOV) and large numerical aperture using standard photolithographic and silicon micromachining techniques. Fluidic pressure was applied by an external syringe pump. This lens system is capable of working in dual mode, forming either a double convex (DCX) or a double concave (DCV) lens. The focal length could be tuned in the range from 75.9 to 3.1 mm and from -75.9 to -3.3 mm for the DCX and DCV lens configurations, respectively. The FOV for this lens system was found to be in the range of 0.12–61° for DCX lens and 7–69° for DCV lens. The smallest *F*-number that could be achieved using this dynamic lens is 0.61, which corresponds to the numerical aperture value of 0.64. Based on the same mechanism, Kuwano, Tokunaga, Otani, and Umeda (2005) were able to continuously change the shape of the lens from concave to convex. A schematic diagram is shown in Figure 45. When the liquid is injected into the lens, the pressure increases as shown in Figure 45(a), and both lens surfaces expand into a convex shape. When the liquid is discharged from the lens, the refraction surface is reformed to a concave shape as shown in Figure 45(b). This kind of lens was also demonstrated by Moran et al. (2006). A microfluidic device that operates as a set of

two adaptive cylindrical lenses focusing light along two orthogonal axes was demonstrated by Pang, Levy, Campbell, Groisman, and Fainman (2005). The device is made out of PDMS using soft lithography, and consists of a few chambers separated by flexible membranes and filled with liquids of different refractive indices. The cylindrical lenses can be both converging and diverging; their focal lengths are varied independently and continuously adjusted between -40 and 23 mm by setting pressure in the chambers. An adaptive lens by changing the effective aperture of the liquid was proposed by Ren and Wu (2005). The lens consists of an elastic membrane, a solid plate, and an annular sealing ring which looks like an iris diaphragm; a liquid with a fixed volume is stored in lens chamber. The surfaces of annular sealing ring are sealed with an elastic membrane. The radius of the annular sealing ring is changeable. By tuning the radius of the annular sealing ring, the stored liquid in the lens will be redistributed, thus changing the curvature of the elastic membrane. Therefore, the lens cell causes light to converge or diverge.

The lens cell may consist of a lens chamber connected to a reservoir, both covered by elastic membranes. By pushing the membrane of the reservoir, the liquid of the fixed volume will be redistributed and consequently the fluid pressure deforms the membrane of the lens chamber. Various techniques for implementation of the fluidic pressure have been proposed. For example, a servo-motor can be used to push the membrane of the reservoir from the side of the lens (Ren, Fox, Anderson, Wu, & Wu, 2006). Deformation of the membrane can also be implemented by a piece of photo-polymer, which can bend under the influence of polarized light (Yu, Nakano, & Ikeda, 2003). Such a polymer contains azobenzene LC moieties. When the photo-sensitive polymer is attached to the membrane of the reservoir and exposed to polarized blue light, the polymer is bent, exerting fluid pressure for the change the focal length of the plano-convex lens (Xu et al., 2009). However, the response of the lens is slow (approximately a few seconds). In order to achieve high-speed focusing, a piezo stack actuator with a built-in motion amplifier has been used to rapidly deform the membrane and 1-kHz bandwidth was achieved (Oku, Hashimoto, & Ishikawa, 2004). Two pneumatically actuated adaptive lenses with a 2-ms response time and a 4-diopter variation of power have been demonstrated (Campbell, Fainman, & Groisman, 2007). The two membranes are 18 and 12 mm in diameter and the effective aperture of the two lenses are 5 and 3.3 mm, respectively. A pinned-contact oscillating liquid lens working at 100 Hz with a small scale (1–2 mm aperture) has been reported (López & Hirsa, 2008). Electrochemical (López, Lee, & Hirsa, 2005) and electromagnetic (Lee & Lee, 2007) actuators have also been proposed for implementation of small-scale lens. Recently, Li and Fang (2010) have demonstrated compact, low-cost adaptive lenses actuated by electromagnetic solenoid. The lens apertures are all larger than 10 mm and the lenses show large tunable power (over 30 diopters) and high performance. A novel structure for electromagnetic solenoids was designed, which allows much larger electromagnetic force. As shown in Figure 46, there are two holes in the plastic substrate and they are connected by a channel. They serve as the reservoir and the lens chambers respectively. The top surfaces of the two chambers are covered by soft materials such as elastic rubber or PDMS membrane. The bottom surface of the lens is covered by glass or another PDMS membrane. The required DC voltage is only a few volts.

Apart from the continuously tunable lens, a 4-bit digital liquid lens for variable focal length using a 4-bit actuator (b_1 , b_2 , b_3 , and b_4 bit actuators) has been demonstrated (Lee & Cho, 2010). The 4-bit actuator, where 1, 2, 4, and 8 unit pneumatic actuators are serially connected with binary-combination, pushes a discrete fluidic volume into the lens in 2^4 different levels. Thus, the 4-bit digital actuation mode ($b_4 b_3 b_2 b_1$) from (0000) to (1111) makes $2^4 = 16$ different levels of lens curvature and focal length.

Most of the adaptive liquid lenses focus light perpendicular to the plane of the substrate (out-of-plane). A structure for tunable microlens that can focus light in the plane of the substrate (in-plane) was proposed by Shi, Stratton, Steven, Huang, and Huang (2010). The in-plane tunable microlens is critical for lab-on-a-chip devices.

In most of the systems demonstrated, simple models assuming spherical surfaces have been used.

Although this model is not accurate, to first order this approximation is useful in determining the basic focal length. A schematic drawing for the plano-convex lens shape is shown in Figure 47. The dependence of the focal length on the liquid volume and lens contact angle can be calculated using the lens formula. From thin lens equation,

$$\frac{1}{f} = (n - 1) \left(\frac{1}{R_1} - \frac{1}{R_2} \right), \quad (3.36)$$

when $R_2 \rightarrow \infty$, the following equation is obtained:

$$f = R_1 / (n - 1). \quad (3.37)$$

Referring to Figure 47, assume the lens diameter D , sag height h , and contact angle $\theta = \beta + \gamma$. We have

$$R = \frac{D^2 + 4h^2}{8h}, \quad (3.38)$$

$$\alpha = \tan^{-1} \left(\frac{R - h}{D/2} \right), \quad (3.39)$$

and

$$\beta = \tan^{-1} \left(\frac{h}{D/2} \right). \quad (3.40)$$

Then

$$\gamma = 90^\circ - \alpha - \beta = 90^\circ - \tan^{-1} \left(\frac{2R - 2h}{D} \right) - \tan^{-1} \left(\frac{2h}{D} \right). \quad (3.41)$$

Therefore, the contact angle θ equals to

$$\begin{aligned}
\theta = \beta + \gamma &= 90^\circ - \tan^{-1} \frac{2R - 2h}{D} \\
&= 90^\circ - \tan^{-1} \left[\frac{2 \left(\frac{D^2 + 4h^2}{8h} \right) - 2h}{D} \right] \\
&= 90^\circ - \tan^{-1} \left[\frac{1 - \left(\frac{h}{D} \right)^2}{\frac{4h}{D}} \right].
\end{aligned} \tag{3.42}$$

The volume of the liquid that enters the lens chamber can be express by

$$\Omega = \frac{\pi R^3}{3} (2 + \cos\theta)(1 - \cos\theta)^2, \tag{3.43}$$

and the focal length f is equal to

$$f^3 = \frac{3\Omega}{\pi(1 - \cos\theta)(2 - \cos^2\theta - \cos\theta)(n_L - 1)^3}, \tag{3.44}$$

where n_L is the refractive index of the liquid.

The maximum deflection h of the membrane is derived by

$$w_0 = 0.662 \left(\frac{a \Delta P}{Et} \right)^{1/3}, \tag{3.45}$$

where P is the pressure drop, a is the radius, t is the thickness, and E is the elastic modulus of a membrane. The equation shows that the maximum deflection is proportional to the cube root of the pressure and inversely proportional to the cube root of the thickness.

As a result of edge-bonding conditions and finite film stiffness, the surface of the membrane is not exactly a sphere. A higher-order shape function is needed to design precise optical systems. A parametric mechanical model is first developed for the deformation by Yang, Kobrin, Seabury, Narayanaswamy, and Christian (2008), based on the geometric dimensions and film properties including thickness, boundary conditions, modulus, and prestrain. The material constants are then extracted from a comparison with simple point measurements on real devices at various pressures. Those values are then inserted into a finite-element model to predict the precise shape over a wide range of operating conditions. This form is then fitted with a standard optical lens shape function to obtain the radius of curvature and the conic constant, which are used for accurate optical design. Several articles have characterized the aberrations of the liquid lenses (Feng & Chou, 2009; Schneider, Draheim, Kammerer, Waibel, & Wallrabe, 2009; Schneider, Müller, & Wallrabe, 2008; Shaw & Sun, 2007; Werber & Zappe, 2005). A design method for correcting chromatic as well as spherical aberrations of variable-focus, multichamber liquid lenses was presented by Reichelt and Zappe (2007). By combining suitable optical liquids with appropriate radii of the liquid's interfaces, liquid lenses with superior, diffraction-limited resolution over a wide

focal tuning range are possible. Wang, Xu, and Zhao (2007) showed that a two-group liquid lens system is the simplest one that contains no moving mechanical parts and has enough parameters to correct all chromatic aberrations for any focal length and most monochromatic aberrations for certain focal lengths.

3.2. Liquid Lenses Based on Electrowetting Effect

The electrowetting effect (Minnema, Barneveld, & Rinkel, 1980) can be explained with reference to Figure 48, where a droplet of conductive liquid partially wets a solid insulator film of thickness d and dielectric constant ϵ_r and a voltage is applied between the liquid and a counter-electrode beneath the insulator. The contact angle θ of the droplet on the surface will be modified according to the Young–Laplace equation (Vallet, Berge, & Volvelle, 1996)

$$\cos\theta(V) = \cos\theta_0 + \frac{\epsilon_0\epsilon_r}{2d\gamma_{LV}}V^2, \quad (3.46)$$

where V is the applied voltage, θ_0 is the initial contact angle at 0 V, γ_{LV} is the surface tension of the liquid-surrounding media interface, ϵ_r is the permittivity of the dielectric substrate, ϵ_0 is the permittivity of the vacuum, and d is the distance that separates the electrode and the liquid–solid interface. This effect has been studied in other articles such as Gorman, Biebuyck, and Whitesides (1995), Verheijen and Prins (1999), and Welters and Fokkink (1998). The contact angle can be modified by more than 50°. The insulating layer minimizes the electrolysis of the conductive liquid and reduces the Joule heating effect and the microbubbles.

A direct application of this effect is to use the liquid drop as an optical lens (Figure 49(a), Krupenkin, Yang, & Mach, 2003). Changes of the contact angle of the drop induce changes of the radius of curvature of a liquid–liquid interface, changing its resulting focal length, which is determined by the contact angle θ , the droplet volume Ω , and the refractive indices of the liquid and the surrounding media as

$$f^3 = \frac{3\Omega}{\pi(1 - \cos\theta)(2 - \cos^2\theta - \cos\theta)(n_L - n_V)^3}, \quad (3.47)$$

where n_L is the refractive index of the liquid and n_V is the refractive index of the surrounding media. The counter-electrode can also be divided into several subelectrodes and ground electrode (Figure 49(b)), and by applying different voltages to these subelectrodes, the droplet can be moved toward the higher-voltage electrode, and hence, the location of the droplet can be adjusted. However, the conductive liquid is exposed to the air, and the evaporation of the liquid could be a problem. To overcome the problem, electrowetting lenses using two immiscible liquids inside a chamber have been studied as described later (Berge & Peseux, 2000; Kuiper & Hendriks, 2004; Liu, Park, & Choi, 2008).

Figure 50 (Berge & Peseux, 2000) shows the schematic drawing of the lens cell with two nonmiscible liquids, one insulating and nonpolar, and the other a conducting water solution. The liquids are transparent with different indices of refraction, but with the same density so that gravity does not deform the liquid–liquid interface, which remains spherical to any

Author Manuscript

Author Manuscript

Author Manuscript

Author Manuscript

orientation of the cell. The insulating liquid has the shape of a drop in contact with a thin insulating window (in gray in Figure 50), which is hydrophobic so that naturally the insulating liquid will sit on it. The transparent counter-electrode is deposited on the external side of the window. The outer zone is treated to be hydrophilic so that when no voltage is applied, the drop maintains in shape A. Application of a voltage between the counter-electrode and the conducting liquid favors the wettability of the surface by the same liquid. This deforms the interface from shape A to shape B and thus changes the focal length. Figure 51 (Kuiper & Hendriks, 2004) shows a self-centered lens using two immiscible liquids. The cylindrical glass housing is coated with a transparent electrode, which is formed of 50-nm ITO. The inside of the cylinder is coated with a hydrophobic insulator (The insulator is a 3-mm-parylene-*N*layer, and the 10-nm-hydrophobic top coating is a dipcoated fluoropolymer, AF1600 supplied by Dupont). The counter electrode is in direct contact with the conducting liquid. The top and bottom glass plates are glued onto the glass cylinder with epoxy glue. When a voltage is applied between the electrodes, charges accumulate in the wall electrode and opposite charges collect near the solid/liquid interface in the conducting liquid and this results in an electric field across the insulator, which effectively lowers the interfacial tension between the conductive liquid and the insulator and hence the contact angle. The resulting change in contact angle of the conducting liquid with the wall changes the focal length of the lens. However, the out-of-plane electrode in the lens design limited its application in integrated microsystems as vertical metal deposition in microfabrication is often difficult to achieve. To avoid this issue, a planar liquid lens design based on electrowetting of two immiscible liquids with two ring-type electrodes beneath the hydrophobic surface has been reported (Figure 52, Liu et al., 2008). As shown in Figure 52, the outer ring electrode, when applied with an electric potential, electrowets the area above it and changes the surface property. This provides an initial boundary to confine the insoluble oil droplet. If this voltage was not applied before the placement of the oil, it could easily disperse on the hydrophobic surface. The inner ring, however, is the actuation electrode of the lens. When an electric voltage is applied to the inner electrode, the surface above becomes hydrophilic and attracts the surrounding aqueous solution. The aqueous solution deforms the shape of the confined oil droplet, which means changing the focal length of the optical lens.

These electrowetting lenses typically have an aperture about 3 mm and the tunable focal range about 10 mm. But the insulating layer induces electric field shielding effect and increases the driving voltage. Usually they require high voltages up to a few hundred voltages. Very recently an electrode-less and circuitless microlens array configuration was proposed based on the electrowetting effect in pyroelectric periodically poled crystals (Grilli et al., 2008; Miccio et al., 2009; Miccio, Paturzo, Grilli, Vespi, & Ferraro, 2009). Lens effect was obtained in an open microfluidic system by using a thin layer of liquid on a polar electric crystal like LiNbO₃. Because of the pyroelectric effect of the crystals, a temporary voltage is generated when they are heated or cooled. An array of liquid micro-lenses was observed during heating and cooling treatments. The response time is in the order of seconds, which is slower than the earlier lenses using external applied voltages.

3.3. Liquid Microlenses Based on Dielectrophoretic Effect

Nonuniform electric fields exert a dielectrophoretic force on polarizable media including liquids (Jones, Gunji, Washizu, & Feldman, 2001). The liquids respond to a nonuniform electric field by collecting preferentially in regions of maximum field intensity. With properly designed electrodes, the DEP effect may be exploited to control and manipulate small water volumes. The structures of the microlenses based on the dielectrophoretic effect have some similarities to those based on the electrowetting effect. Either one liquid or two immiscible liquids can be used. However, for electrowetting lenses, one liquid must be conductive. In contrast, the liquid(s) used for dielectrophoretic lenses are nonconductive, and when two liquids are used, they have different dielectric constants. Moreover, there are no electrolysis, microbubbles and Joule heat that may appear in electrowetting lenses. Several kinds of dielectrophoretic microlenses have been demonstrated using different methods to generate inhomogeneous electric field, including patterned ring electrodes, hole-patterned electrode, continuous flat electrode, and curved electrode on a concave lens surface.

The first dielectric microlens (Cheng, Chang, & Yeh, 2006) used nonconductive LC as the high-dielectric medium and patterned ring electrodes to generate the inhomogeneous field, as shown in Figure 53. Because of the birefringence of the LC, it must be operated in the isotropic phase (temperature exceeding 23.5° of the transition temperature between the nematic phase and the isotropic phase). The ITO electrodes of 50 μm in width and 50 μm in spacing were fabricated on a glass wafer, followed by Teflon coating, which functions as a hydrophobic layer to increase the contact angle of the LC droplet. The dielectric force is given by the Kelvin theory (Haus & Melcher online material)

$$F = \frac{\epsilon_0}{2}(\epsilon_{\parallel} - 1)\nabla(E \bullet E), \quad (3.48)$$

where ϵ_{\parallel} and ϵ_0 are the permittivities of the LC and free space, respectively. E denotes the electric field intensity. For a lens aperture less than 2 mm, the focal length varied from 1.6 to 2.6 mm in the voltage range of 0–200 V at 1 kHz. In order to allow for operation of the dielectric lens at the ambient temperature that is less than the transition temperature of the LC, two new liquids were used to replace LC (Cheng & Yeh, 2007). As shown in Figure 54, the new lens consists of a liquid droplet with a low-dielectric constant and a sealing liquid with a high-dielectric constant. The bottom diameter of the droplet was 7 mm when no voltage was applied. The two liquids were injected inside a 3-mm-thick PMMA (polymethyl methacrylate) chamber that was sealed between two ITO glass substrates. The mass density of the sealing liquid was matched to that of the droplet to minimize the gravitational effect for better optical quality. As the voltage was applied, a dielectric force exerts on the droplet because of the difference in the dielectric constant between the two liquids. In this case, the dielectric force is given by

$$F = \frac{\epsilon_0}{2}(\epsilon_1 - \epsilon_2)\nabla(E \bullet E), \quad (3.49)$$

where ϵ_1 and ϵ_2 are the permittivities of the sealing liquid and the droplet, respectively. The dielectric force shrinks the droplet toward the region where the electric field is weaker,

increasing the droplet's contact angle and shortening the focal length of the liquid lens. The refractive indices were 1.4 and 1.6 for the sealing liquid and the droplet (optical fluids SL-5267, SantoLight™), respectively. The two liquids had a difference in dielectric constant of about 35. The focal length of the 3-mm-aperture lens was tuned from 34 to 12 mm in the range of 0–200 V. The rise time was measured to be about 650 ms and the measured fall time was 300 ms. To reduce the applied voltage, two liquids with a large difference in dielectric constants should be used. Following this operation mechanism, a hole-patterned array electrode is used to substitute for the patterned ring electrodes to make dielectric microlens array (Ren & Wu, 2008). The aperture of each hole is 140 μm and the gap between the adjacent holes is 100 μm. A thin polyimide layer was coated on the hole-patterned electrode surface, and two liquids were chosen: diacrylate monomer AE-93 ($n \sim 1.46$ and $\epsilon_1 \sim 5$) for the droplet and deionized water ($n = 1.33$, $\epsilon_2 \sim 80$) for the sealing liquid. The focal length can be changed from 1.45 to 2.1 mm. The rise time was measured to be ~30 ms and the fall time ~250 ms.

Ren, Xianyu, Xu, and Wu (2008) also showed that if the droplet and the sealing liquid are sandwiched between two flat electrodes as shown in Figure 55, the electric field across the droplet is inhomogeneous. The electric field inside the droplet with a height t is given by

$$E_t = \frac{V/\epsilon_2}{t/\epsilon_2 + (d-t)/\epsilon_1 + d_p/\epsilon_p}, \quad (3.50)$$

where ϵ_p is the dielectric constant of the polymer layer, d is the cell gap, and d_p is the thickness of the polymer layer. If the polymer layer is very thin, i.e., $d_p \rightarrow 0$, the effect of d_p/ϵ_p on E_t is negligible. Then, the electric field at the boundary of the droplet can be approximated as

$$E_{t \rightarrow 0} = \frac{V\epsilon_1}{d\epsilon_2}. \quad (3.51)$$

If the sag of the droplet approaches the cell gap, i.e., $t \rightarrow d$, the electric field at the center of the droplet can be approximated as

$$E_{t \rightarrow d} = \frac{V}{d}. \quad (3.52)$$

The above two equations indicate that the electric field at the boundary of the droplet is ϵ_1/ϵ_2 times stronger than that at its center. The electric field changes continuously in between them. With $\epsilon_p = 4$, $d_p = 0.8 \mu\text{m}$, $\epsilon_1 = 47$ (NOA81), $\epsilon_2 = 1.672$ (SantoLight Optical Fluids SL-5267), $d = 110 \mu\text{m}$, droplet diameter = 230 μm, the focal length was changed from 620 μm at $V = 0 \text{ V}_{\text{rms}}$ to 500 μm at $V = 90 \text{ V}_{\text{rms}}$. To enhance the gradient of the electric field across the droplet and hence the dielectric force (Figure 56, Xu et al., 2009), the bottom electrode is replaced by a curved electrode on a plano-concave polymer lens base formed by a glass plano-convex microlens array stamper. The curved electrode not only fixes the position of the microlens, but also reduces the driving voltage. Furthermore, the polymer layer is not necessarily required in this case, which simplifies the fabrication process and

Author Manuscript
Author Manuscript
Author Manuscript
Author Manuscript

minimizes the electric field–shielding effects. Using the same liquids and the concave polymer lens with a radius of curvature of 1 mm and an aperture of 0.75 mm, the focal length was tuned from 2.5 mm at $V=0$ to 1.39 mm at $V=88 V_{\text{rms}}$. The relaxing speed is slow (~0.5 s), which can be improved using low-viscosity liquids.

3.4. Liquid Microlenses Based on Hydrogel and Thermal Effect

Liquid microlenses actuated by hydrogel responding to pH, temperature, or infrared light have been demonstrated (Dong, Agarwal, Beebe, & Jiang, 2006, 2007; Zeng & Jiang, 2008). In these devices, microstructures made of pH-, thermal-, or light-responsive hydrogel were used to regulate the curvature of a liquid–liquid interface to form tunable microlenses. An example is shown in Figure 57. The basic design consists of a stimuli-responsive hydrogel ring placed within a microfluidic channel system, and sandwiched between a glass plate and an aperture slip, the latter with an opening centered over the ring. The microchannels are filled with water, and oil is placed on top of this structure and capped with a glass coverslip. The sidewall and bottom surface of the aperture ('ca' in Figure 57(b)) are hydrophilic and the top surface ('ts' in Figure 57(b)) is hydrophobic, which ensures that the water–oil meniscus is pinned along the hydrophobic–hydrophilic contact line 'ca-ts' (that is, the top edge of the aperture opening). When exposed to an appropriate stimulus (which could be pH, temperature, light, an electric field, and so on), the hydrogel ring underneath the aperture opening responds by expanding or shrinking, owing to the absorption or release of water via the hydrogel network interstitials; this leads to a change in the volume of the water droplet located in the middle of the ring. The net volume changes – the change in the volume enclosed by the ring, and the change in water droplet volume – cause a change in the pressure difference P across the water–oil interface, with P directly determining the geometry of the liquid meniscus. Because the contact line of the meniscus is pinned and stationary, volume changes are translated into a change in curvature and hence angle (Figure 57(b)), which determines the focal length of the microlens. Another thermal responsive material poly-*N*-isopropylacrylamide (PNIPAAm) has been encapsulated into monodisperse microcapsules for microlens array (Yang, Han, Zhao, Nagai, & Gu, 2006). The size, embedding efficiency, and wall thickness of the microcapsules are controllable. The monodisperse microcapsules were hexagonally packed to form microlens array via a self-assembly process. The imaging capability is controlled by temperature.

4. EXAMPLES OF APPLICATIONS OF THE ADAPTIVE LENSES

Adaptive liquid crystal and liquid lenses have been applied for ophthalmic lens, zoon lens, aberration compensation, biomedical imaging, optical tweezers, beam steering, fiber coupling, and so on. Here we only list a few examples.

4.1. Correction of Presbyopia

Presbyopia is an age-related loss of accommodation of the human eye that manifests itself as inability to shift focus from distant to near objects. Assuming no refractive error, presbyopes have clear vision of distant objects; they require reading glasses for viewing near objects. Area-divided bifocal lenses are one example of a treatment for this problem. However, the field of view is limited in such eyeglasses except the bifocal diffractive lens (Futhey, 1989),

requiring the user to gaze down to accomplish near vision tasks and in some cases, causing dizziness and discomfort. Some users need three different eyeglasses for reading, computer, and driving. Progressive lenses cause some distortion. By using the new switchable, flat, liquid crystal diffractive lenses that can adaptively change their focusing power, we have assembled the prototypes of adaptive eyewear, one can be switched between plano, 1-diopter and 2-diopter (Figure 58), and the other can be switched between plano, 2-diopter, and 4-diopter (Figure 59). The operation of these spectacle lenses is based on electrical control of the refractive index of a 5- μm -thick layer of nematic liquid crystal using a circular array of photolithographically defined transparent electrodes. It operates with high transmission, low voltage ($<2 V_{\text{RMS}}$), fast response ($<1 \text{ s}$), diffraction efficiency exceeding 90% at eight phase levels, small aberrations, and a power-failure-safe configuration. These results represent significant advance in the state-of-the-art in liquid crystal diffractive lenses for vision care and other applications. They have the potential of revolutionizing the field of presbyopia correction when it is combined with automatic adjustable focusing power. In addition, Professor Josh Silver at Oxford University has developed adaptive eyewear using liquid lens and it has been commercialized with the main market in the undeveloped countries. Besides the adaptive spectacle lenses, accommodative intraocular lens has been proposed using the tunable liquid lens (Qiao, Tsai, Cho, Yan, & Lo, 2009).

4.2. Zoom Lens, Optical Tweezer, and Biomedical Imaging

An optical zoom lens is a system that can vary the magnification of focal length while keeping the image plane fixed. As described in the introduction section, replacing the moving optics with stationary adaptive lens can simplify the system, reduce the size and power consumption, and eliminate vibration caused by conventional mechanic movement. Changing the magnification or focal length of an imaging system can be accomplished by using one or multiple adaptive lenses. An optical zoom lens based on two LC spatial light modulators and a few more conventional lenses has been analyzed by Tam (1992), and a design with $3.9\times$ zoom was presented by Wick and Martinez (2004). In the design by Zhang, Justis, and Lo (2005), two fluidic lenses were used to achieve a zoom ratio higher than 4.0. In another design, the zoom lens system consists of one lens with fixed power followed by two double-liquid variable-focus lenses (Peng, Chen, Zhu, & Zhuang, 2007). Recently Ye, Noguchi, Wang, and Sato (2009) demonstrated a zoom lens system by using one glass lens in between two LC lenses and a zoom ratio 1.5 was achieved. Micro-zoom arrays have been used for parallel focusing in integral imaging (Tolosa et al., 2010).

A laser-manipulation system using a LC lens with variable-focusing and beam deflection functions for the transmitted laser beam has been demonstrated by Kawamura, Ye, and Sato (2005). Three-dimensional trapping and manipulation of microscopic particles can be realized by focusing and deflecting the laser beam, and the position of the captured particles can be controlled by adjusting the applied voltage without any mechanical movements. Hands, Tatarkova, Kirby, and Love (2006) used different LC elements to provide full three-dimensional particle control in an optical tweezer. The transmissive LC devices could be retro-fitted to an existing microscope system. An adaptive modal LC lens is used to vary the z -focal position over a range of up to 100 μm and an adaptive LC beam-steering device is

used to deflect the beam (and trapped particle) in the $x-y$ plane within an available radius of 10 μm .

Confocal laser scanning fluorescence microscopy has been an indispensable tool for live cell imaging. Rapid data acquisition with high resolution and nontranslational components is extremely important for 3D microscopic imaging, especially live-cell imaging where dynamic behaviors inside cells need to be recorded in real time for better understanding of the cell functions. Very recently a nontranslational parallel 3D confocal optical imaging system equipped with an electro-optic varifocal lens for rapid depth scanning and digital micromirror device for parallel transverse confocal scanning and hence fast image acquisition has been presented by Li, Fang, and Zhao (2010).

4.3. Aberration Correction

The next-generation data storage system will use shorter wavelength (blue light), multiple recording layers, and objective lens with higher numerical aperture. These factors increase the sensitivity of the optical pickup to the spherical aberration, which is mainly due to the variation of the substrate thickness and the switching between layers, as the objective lens can be compensated only for a single-layer thickness. LC lenses have been used as a nonmechanical device to compensate the spherical aberration (Hain et al., 2001; Ohtaki, Murao, Ogasawara, & Iwasaki, 1999; Stallinga, Vrehen, Wals, Stapert, & Verstegen, 2000), but they have low tolerance with regard to lateral adjustments of the LC device into the light path and a comparatively high number of driving electrodes is required. For example, in the latter case, a convex LC lens and a circular electrode structure with 64 ring electrodes were used in dual-layer digital versatile discs (DVDs). Somalingam et al. (2004) proposed a method for effective compensation of spherical aberration by utilizing a novel LC device that generates a parabolic wave front. This particular shape makes the element highly tolerant against lateral movements. By enhancing the method of conductive ladder mashing for electrode design, the number of driving electrodes is reduced to only two. Chung, Choi, Kim, Ahn, and Baik (2006) designed and fabricated a novel structure of the LC lens having both the concave and convex surfaces for spherical aberration compensation. The structure was able to improve the shift tolerance characteristics of the objective lens and increase the compensation range to a three-layer recording disk. Examples of the other applications of adaptive lens include beam steering, (Masuda, Takahashi, Nose, Sato, & Ito, 1997), fiber optic device (Reza & Riza, 2009), and so on. Spatial light modulators have been used as a programmable lens for imaging (Gruneisen, DeSandre, Rotge, Dymale, & Lubin, 2004; Laude, 1998), information processing (Davis, Valadéz, & Cottrell, 2003; Love et al., 2009; Takaki & Ohzu 1996), and vision correction (Fernández, Prieto, & Artal, 2009). Quite a few articles are on fabrication and applications of adaptive microlens array and the details are not presented here. Adaptive microlenses are very useful for optofluidic, lab-on-a-chip, and micro-total-analysis systems.

5. CONCLUSION

A lot of efforts have been devoted to the research in adaptive lens. Recent advances in this field have been reviewed in this article. For liquid crystal lens, refractive and diffractive LC

lenses based on discrete electrodes, hole-patterned electrodes, modal control electrode, hybrid alignment, polymer/LC materials have been discussed in detail. For liquid lenses, lenses based on mechanic pressure, electrowetting effect, dielectric effect, hydrogel and thermal effect have been reviewed. Examples of applications in vision care, aberration compensation, zoom lens, and optical tweezers have been discussed. To fabricate large-aperture low-aberration adaptive LC and liquid lenses are still challenging. We look forward to new developments in this active area.

ACKNOWLEDGMENTS

I would like to acknowledge the Wallace H. Coulter Foundation, National Institutes of Health, and University of Missouri Research Board for partially supporting my current research.

REFERENCES

- Agarwal M, Gunasekaran RA, Coane P, & Varahramyan K (2004). Journal of Micromechanics and Microengineering, 14, 1665.
- Alvarez LW (1967). U.S. Patent No. 3,305,294.
- Alvarez LW (1978). Journal of the American Optometric Association, 49(1), 24. [PubMed: 342589]
- Alvarez LW, & Humphrey WE (1970). U.S. Patent No. 3,507,565.
- Apter B, Efron U, & Bahat-Treidel E (2004). Applied Optics, 43, 11. [PubMed: 14714638]
- Asatryan K, Presnyakov V, Tork A, Zohrabyan A, Bagramyan A, & Galstian T (2010). Optics Express, 18, 13981. [PubMed: 20588530]
- Back FG, & Lowen H (1954). Journal of the Optical Society of America, 44, 684.
- Back FG, & Lowen H (1958). Journal of the Optical Society of America, 48, 149.
- Barbero S (2009). Optics Express, 17, 9376. [PubMed: 19466190]
- Barton IM, Dixit SN, Summers LJ, Thompson CA, Avicola K, & Wilhelmsen J (2000). Optics Letters, 25, 1. [PubMed: 18059762]
- Berge B, & Peseux J (2000). European Physical Journal E, 3, 159.
- Bergstein L (1958). Journal of the Optical Society of America, 48, 154.
- Bernet S, & Ritsch-Marte M (2008). Applied Optics, 47, 3722. [PubMed: 18641736]
- Born M, & Wolf E (1999). Principles of optics. Oxford: Pergamon.
- Bricot C, Hareng M, & Spitz F (1977). U.S. Patent No. 4,037,929.
- Brinkley PF, Kowal ST, & Chu C (1988). Applied Optics, 27, 4578. [PubMed: 20539611]
- Burch JM, & Williams DC (1977). Applied Optics, 16, 2445. [PubMed: 20168948]
- Campbell K, Fainman Y, & Groisman A (2007). Applied Physics Letters, 91, 171111.
- Caulfield HJ (2002). Optics Laser Technology, 34, 1.
- Chan WW, & Kowal ST (1997). Applied Optics, 36, 8958. [PubMed: 18264450]
- Charman WN (1993). Ophthalmic and Physiological Optics, 13, 427. [PubMed: 8278200]
- Chen J, Wang W, Fang J, & Varahramyan K (2004). Journal of Micromechanics and Microengineering, 14, 675.
- Cheng CC, & Yeh JA (2007). Optics Express, 15, 7140. [PubMed: 19547032]
- Cheng CC, Chang CA, & Yeh JA (2006). Optics Express, 14, 4101. [PubMed: 19516558]
- Cheng CC, Chang CA, Liu CH, & Yeh JA (2006). Journal of Optics A: Pure Applied Optics, 8, S365.
- Chiu CW, Lin Y-C, Chao PC-P, & Fuh AY-G (2008). Optics Express, 16, 19277. [PubMed: 19582020]
- Chronis N, Liu GL, Jeong K-H, & Lee LP (2003). Optics Express, 11, 2370. [PubMed: 19471346]
- Chung SH, Choi SW, Kim YJ, Ahn HJ, & Baik HK (2006). Japanese Journal of Applied Physics, 45, 1152.
- Dance B (1992). Laser Focus World, 28, 34.
- Davis JA, Valadéz KO, & Cottrell DM (2003). Applied Optics, 42, 2003. [PubMed: 12699347]

- Dong L, Agarwal AK, Beebe DJ, & Jiang H (2006). *Nature*, 442, 551. [PubMed: 16885981]
- Dong L, Agarwal AK, Beebe DJ, & Jiang H (2007). *Advanced Materials*, 19, 401.
- Faklis D, & Morris GM (1995). *Applied Optics*, 34, 2462. [PubMed: 21052381]
- Fan Y-H, Ren H, & Wu S-T (2003). *Optics Express*, 11, 3080. [PubMed: 19471429]
- Fan Y-H, Ren H, & Wu S-T (2005). *Optics Express*, 13, 4141. [PubMed: 19495326]
- Feng G-H, & Chou Y-C (2009). *Applied Optics*, 48, 3284. [PubMed: 19543333]
- Fernández EJ, Prieto PM, & Artal P (2009). *Optics Letters*, 34, 2628. [PubMed: 19724513]
- Ferstl M, & Frisch A-M (1996). *Journal of Modern Optics*, 43, 1451.
- Fowler CW, & Pateras ES (1990). *Ophthalmic and Physiological Optics*, 10, 186. [PubMed: 2196511]
- Futhey JA (1989). *Proceedings of SPIE*, 1052, 142.
- Goodman JW (2005). *Introduction to Fourier optics*. Roberts & Company Publishers.
- Gorman CB, Biebuyck HA, & Whitesides GM (1995). *Langmuir*, 11, 2242.
- Gural'nik IP, & Samagin SA (2003). *Quantum Electronics*, 33, 430.
- Grilli S, Miccio L, Vespi V, Finizio A, De Nicola S, & Ferraro P (2008). *Optics Express*, 16, 8084. [PubMed: 18545521]
- Gruneisen MT, DeSandre LF, Rotge JR, Dymale RC, & Lubin DL (2004). *Optical Engineering*, 43, 1387.
- Gvozdarev A, & Nevskaia GE (1999). *Molecular Crystallization Liquid Crystallization Science Technology*, Section A, 329, 81.
- Gvozdarev A, & Nevskaia GE (2001a). *Molecular Crystallization Liquid Crystallization Science Technology*, Section A, 4, 364.
- Gvozdarev A, & Nevskaia GE (2001b). *Molecular Crystallization Liquid Crystallization Science Technology*, Section B: Nonlinear Optics, 4, 358.
- Hain M, Glöckner R, Bhattacharya S, Dias D, Stankovic S, & Tschudi T (2001). *Optics Communications*, 188, 291.
- Hands PJW, Tatarkova SA, Kirby AK, & Love GD (2006). *Optics Express*, 14, 4525. [PubMed: 19516606]
- Haus HA, & Melcher JR (1998). Electromagnetic fields and energy (chap. 11). http://web.mit.edu/6.013_book/www/chapter11/11.9.html.
- He Z, Nose T, & Sato S (1995). *Japanese Journal of Applied Physics*, 34, 2392.
- Honma M, Nose T, & Sato S (1999). *Japanese Journal of Applied Physics*, 38, 89.
- Humphrey WE (1976). *Optical Engineering*, 15, 286.
- Jaroszewicz Z, Kołodziejczyk A, Mira A, Henao R, & Bará S (2005). *Optics Express*, 13, 918. [PubMed: 19494954]
- Jeong KH, Liu GL, Chronis N, & Lee LP (2004). *Optics Express*, 12, 2494. [PubMed: 19475086]
- Jepsen ML, & Gerritsen HJ (1996). *Optics Letters*, 21, 1081. [PubMed: 19876259]
- Jones TB, Gunji M, Washizu M, & Feldman MJ (2001). *Journal of Applied Physics*, 89, 1441.
- Kawamura M, Ye M, & Sato S (2005). *Japanese Journal of Applied Physics*, 44, 6098.
- Kim D-W, Yu C-J, Kim H-R, Kim S-J, & Lee S-D (2006). *Applied Physics Letters*, 88, 203505.
- Klaus W, Ide M, Hayano Y, Morokawa S, & Arimoto Y (1999). *Proceedings of SPIE*, 3635, 66.
- Knollman GC, Bellin JLS, & Weaver JL (1970). *Journal of the Acoustical Society of America*, 49, 253.
- Kolodziejczyk A, & Jaroszewicz Z (1993). *Applied Optics*, 32, 4317. [PubMed: 20830087]
- Kowal ST, Cleverly DS, & Kornreich PG (1984). *Applied Optics*, 23, 278. [PubMed: 18204554]
- Kress B, & Mey P (2000). *Digital diffractive optics*. England: John Wiley & Sons Ltd.
- Krupenkin T, Yang S, & Mach P (2003). *Applied Physics Letters*, 82, 316.
- Kuiper S, & Hendriks BHW (2004). *Applied Physics Letters*, 85, 1128.
- Kuwano R, Tokunaga T, Otani Y, & Umeda N (2005). *Optical Review*, 12, 405.
- Laude V (1998). *Optics Communications*, 153, 134.
- Lee DW, & Cho Y-H (2010). *Journal of Micromechanics and Microengineering*, 20, 035029.

- Lee SW, & Lee SS (2007). Applied Physics Letters, 90, 121129.
- Lester GA, Coulston SJ, & Strudwick AM (2006). Applied Optics, 45, 110. [PubMed: 16422328]
- Li G (2008). Liquid crystal lenses for correction of presbyopia. In Dainty JC (Ed.), Adaptive optics for industry and medicine: Proceedings of the Sixth International Workshop (pp. 3–8). London: Imperial College Press.
- Li G, Ayras P, & Peyghambarian N (2006) U.S. Patent No. 0164593.
- Li G, & Fang H (2010). Frontiers in optics. Rochester, New York: Optical Society of America.
- Li G, Fang X, & Zhao D (2010). Frontiers in optics. Rochester, New York: Optical Society of America.
- Li G, Mathine DL, Valley P, Ayras P, Haddock JN, Giridhar MS, et al. (2006). Proceedings of the National Academy of Sciences of the United States of America, 103, 6100. [PubMed: 16597675]
- Li G, Valley P, Äyräs P, Honkanen S, & Peyghambarian N (2007). Applied Physics Letters, 90, 111105.
- Li G, Valley P, Giridhar MS, Mathine D, Meredith G, Haddock J, et al. (2006). Applied Physics Letters, 89, 141120.
- Lin L-C, Jau H-C, Lin T-H, & Fuh AY-G (2007). Optics Express, 15, 2900. [PubMed: 19532525]
- Liu C-X, Park J, & Choi J-W (2008). Journal of Micromechanics and Microengineering, 18, 035023.
- Lohmann AW (1964). British Patent, 998, 191.
- Lohmann AW (1970). Applied Optics, 9, 1669. [PubMed: 20076440]
- Lohmann AW, & Paris DP (1967). Applied Optics, 6, 1567. [PubMed: 20062261]
- Loktev MY, Belopukhov VN, Vladimirov FL, Vdovin GV, Love GD, & Naumov AF (2000). Review of Scientific Instruments, 71, 3290.
- López CA, & Hirsa AH (2008). Nature Photonics, 2, 610.
- López CA, Lee CC, & Hirsa AH (2005). Applied Physics Letters, 87, 134102.
- Love GD, Hoffman DM, Hands PJW, Gao J, Kirby AK, & Banks MS (2009). Optics Express, 17, 15716. [PubMed: 19724571]
- Marks R, Mathine DL, Peyman G, Schwiegerling J, & Peyghambarian N (2009). Optics Letters, 34, 515. [PubMed: 19373359]
- Masuda S, Takahashi S, Nose T, Sato S, & Ito H (1997). Applied Optics, 36, 4772. [PubMed: 18259277]
- McManamon PF, Dorschner TA, Corkum DL, Friedman LJ, Holz M, Liberman S, et al. (1996). Proceedings of IEEE, 84, 268.
- McOwan PW, Gordon MS, & Hossack WJ (1993). Optics Communications, 103, 189.
- Miccio L, Finizio A, Grilli S, Vespi V, Paturzo M, De Nicola S, et al. (2009). Optics Express, 17(4), 2487. [PubMed: 19219152]
- Miccio L, Paturzo M, Grilli S, Vespi V, & Ferraro P (2009). Optics Letters, 34, 1075. [PubMed: 19340224]
- Minnema L, Barneveld HA, & Rinkel PD (1980). IEEE Transactions on Electrical Insulation, EI-15(6), 461.
- Moran PM, Dharmatilleke S, Khaw AH, Tan KW, Chan ML, & Rodriguez I (2006). Applied Physics Letters, 88, 041120.
- Naumov AF, Loktev MY, Guralnik IR, & Vdovin G (1998). Optics Letters, 23, 992. [PubMed: 18087406]
- Naumov AF, Love GD, Yu ML, & Vladimirov FL (1999). Optics Express, 4, 344. [PubMed: 19396291]
- Nose T, Masuda S, & Sato S (1991a). Molecular Crystallization Liquid Crystallization, 199, 27.
- Nose T, Masuda S, & Sato S (1991b). Japanese Journal of Applied Physics, 30, 2110.
- Nose T, Masuda S, & Sato S (1992). Japanese Journal of Applied Physics, 31, 1643.
- Nose T, & Sato S (1989). Liquid Crystallization, 5, 1425.
- Nouhi A, & Kowal ST (1984). Applied Optics, 23, 2774. [PubMed: 18213074]
- Ohtaki S, Murao N, Ogasawara M, & Iwasaki M (1999). Japanese Journal of Applied Physics, 38, 1744.

- Oku H, Hashimoto K, & Ishikawa M (2004). Optics Express, 12, 2138. [PubMed: 19475049]
- Pang L, Levy U, Campbell K, Groisman A, & Fainman Y (2005). Optics Express, 13, 9003. [PubMed: 19498935]
- Patel JS, & Rastani K (1991). Optics Letters, 16, 532. [PubMed: 19773990]
- Peng R, Chen J, Zhu C, & Zhuang S (2007). Optics Express, 15, 6664. [PubMed: 19546976]
- Presnyakov VV, Asatryan KE, Galstian TV, & Tork A (2002). Optics Express, 10, 865. [PubMed: 19451939]
- Presnyakov VV, & Galstian TV (2005). Journal of Applied Physics, 97, 103101.
- Qiao W, Tsai FS, Cho SH, Yan H, & Lo Y-H (2009). IEEE Photonics Technology Letters, 21, 304.
- Rawicz AH, & Mikhailenko I (1996). Applied Optics, 35, 1587. [PubMed: 21085276]
- Rege SS, Tkaczyk TS, & Descour MR (2004). Optics Express, 12, 2574. [PubMed: 19475097]
- Reichelt S, & Zappe H (2007). Optics Express, 15, 14146. [PubMed: 19550687]
- Ren H, & Wu S-T (2002). Applied Physics Letters, 81, 3537.
- Ren H, & Wu ST (2003). Applied Physics Letters, 82, 22.
- Ren H, & Wu ST (2005). Applied Physics Letters, 86, 211107.
- Ren H, & Wu ST (2006). Optics Express, 14, 11292. [PubMed: 19529544]
- Ren H, & Wu ST (2008). Optics Express, 16, 2646. [PubMed: 18542348]
- Ren H, Fan Y-H, Gauza S, & Wu ST (2004a). Japanese Journal of Applied Physics, 43, 652.
- Ren H, Fan Y-H, Gauza S, & Wu S-T (2004b). Applied Physics Letters, 84, 4789.
- Ren H, Fan Y-H, & Wu S-T (2003). Applied Physics Letters, 83, 1515.
- Ren H, Fox D, Anderson PA, Wu B, & Wu S-T (2006). Optics Express, 14, 8031. [PubMed: 19529173]
- Ren H, Fox DW, Wu B, & Wu S-T (2007). Optics Express, 15, 11328. [PubMed: 19547490]
- Ren H, Lin Y-H, & Wu S-T (2006). Applied Physics Letters, 88, 1911116.
- Ren H, Xianyu H, Xu S, & Wu ST (2008). Optics Express, 16, 14954. [PubMed: 18795032]
- Resler DP, Hobbs DS, Sharp RC, Friedman LJ, & Dorschner TA (1996). Optics Letters, 21, 689. [PubMed: 19876126]
- Reza S, & Riza NA (2009). Optics Communications, 282, 1298.
- Riza NA, & DeJule MC (1994). Optics Letters, 19, 1013. [PubMed: 19844517]
- Sato S (1979). Japanese Journal of Applied Physics, 18, 1679.
- Sato S, Sugiyama A, & Sato R (1985). Japanese Journal of Applied Physics, 24, L626.
- Sato S, & Ye M (2005). Proceedings of SPIE, 5936, 113.
- Scharf T, Kipfer P, Bouvier M, & Grupp J (2000). Japanese Journal of Applied Physics, 39, 6629.
- Scharf T, Fontannaz J, Bouvier M, & Grupp J (1999). Molecular Crystallization Liquid Crystallization, 331, 235.
- Schneider F, Draheim J, Kammerer R, Waibel P, & Wallrabe U (2009). Optics Express, 17, 11813. [PubMed: 19582096]
- Schneider F, Müller C, & Wallrabe U (2008). Journal of Optics A: Pure Applied Optics, 10, 044002.
- Shaw D, & Sun TE (2007). Optical Engineering, 46, 024002.
- Shi J, Stratton Z, Steven S-C, Huang L-H, & Huang T-J (2010). Microfluidics and Nanofluidics, 9, 313.
- Simonov AN, Vdovin G, & Loktev M (2007). Optics Express, 15, 7468. [PubMed: 19547070]
- Simonov AN, Vdovin G, & Rombach MC (2006). Optics Express, 14, 7757. [PubMed: 19529146]
- Slinger C, Brett P, Hui V, Monnington G, Pain D, & Sage I (1997). Optics Letters, 22, 1113. [PubMed: 18185768]
- Smith G, & Atchison DA (1997). The eye and visual optical instruments. United Kingdom: Cambridge University Press.
- Somalingam S, Dressbach K, Hain M, Stankovic S, Tschudi T, Knittel J, et al. (2004). Applied Optics, 43, 2722. [PubMed: 15130012]
- Spivey B (2008). U.S. Patent No. 151184.

- Stallinga S, Vrehen JJ, Wals J, Stapert H, & Verstegen E (2000). Proceedings of SPIE, 4081, 50.
- Sugiura N, & Morita S (1993). Applied Optics, 32, 4181. [PubMed: 20830064]
- Sun Y, Nordin GP, Kowal ST, & Wang B (2003). Proceedings of SPIE, 4987, 209.
- Takahashi T, Ye M, & Sato S (2007). Japanese Journal of Applied Physics, 46, 2926.
- Takaki Y, & Ohzu H (1996). Applied Optics, 35, 6896. [PubMed: 21151288]
- Tam EC (1992). Optics Letters, 17, 369. [PubMed: 19784331]
- Tolosa A, Martinez-Cuenca R, Pons A, Saavedra G, Martinez-Corral M, & Javadi B (2010). Journal of the Optical Society of America A, 27, 495.
- Vallet M, Berge B, & Volvelle L (1996). Polymer (Guildf), 37, 2465.
- Vdovin GV, Gural'nik IR, Kotova SP, Yu ML, & Naumov AF (1999a). Quantum Electronics, 29, 256.
- Vdovin GV, Gural'nik IR, Kotova SP, Yu ML, & Naumov AF (1999b). Quantum Electronics, 29, 261.
- Vdovin G, Loktev M, & Naumov A (2003). Optics Express, 11, 810. [PubMed: 19461793]
- Verheijen HJJ, & Prins NWJ (1999). Langmuir, 15, 6616.
- Wang X, Wang B, Bos PJ, Anderson JE, Pouch JJ, & Miranda FA (2005). Journal of the Optical Society of America A, 22, 346.
- Wang X, Wilson D, Muller R, Maker P, & Psaltis D (2000). Applied Optics, 39, 6545. [PubMed: 18354668]
- Wang B, Ye M, Honma M, Nose T, & Sato S (2002). Japanese Journal of Applied Physics, 41, L1232.
- Wang B, Ye M, & Sato S (2004). Applied Optics, 43, 3420. [PubMed: 15219022]
- Wang B, Ye M, & Sato S (2005a). Japanese Journal of Applied Physics, 44, 4979.
- Wang B, Ye M, & Sato S (2005b). Optics Communications, 250, 266.
- Wang B, Ye M, & Sato S (2005c). Molecular Crystallization Liquid Crystallization, 433, 217.
- Wang B, Ye M, & Sato S (2005d). Proceedings of SPIE, 6018, 324.
- Wang B, Ye M, & Sato S (2006a). IEEE Photonics Technology Letters, 18, 79.
- Wang B, Ye M, & Sato S (2006b). Japanese Journal of Applied Physics, 45, 7813.
- Wang Z, Xu Y, & Zhao Y (2007). Optics Communications, 275, 22.
- Welters WJJ, & Fokkink LGJ (1998). Langmuir, 14, 1535.
- Werber A, & Zappe H (2005). Applied Optics, 44, 3238. [PubMed: 15943257]
- Wick DV, & Martinez T (2004). Optical Engineering, 43, 8.
- Williams G, Powell NJ, & Purvis A (1989). Proceedings of SPIE, 1168, 352.
- Wiltshire MCK (1993). GEC Journal of Research 10, 119.
- Wright BM (1968). UK Patent No. 1,209,234.
- Xu S, Lin YJ, & Wu ST (2009). Optics Express, 17, 10499. [PubMed: 19550445]
- Xu S, Ren H, Lin Y-J, Moharam MGJ, Wu S-T, & Tabiryan N (2009). Optics Express, 17, 17590. [PubMed: 19907543]
- Yanase S, Ouchi K, & Sato S (2002). Japanese Journal of Applied Physics, 41, L1482.
- Yang H, Han Y-H, Zhao X-W, Nagai K, & Gu Z-Z (2006). Applied Physics Letters, 89, 111121.
- Yang Q, Kobrin P, Seabury C, Narayanaswamy S, & Christian W (2008). Applied Optics, 47, 3658. [PubMed: 18617983]
- Yang D-K, & Wu S-T (2006). Fundamentals of liquid crystal devices. England: John Wiley & Sons.
- Ye M, Noguchi M, Wang B, & Sato S (2009). Electronics Letters, 46, 646.
- Ye M, & Sato S (2002). Japanese Journal of Applied Physics, 41, L571.
- Ye M, & Sato S (2003). Japanese Journal of Applied Physics, 42, 6439.
- Ye M, & Sato S (2005). Molecular Crystallization Liquid Crystallization, 433, 229.
- Ye M, Wang B, & Sato S (2003). Japanese Journal of Applied Physics, 42, 5086.
- Ye M, Wang B, & Sato S (2004a). Japanese Journal of Applied Physics, 43, L352.
- Ye M, Wang B, & Sato S (2004b). Applied Optics, 43, 6407. [PubMed: 15617277]
- Ye M, Wang B, & Sato S (2006). IEEE Photonics Technology Letters, 18, 505.
- Ye M, Wang B, & Sato S (2008). Optics Express, 16, 4302. [PubMed: 18542526]

- Ye M, Yokoyama Y, & Sato S (2005). Japanese Journal of Applied Physics, 44, 235.
- Ye M, Yokoyama Y, & Sato S (2006). Applied Physics Letters, 89, 141112.
- Yu ML, Belopukhov VN, Vladimirov FL, Vdovin GV, Love GD, & Naumov AF (2000). The Review of Scientific Instruments, 71, 3290.
- Yu Y, Nakano M, & Ikeda T (2003). Nature 425, 145. [PubMed: 12968169]
- Zeng X, & Jiang H (2008). Applied Physics Letters, 93, 151101.
- Zhang DY, Justis N, Lien V, Berdichevsky Y, & Lo Y-H (2004). Applied Optics, 43, 783. [PubMed: 14960070]
- Zhang DY, Justis N, & Lo YH (2005). Optics Communications, 249, 175.
- Zhang DY, Lien V, Berdichevsky Y, Choi J, & Lo YH (2003). Applied Physics Letters, 82, 3171.
- Zhang X, Loktev M, & Vdovin G (2005). Review of Scientific Instruments, 76, 043109.

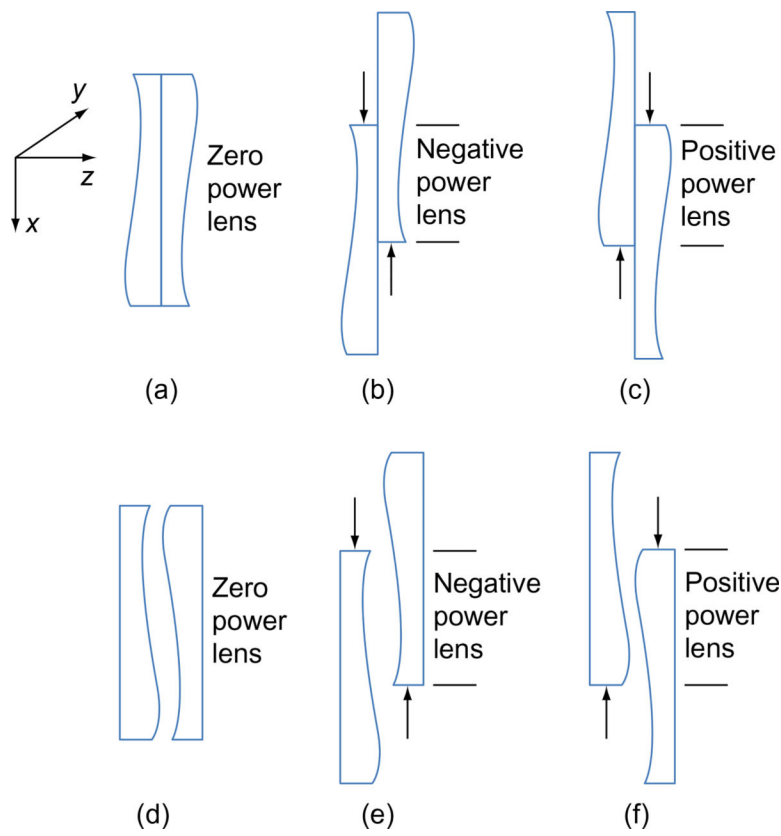


FIGURE 1.

Alvarez–Lohmann lenses. Top, outer cubic surfaces configuration at: (a) neutral position. (b) Negative power addition. (c) Positive power addition. Bottom, inner cubic surfaces configuration at: (d) neutral position. (e) Negative power addition. (f) Positive power addition. Note that for the outer cubic surfaces configuration, there must be a space between both lenses to avoid collision when the shift is done to achieve positive power addition (f).

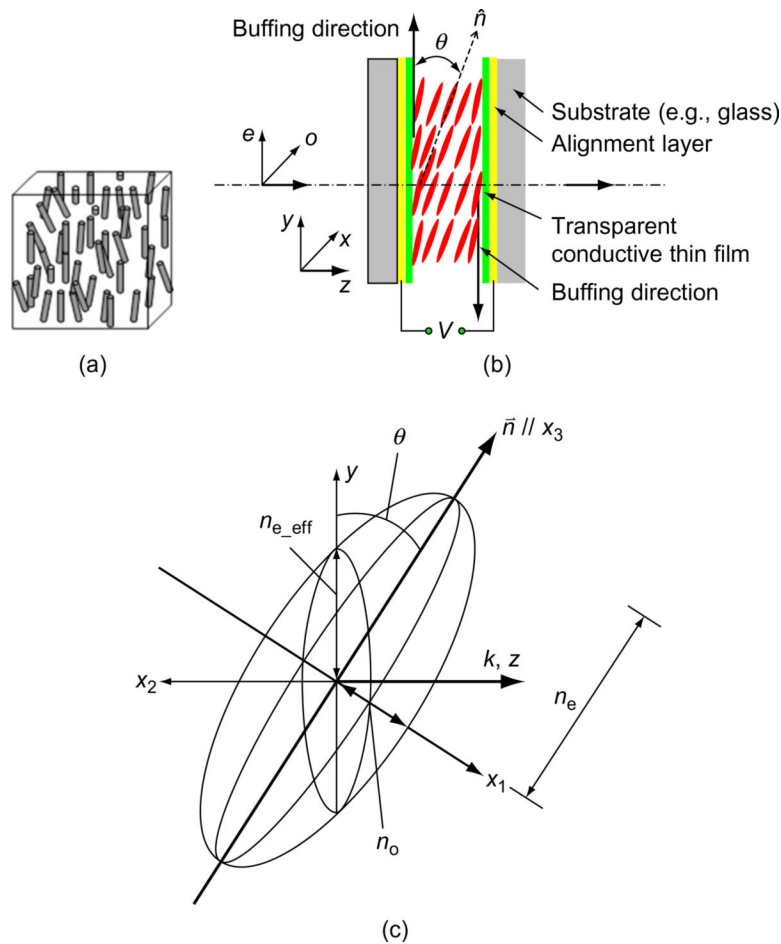


FIGURE 2.

(a) Nematic phase of rod-like LC molecules. (b) Homogeneously aligned nematic LC cell.
(c) Uniaxial LC molecule ellipsoid of refractive index.

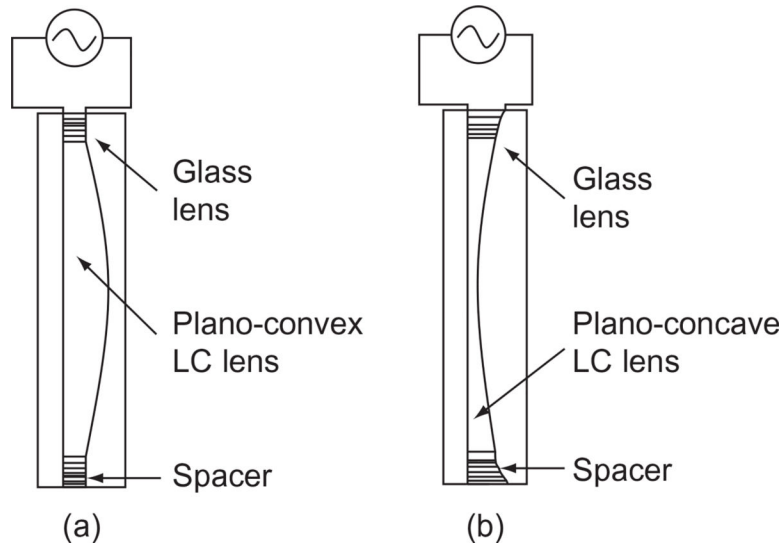


FIGURE 3.

Lens-shaped LC cell. (a) Plano-convex LC lens. (b) Plano-concave LC lens (Sato, 1979).

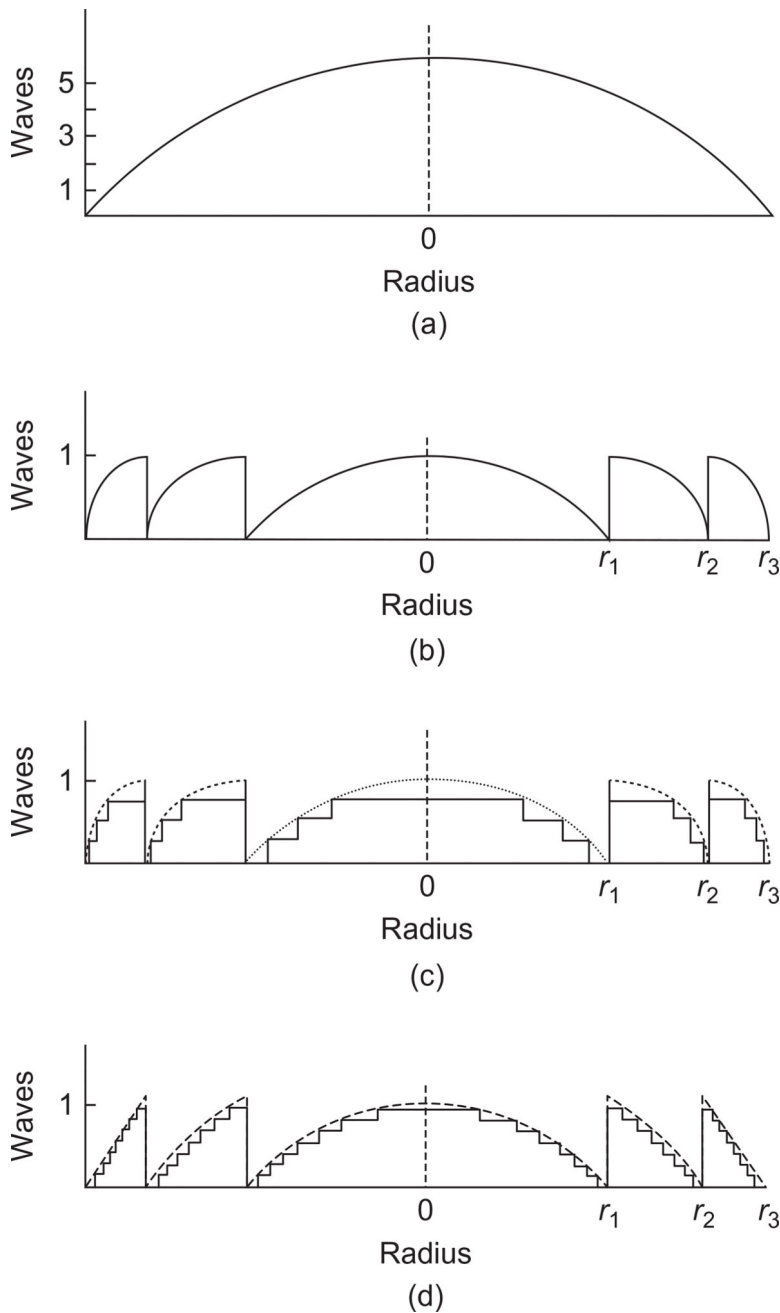
**FIGURE 4.**

Illustration of a diffractive lens: (a) conventional refractive lens. (b) Diffractive lens with continuous quadratic blaze profile. (c) Binary diffractive lens. (d) Fourth-level approximation of the diffractive lens.

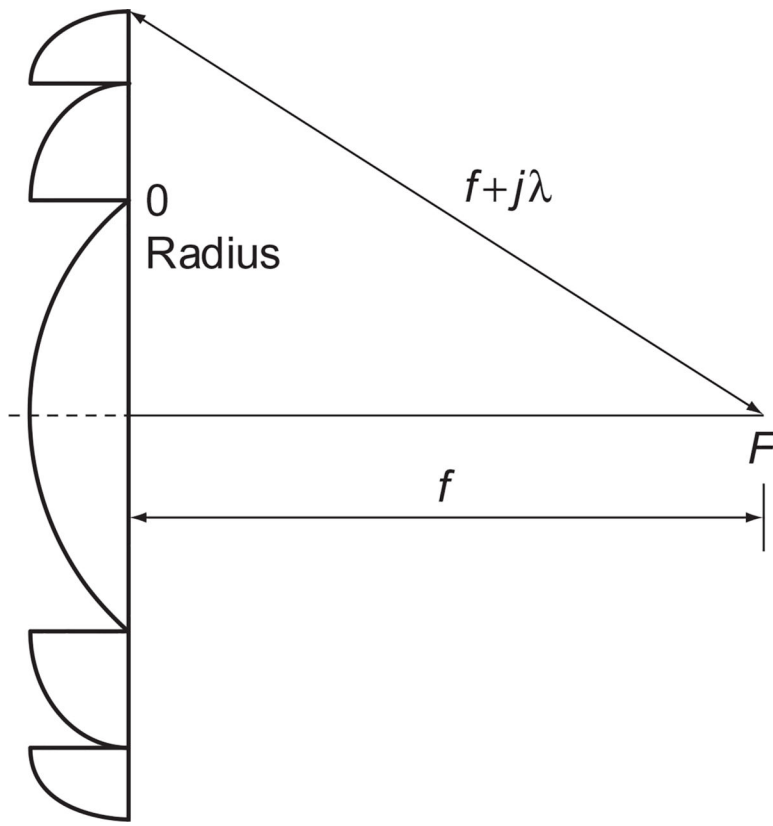
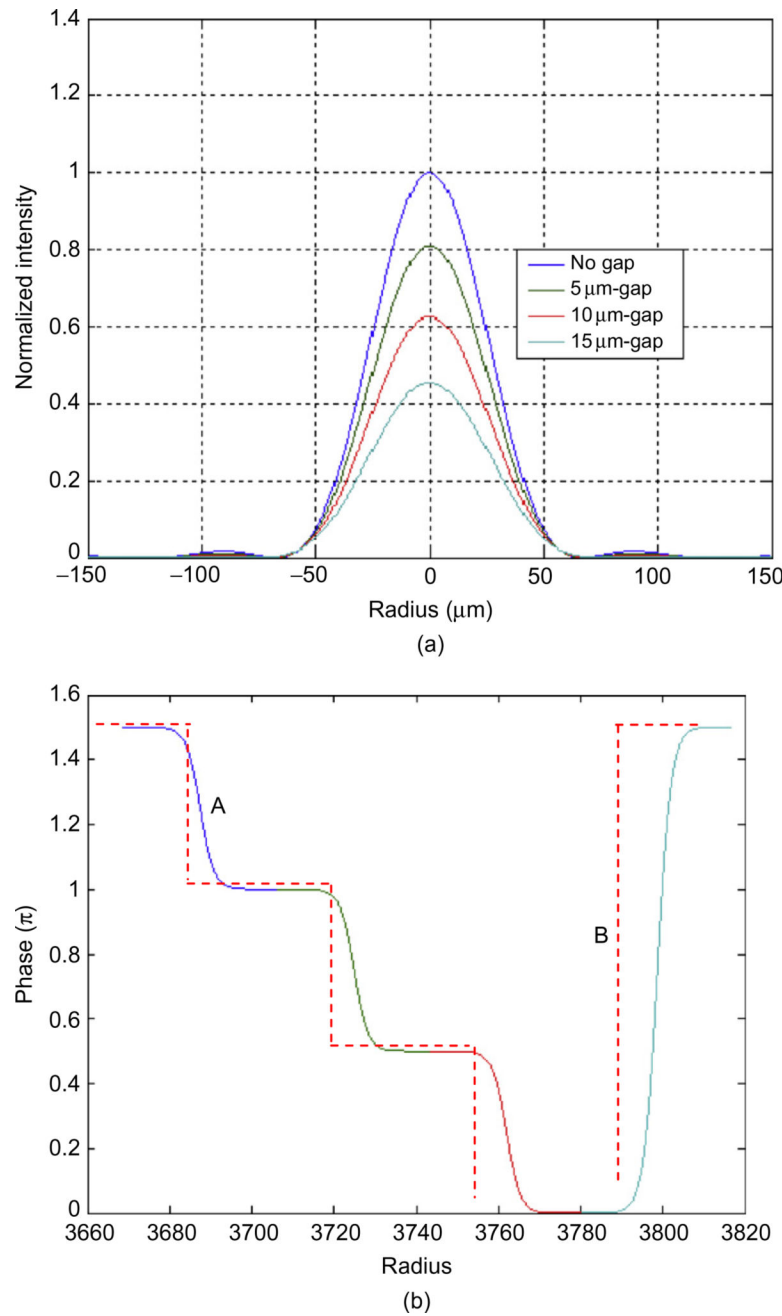


FIGURE 5.

Construction of a diffractive lens.

**FIGURE 6.**

Effects of the gaps between the neighboring ring electrodes and the fringing field. (a) Intensity distribution at the focal plane for no gap and gaps of various values. (b) Illustration of the phase profile caused by the fringing field. Dashed line is the ideal phase profile.

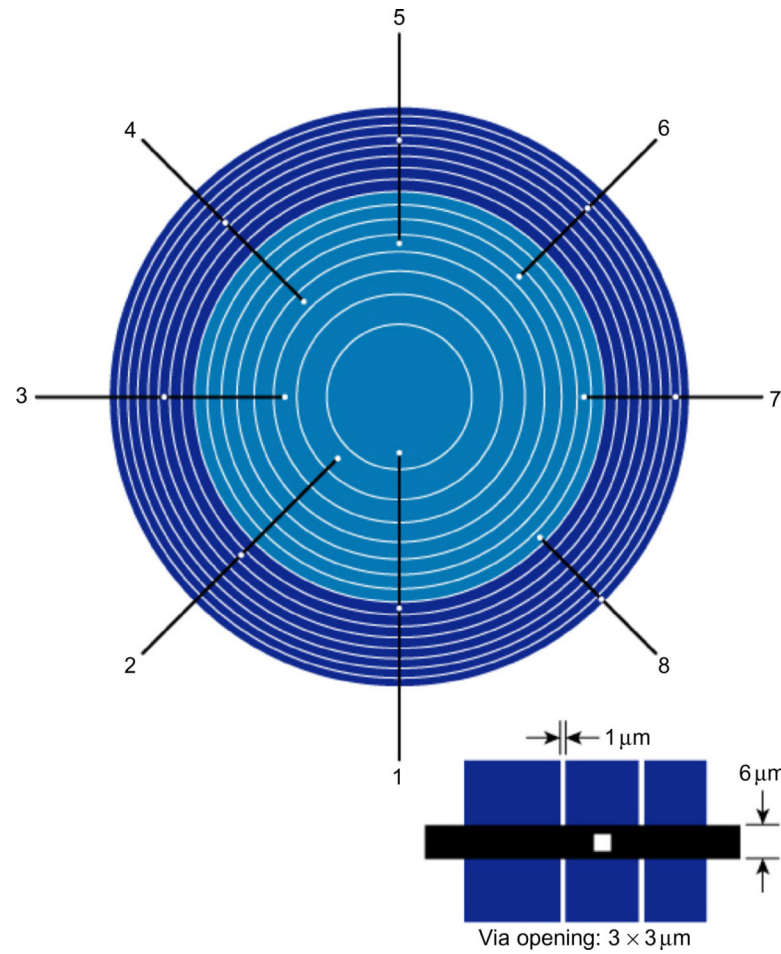


FIGURE 7.

Layout of the one-layer electrode pattern (two central zones shown) for adaptive LC diffractive lens adjacent zones are distinguished by color. An electrical insulation layer with vias is added (vias shown with white dots). Each bus connects to one electrode (subzone) in each zone. Dimensions of the vias, the bus line, and the gap between electrodes are illustrated in the bottom right corner of the figure.

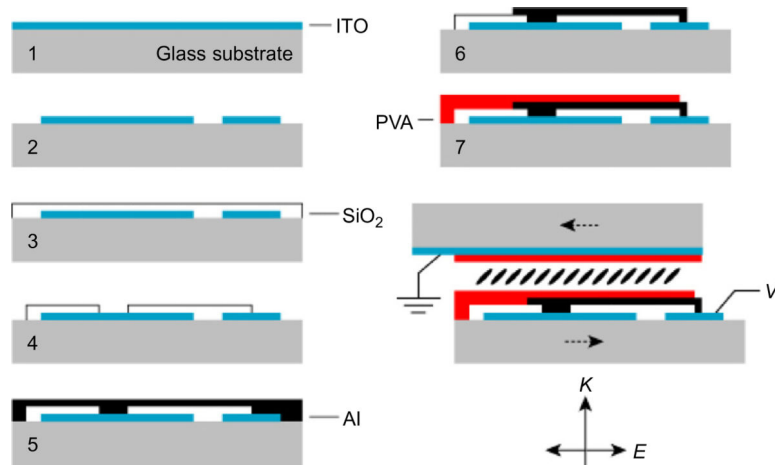


FIGURE 8.

Processing steps for fabrication of the patterned electrodes and the conductive lines. The structure of the liquid crystal lens is shown in the bottom right of the figure, where k is the wave vector and E is the polarization state of the incident light.

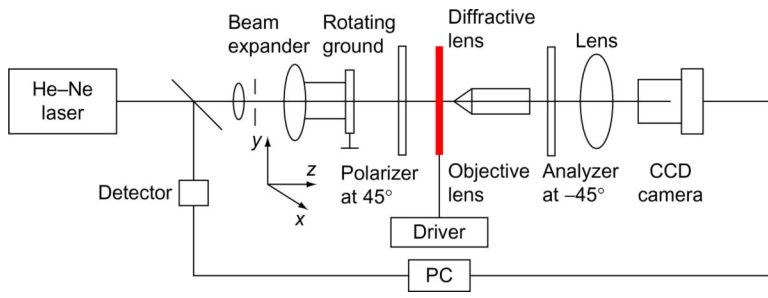


FIGURE 9.

Schematic diagram of the polarizing microscope.

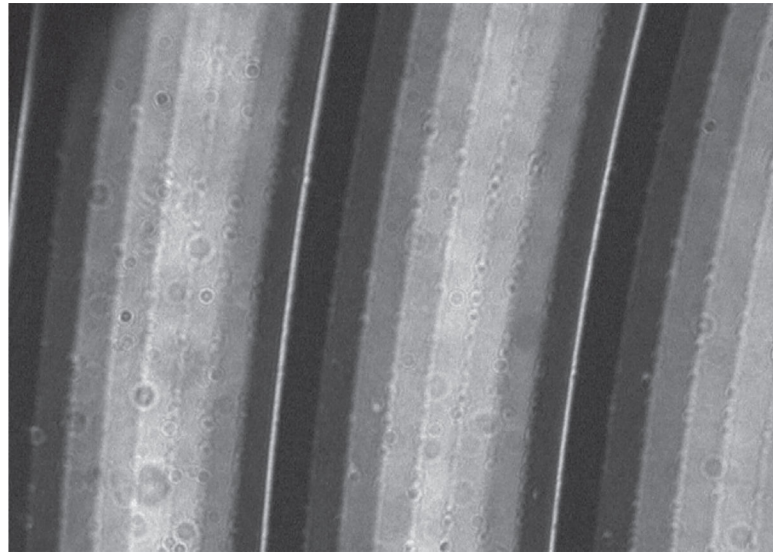


FIGURE 10.

Electro-optic response of the eighth-phase level lens obtained with polarizing microscope.

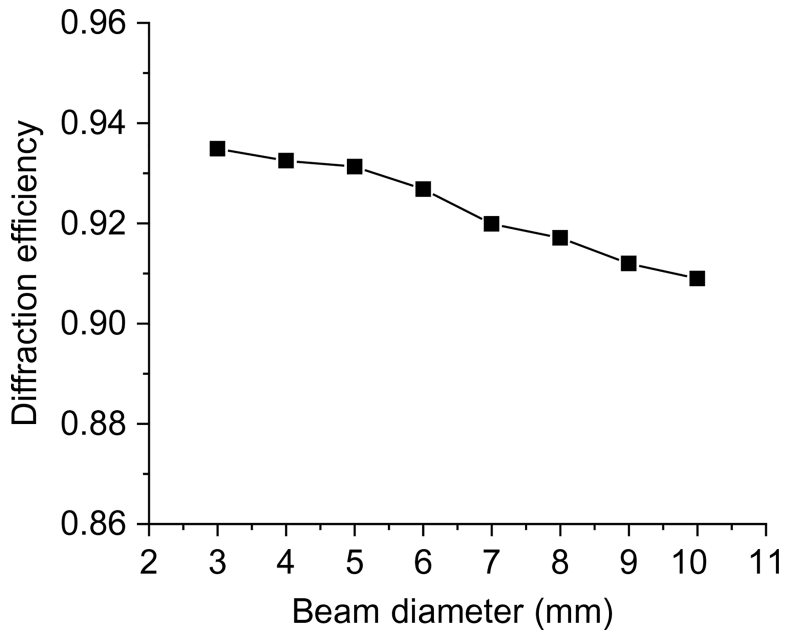


FIGURE 11.

Diffraction efficiency as a function of the beam diameter.

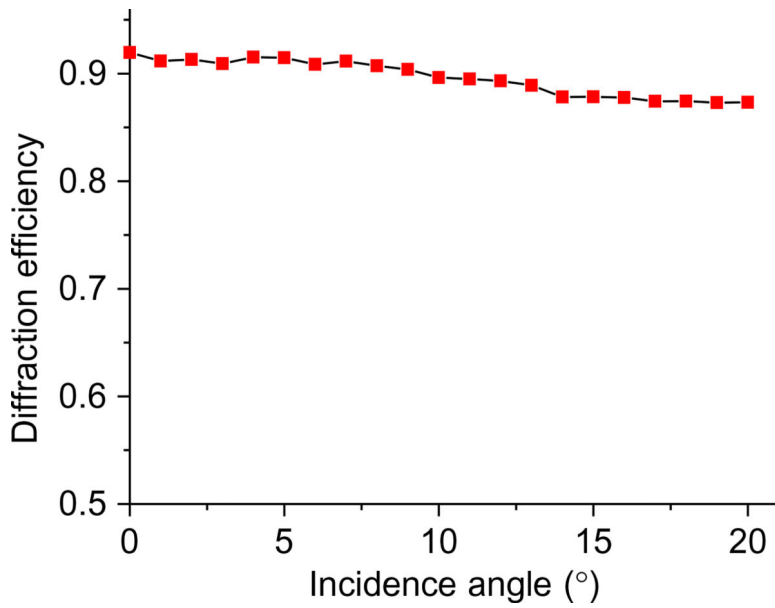


FIGURE 12.

Diffraction efficiency as a function of the incidence angle.

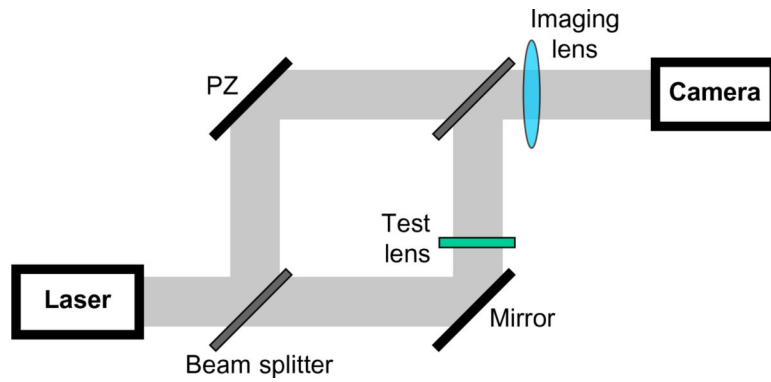


FIGURE 13.

Schematic drawing of the Mach–Zehnder interferometer for measurement of the wavefront coming out of the lens.

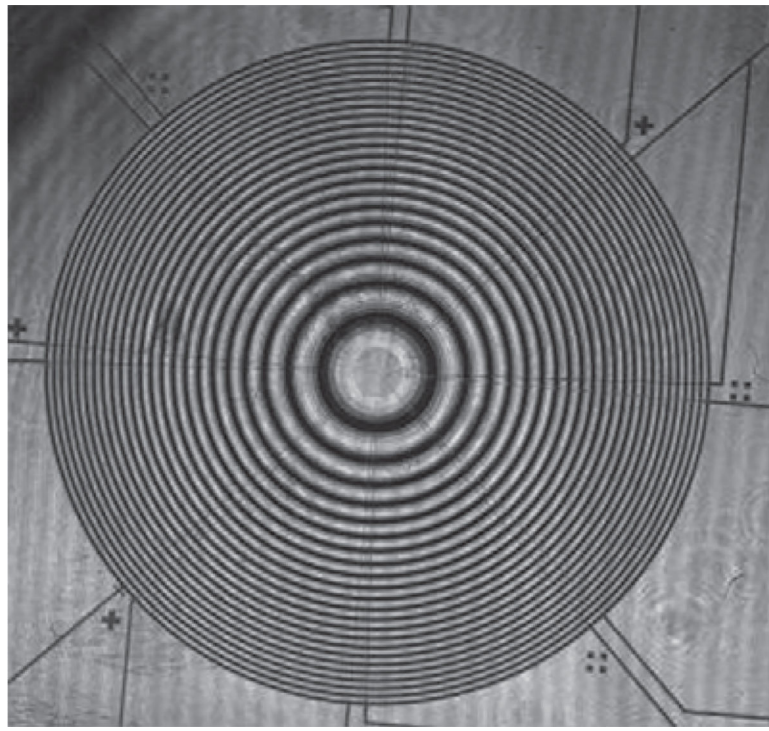
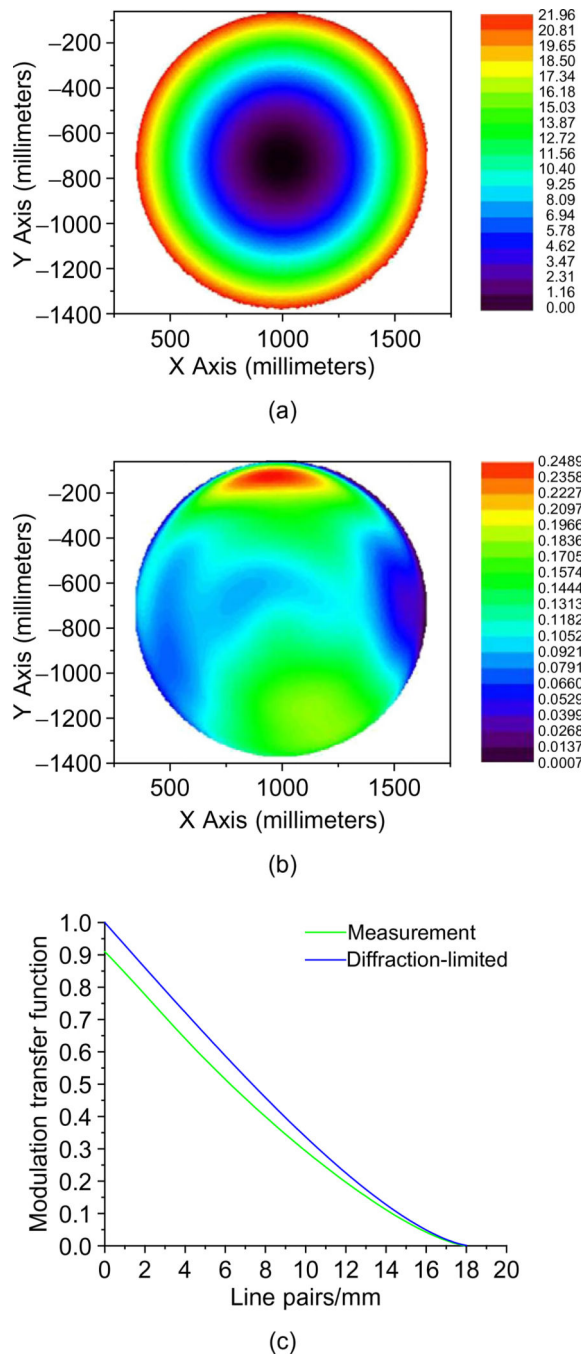


FIGURE 14.

Interferogram obtained with the Mach–Zehnder interferometer. The interference pattern has very good fringe modulation across the lens. A close-up of the interferogram shows that the eight subzones in each zone have different grayscale intensities and the pattern is periodic.

**FIGURE 15.**

Phase map of the lens working at 1-diopter. (a) Unwrapped phase map for a 10-mm aperture. (b) Phase map of the unwrapped phase minus tilting and focusing. (c) Modulation transfer function of the lens. The green line is obtained from the measurement data, while the blue line is for a diffraction-limited lens. The value at low spatial frequency is determined by the diffraction efficiency of the lens.

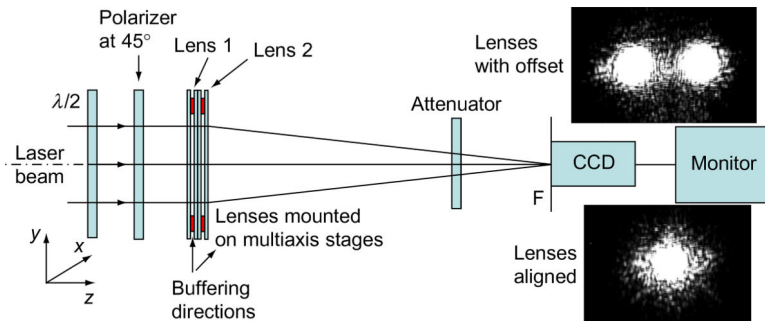


FIGURE 16.

Setup for assembly of a complete lens.

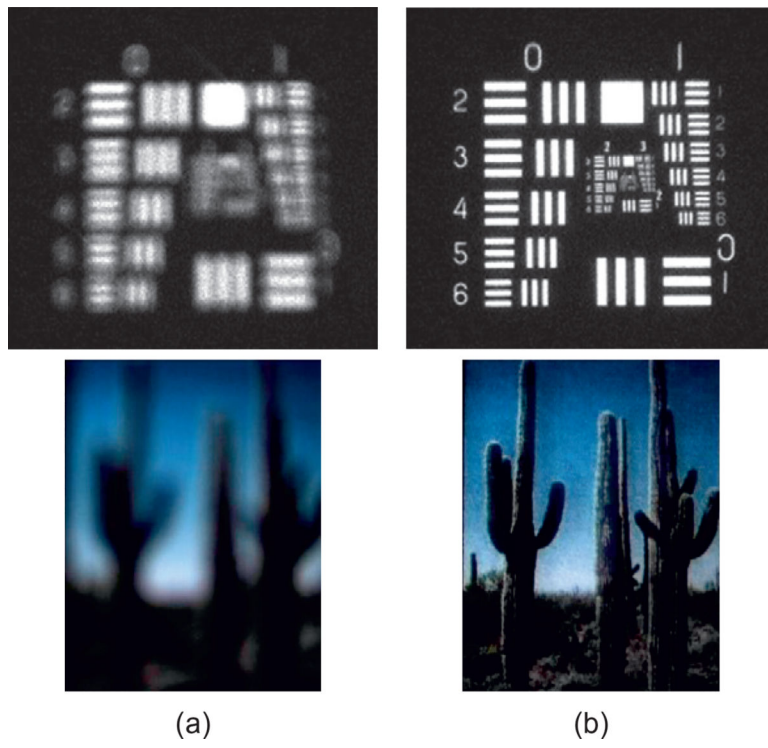
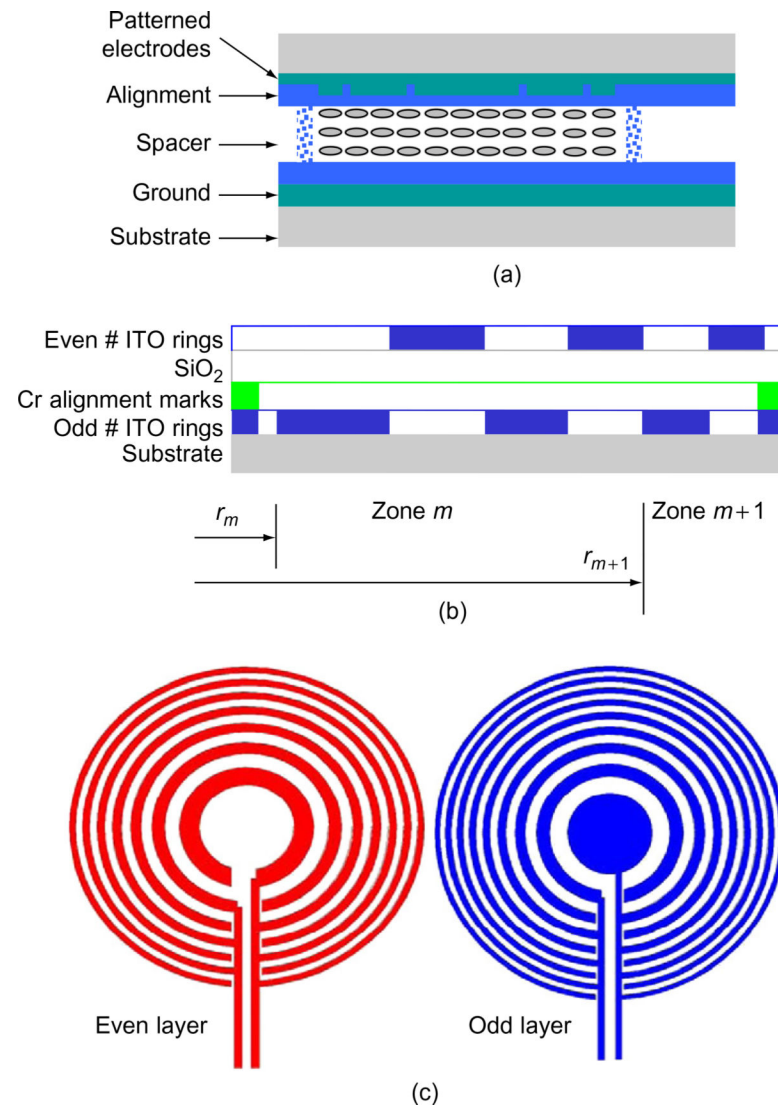


FIGURE 17.

Hybrid imaging using the 1-diopter electro-active diffractive lens with the model eye. The function of the diffractive lens is to provide near vision correction to the model eye. (a) The object is placed at a reading distance (~30 cm). The image is severely out of focus in the model eye when the diffractive lens is OFF. (b) When the diffractive lens is activated, the object is imaged clearly.

**FIGURE 18.**

Switchable LC diffractive lens. (a) Structure of the flat LC lens. (b) Structure of the two-layer electrode pattern for fourth-level lens. (c) Patterns for odd-number electrodes and even-numbered electrodes.

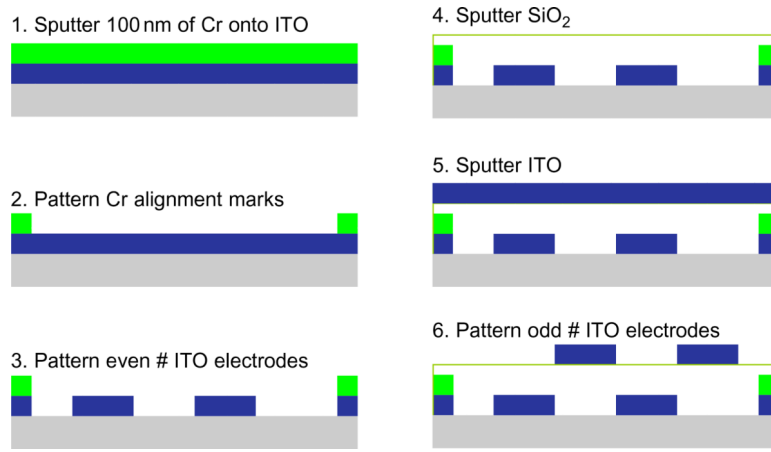
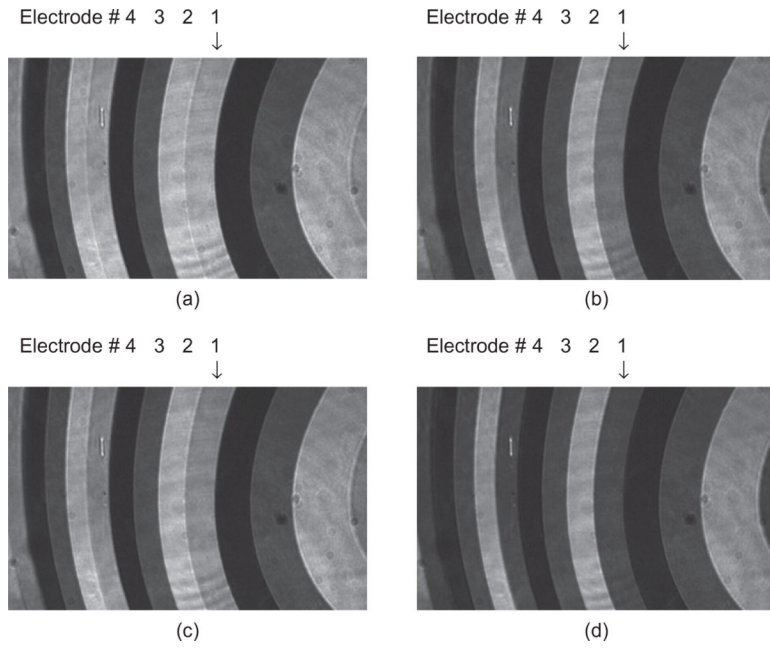
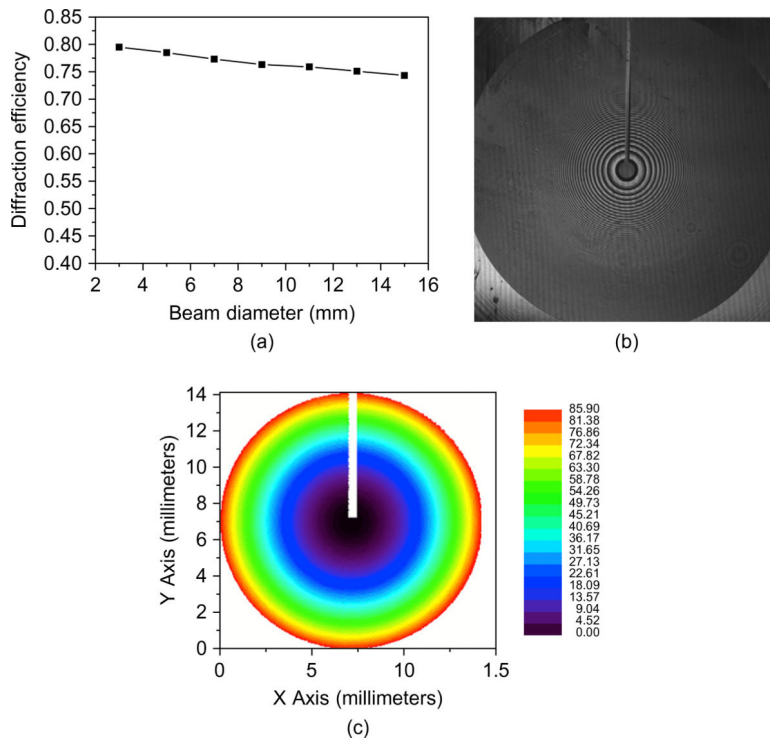


FIGURE 19.

Fabrication procedure for the interleaved electrode pattern.

**FIGURE 20.**

Operation of the electrodes. Electrodes 2, 3, 4 are set to certain voltages respectively, while the voltage applied to electrode 1 was adjusted.

**FIGURE 21.**

Some characterization results of the 15-mm-aperture, fourth-level, 2-diopter lens. (a) Diffraction efficiency as a function of the beam diameter. (b) Interferogram obtained with the Mach-Zehnder interferometer. (c) Unwrapped phase map for a 14-mm aperture.

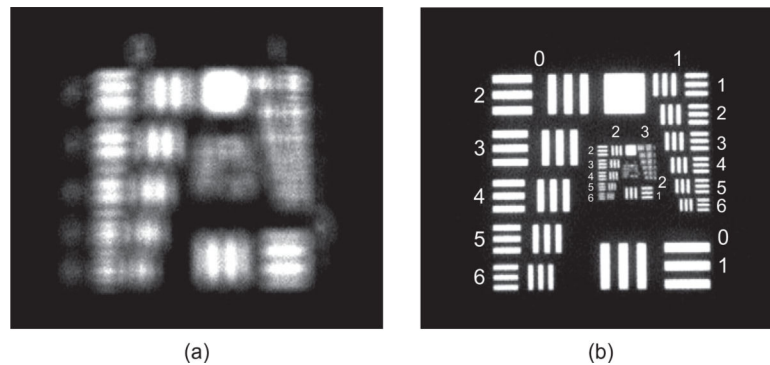


FIGURE 22.

Imaging using the 2-diopter electro-active diffractive lens with the model eye. The object is placed at a reading distance (~30cm). (a) The image is severely out of focus in the model eye when the diffractive lens is OFF. (b) When the diffractive lens is activated, the object is imaged clearly.

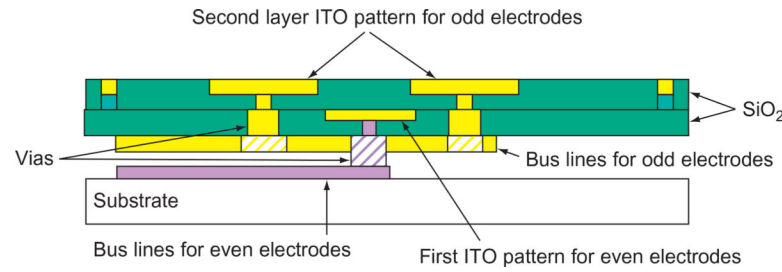
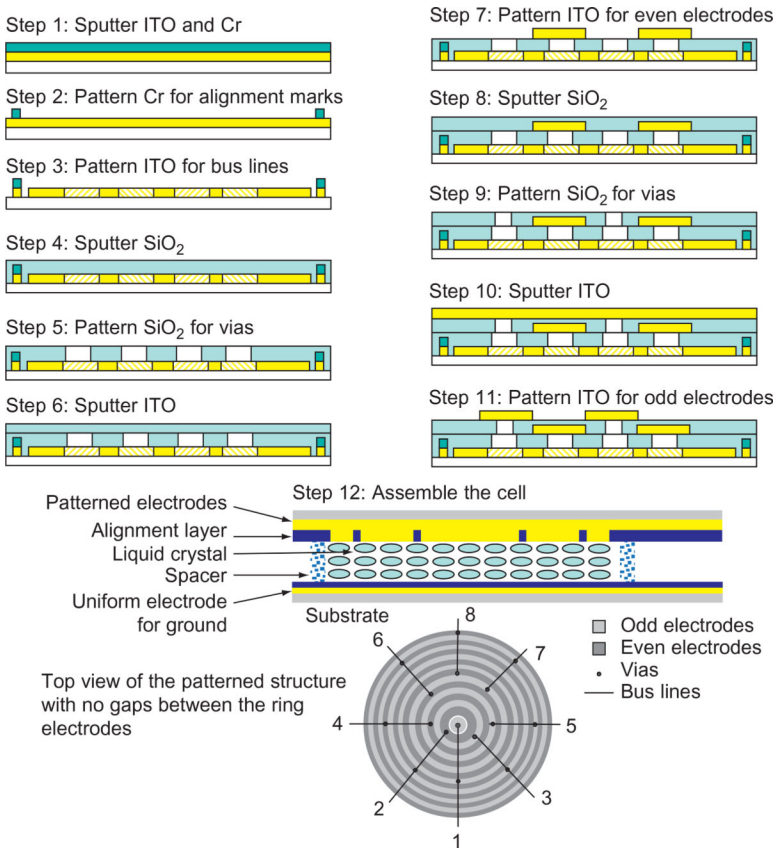
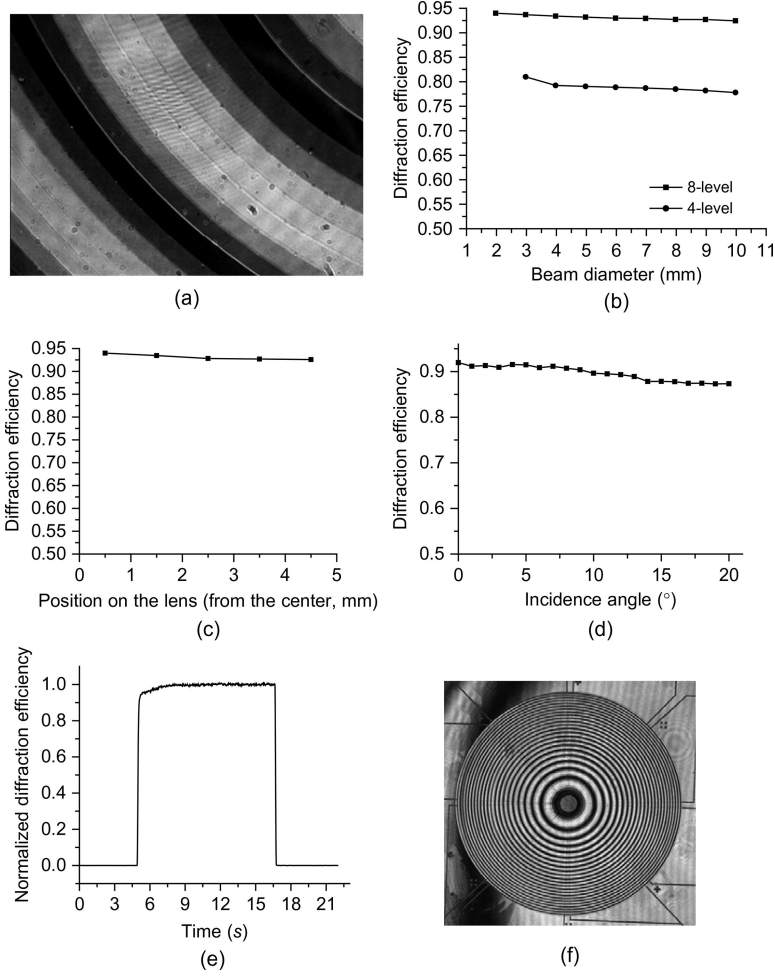


FIGURE 23.

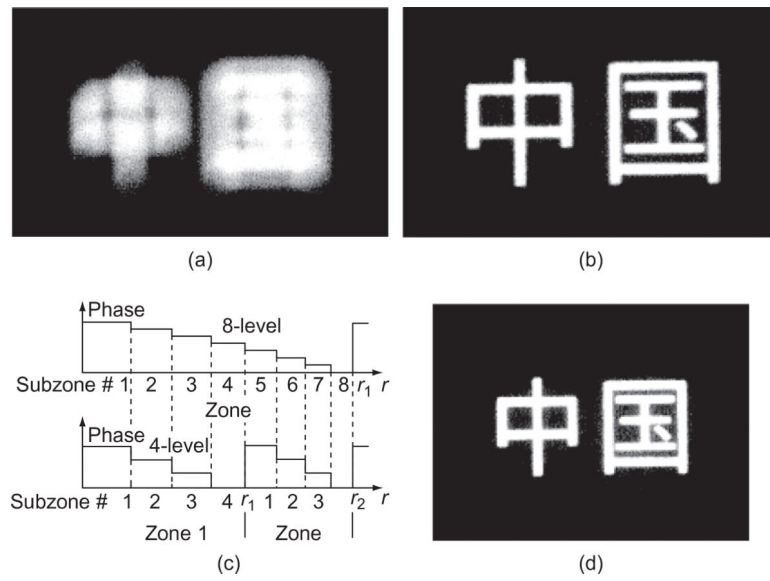
Structure of the three-layer patterned electrodes and two-layer vias. It eliminates gaps between neighboring ring electrodes for arbitrary phase levels.

**FIGURE 24.**

Processing steps for fabrication of the LC diffractive lens with three-layer patterned electrodes and two-layer via structures. At the bottom of the figure, the top view of the finished layers is shown with eight bus lines as an example. The design can be used for any higher phase levels.

**FIGURE 25.**

Characterization of the LC lens. (a) Electro-optic response of individual electrode rings. (b), (c), (d), Diffraction efficiency as a function of the beam diameter, position on the lens, and incidence angle, respectively. (e) Switching dynamics of the lens. (f) Interferogram.

**FIGURE 26.**

Hybrid imaging using the varifocal LC lens. The LC lens is (a) OFF and (b) activated with 1-diopter power. (c) An eighth-level 1-diopter LC lens can be reconfigured to a fourth-level 2-diopter lens. (d) Hybrid imaging with the 2-diopter power.

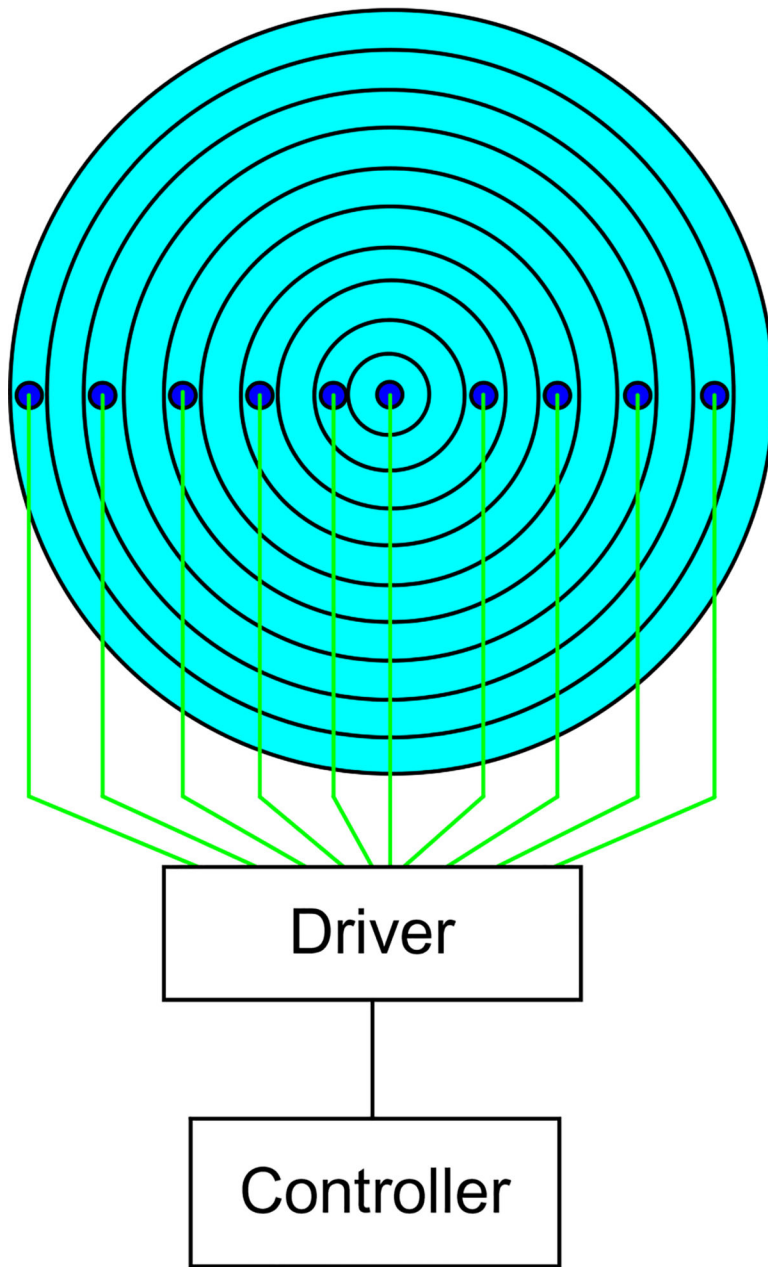


FIGURE 27.

Schematic diagram for driving the individually addressable electrodes.

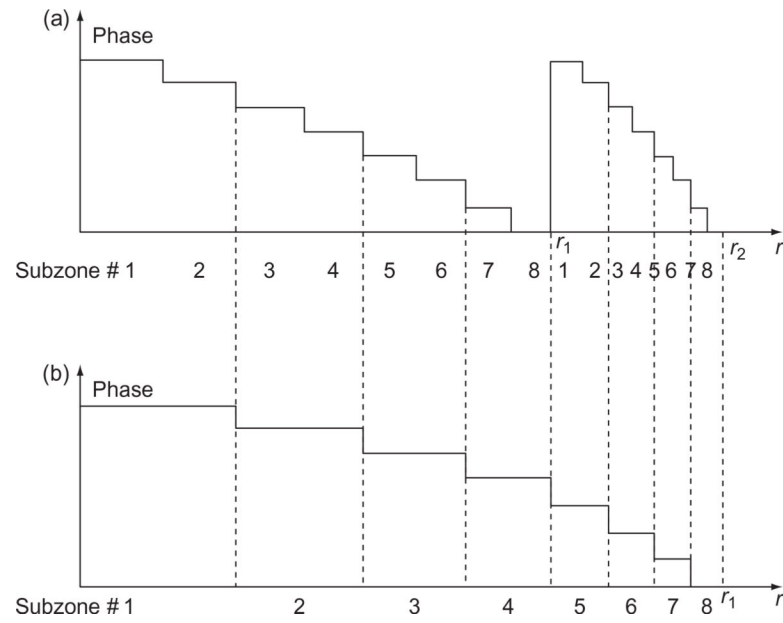


FIGURE 28.

With individually addressable electrodes, multiple focal lengths F , $2F$, $3F$, ..., can be obtained while the light efficiency is kept the same.

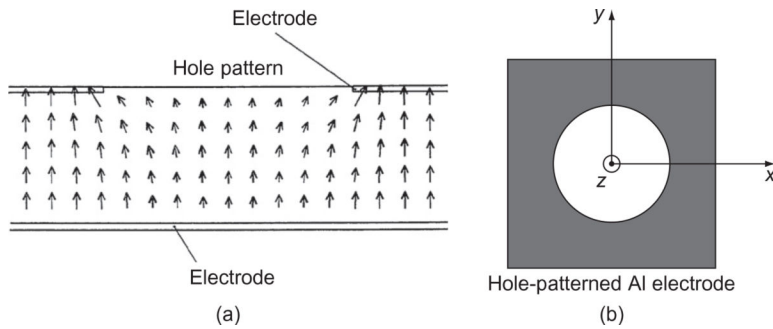


FIGURE 29.

Cross section of the nonuniform electric field produced by a hole-patterned electrode. (a) Cross section of the cell. (b) Top view of the hole pattern (Nose & Sato, 1989).

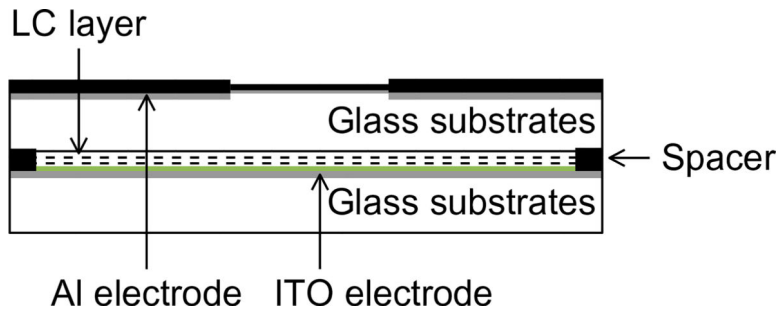


FIGURE 30.

Cell structure with the hole-patterned electrode detached from the LC layer (Ye & Sato, 2002).

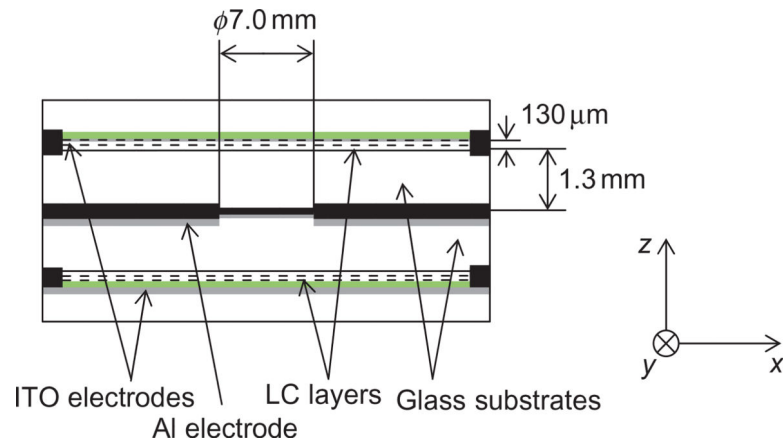


FIGURE 31.

Cell structure with the hole-patterned electrode at the center and two LC layers on its sides (Ye et al., 2004a).

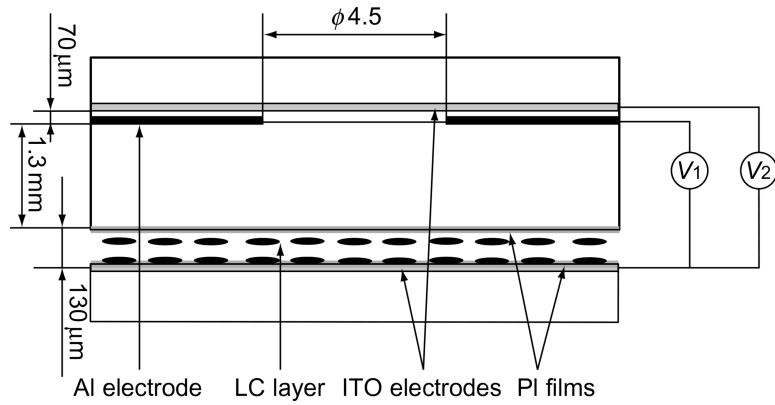
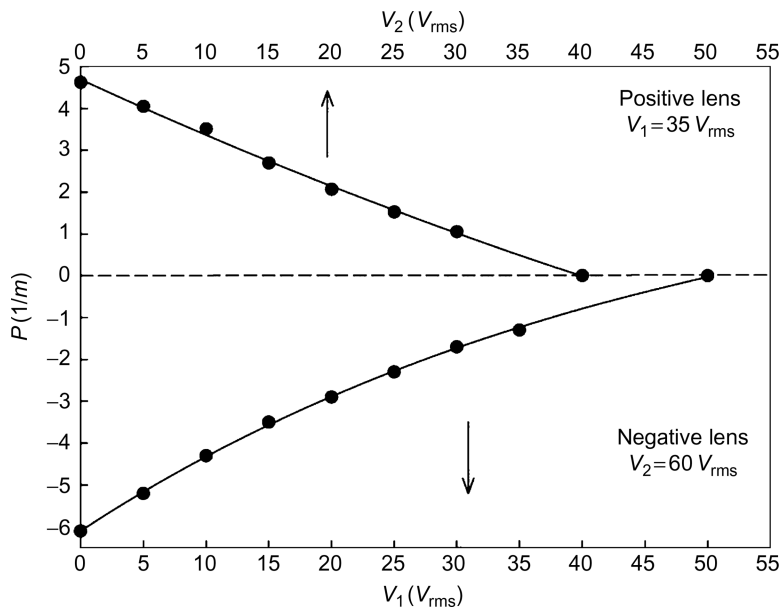


FIGURE 32.

LC cell with three electrodes driven by two voltages for wider tunable range (Ye et al., 2004b).

**FIGURE 33.**

Tunable power of the lens driven by two voltages. When V_1 is fixed at $35 V_{\text{rms}}$, positive powers are tunable as a function of V_2 ; When V_2 is fixed at $60 V_{\text{rms}}$, negative powers are tunable as a function of V_1 (Wang et al., 2006a).

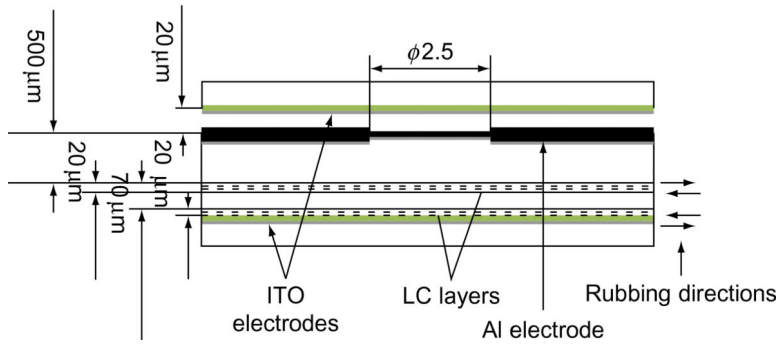


FIGURE 34.

LC cell driven by two voltages for fast operation and wider power range by stacking two thin LC layers (Wang et al., 2005b).

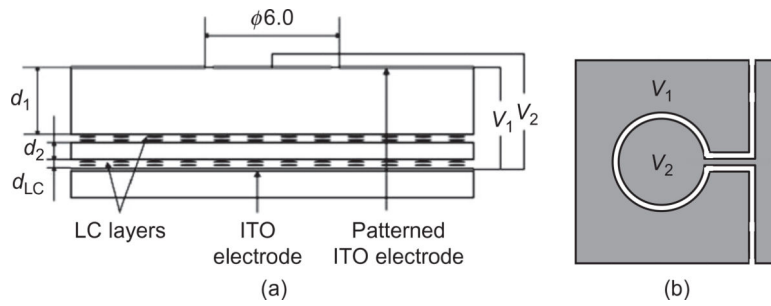


FIGURE 35.

LC lens structure driven by two voltages with a circular electrode in the center surrounded by a hole-patterned electrode. (a) Cross section. (b) Electrode pattern (Ye et al., 2008).

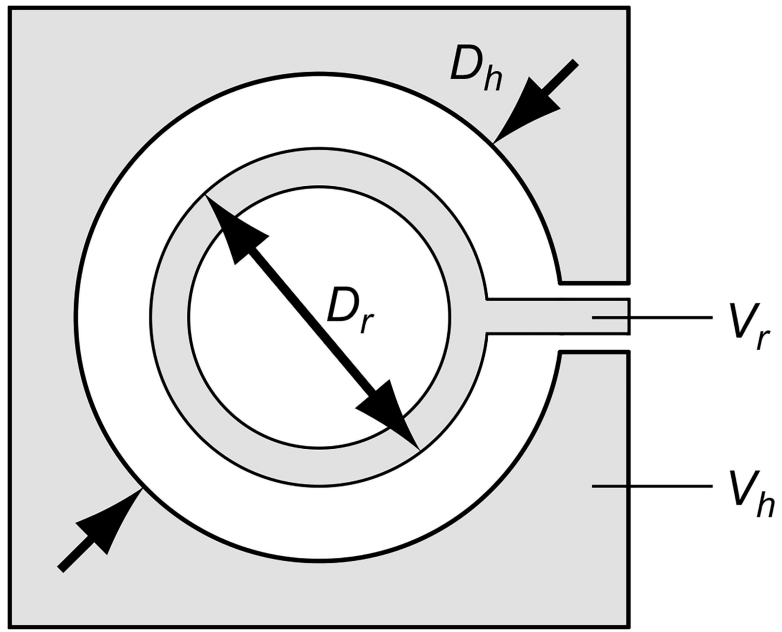


FIGURE 36.

Electrode pattern with a ring electrode inside a hole-patterned electrode. The lens structure can be the same as shown in Figure 30 (Chiu et al., 2008).

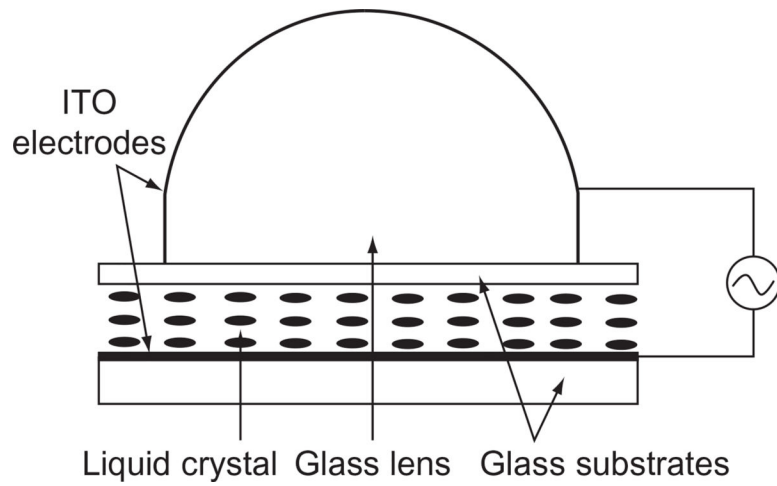


FIGURE 37.

LC cell with a spherical electrode (Wang et al., 2002).

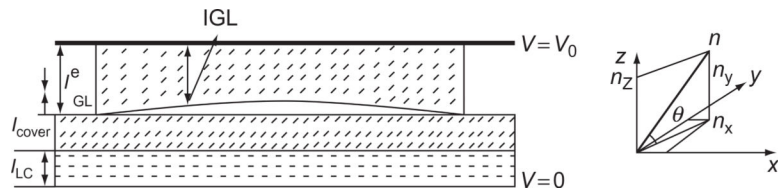


FIGURE 38.

LC lens formed by a plano-concave lens with conductive coating on the plano surface and a flat LC layer (Wang et al., 2004).

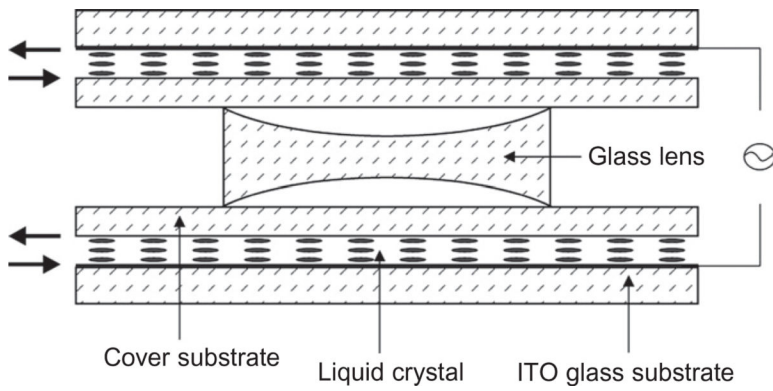


FIGURE 39.

LC lens with two concave surfaces and two LC layers (Wang et al., 2004).

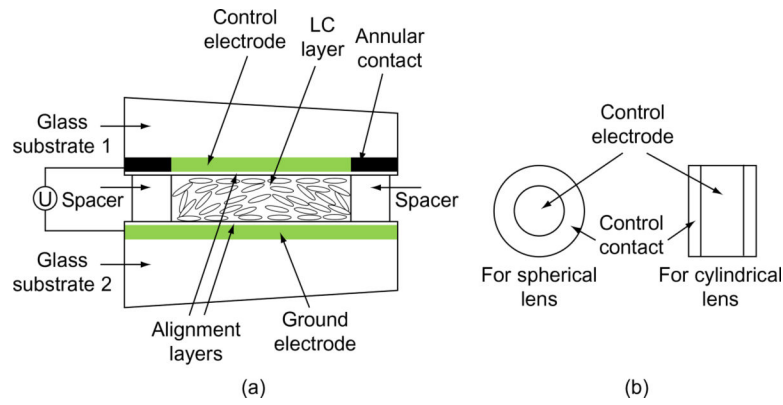


FIGURE 40.

(a) Modal LC lens structure. (b) Resistive electrode patterns for the spherical lens and the cylindrical lens (Naumov et al., 1998).

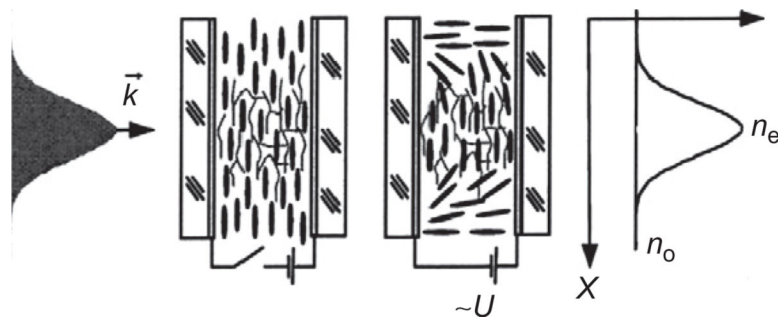


FIGURE 41.

Illustration of the principle of polymer stabilized LC lens fabrication and refractive index distribution with a uniform voltage (Presnyakov & Galstian, 2005).

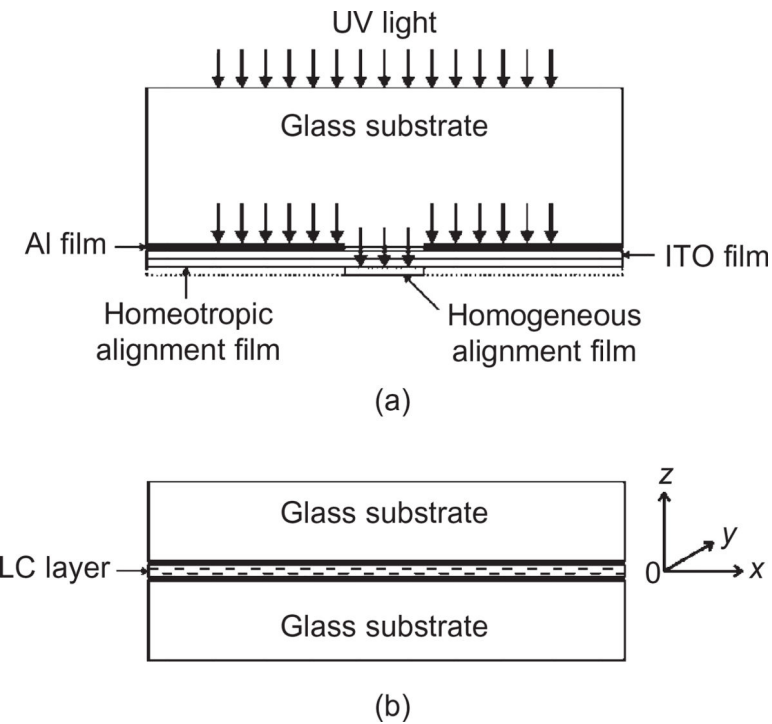


FIGURE 42.

LC microlens formed by patterned molecular orientations on cell walls. (a) Substrate treatment. (b) LC cell (Ye et al., 2006).

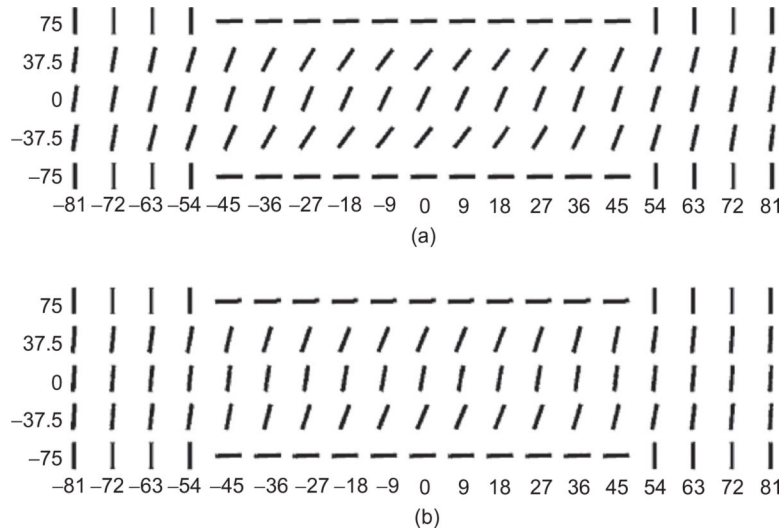


FIGURE 43.

Calculated director orientations in plane $y = 0$ at (a) $V = 0$ and (b) $V = 1$ V (Ye et al., 2006).

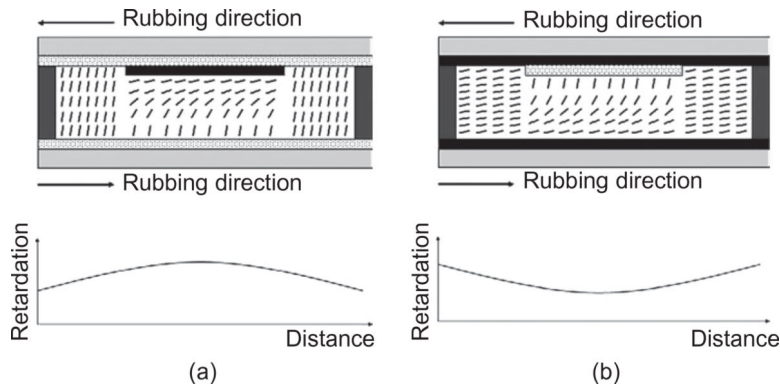


FIGURE 44.

Microlens based on hybrid LC alignment. (a) The convex lens configuration. (b) The concave lens configuration (Cheng, Chang, & Yeh, 2006).

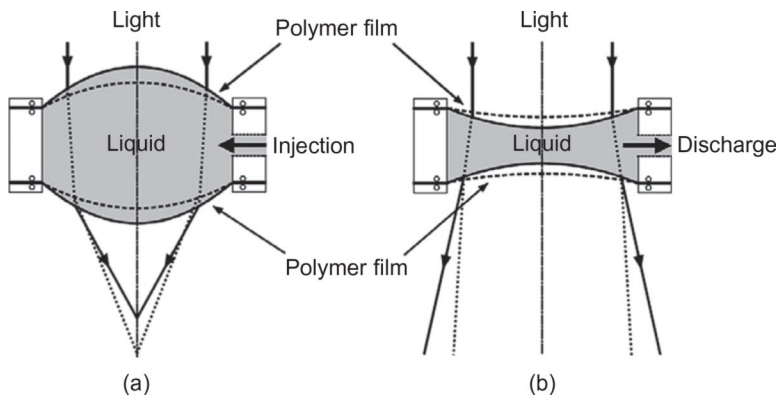


FIGURE 45.

Principle of liquid pressure varifocus lens: (a) biconvex lens and (b) biconcave lens.

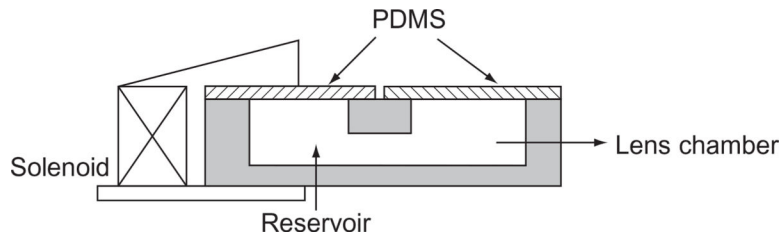


FIGURE 46.

The compact liquid lens actuated by the modified electromagnetic solenoids.

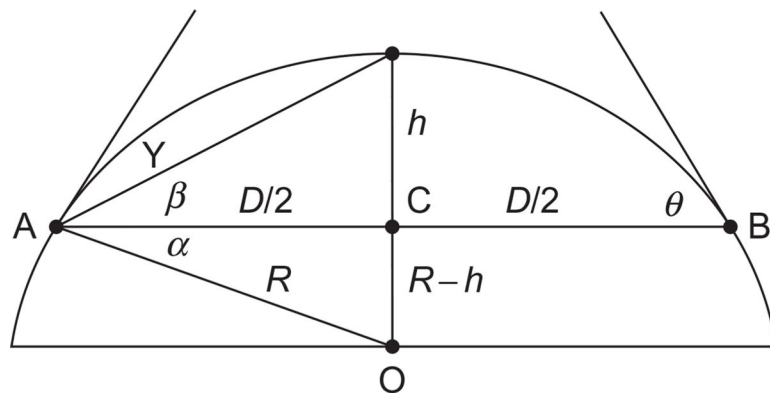


FIGURE 47.

A schematic diagram for the plano-convex lens shape.

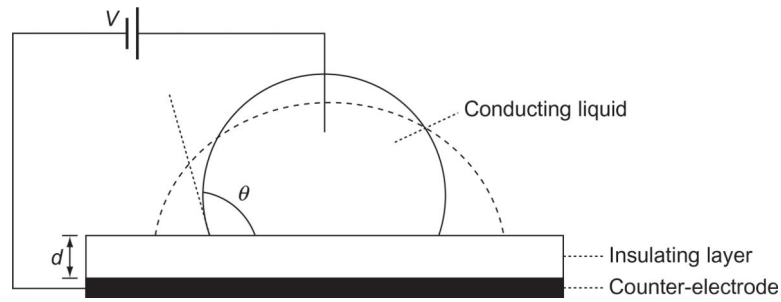


FIGURE 48.

Schematic drawing of an electrowetting experiment. A droplet of a conducting liquid is placed on an insulating layer of thickness d , which is deposited on a metal counter electrode. Application of a potential V between the droplet and the metal electrode changes the free energy of the droplet and results in a decrease of the contact angle θ . The resulting droplet shape is indicated by the dashed line (Minnema et al., 1980).

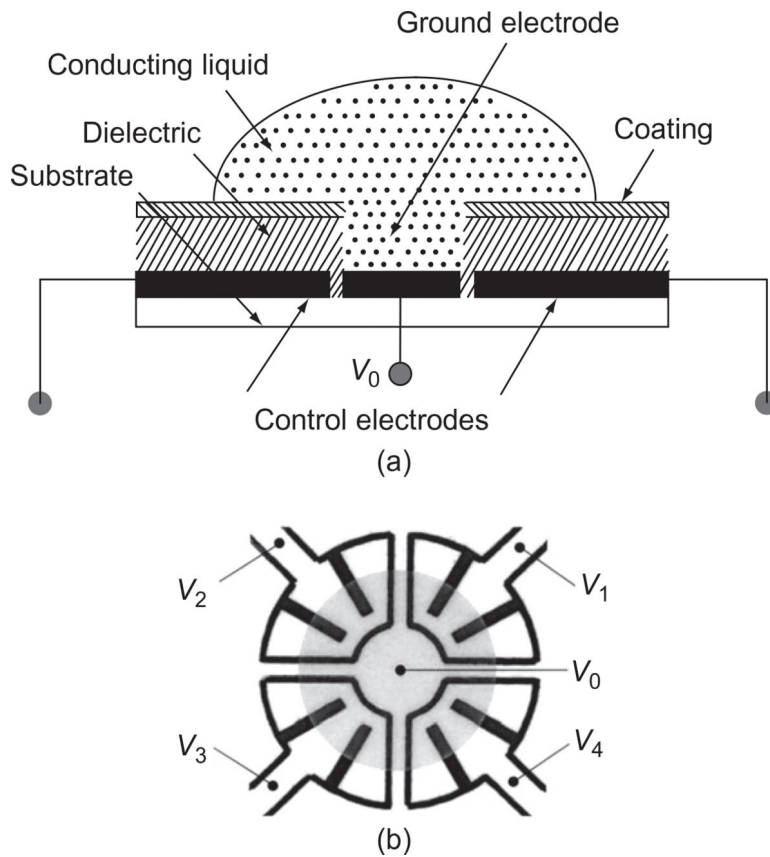


FIGURE 49.

Schematic diagram of the tunable liquid microlens based on the electrowetting effect. (a) Electrode design. Black lines indicate etched areas on ITO. Applied voltages are indicated as V_0 through V_4 . Lightly shaded area represents an approximate droplet position. (b) Device cross section. Voltage applied to the ground electrode is indicated as V_0 (Krupenkin et al., 2003).

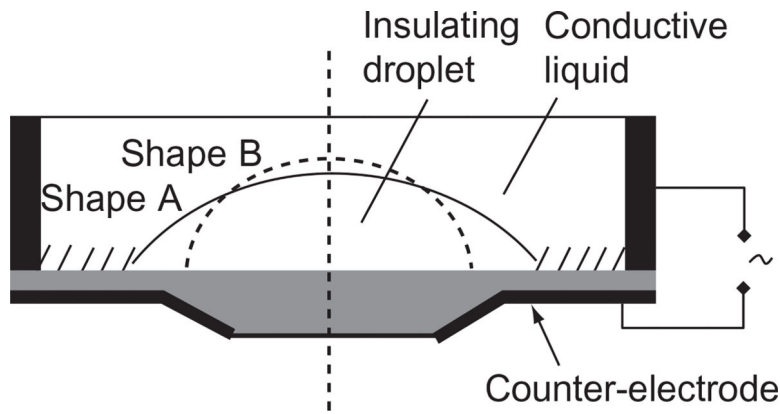


FIGURE 50.

Tunable lens using two immiscible liquids. The cell is filled with a conductive sealing liquid. A drop of an insulating and nonpolar liquid is deposited on the bottom wall, which is made of an insulating and transparent material, in gray. The central disc on the bottom wall surface is hydrophobic, in order to trap the drop. The outer zone (hatched area) is hydrophilic (Berge & Peseux, 2000).

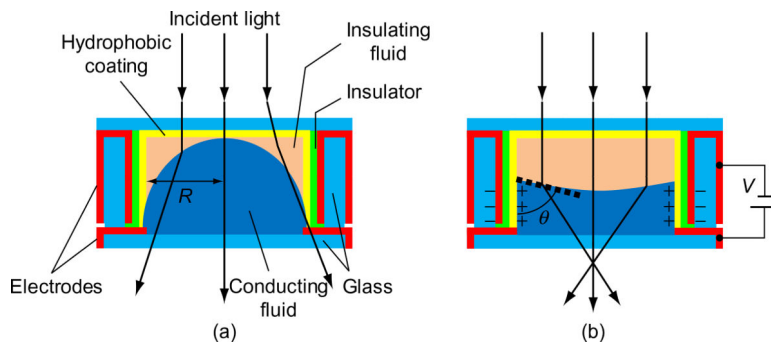
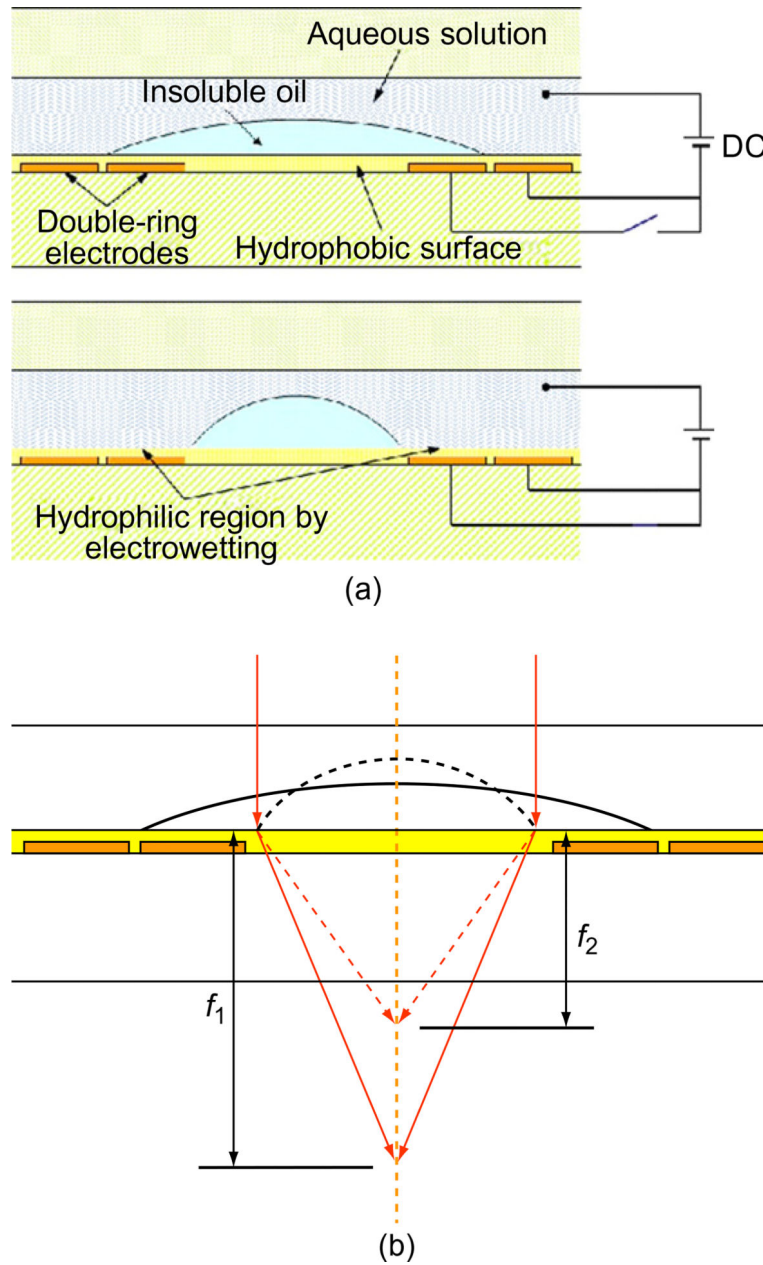


FIGURE 51.

(a) Schematic cross section of a liquid-based variable lens in a cylindrical glass housing. (b) When a voltage is applied, the contact angle of the conducting liquid is changed at the interface of the insulator (Kuiper & Hendriks, 2004).

**FIGURE 52.**

Schematic illustrations of the planar liquid lens design: (a) curvature change of the liquid lens by electrowetting and (b) focal length change of the liquid lens. After the application of a dc voltage, the insoluble oil droplet becomes more curved and the focal length is shortened from f_1 to f_2 (Liu et al., 2008).

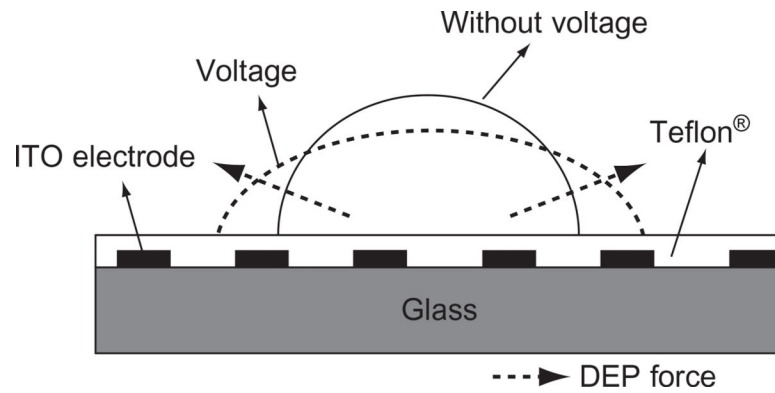


FIGURE 53.

(a) Schematic view of deformation mechanism of a deformable liquid crystal droplet lens (not to scale). (b) Design of concentric ITO electrode of $50\mu\text{m}$ in width and $50\mu\text{m}$ in spacing (Cheng, Chang, & Yeh, 2006).

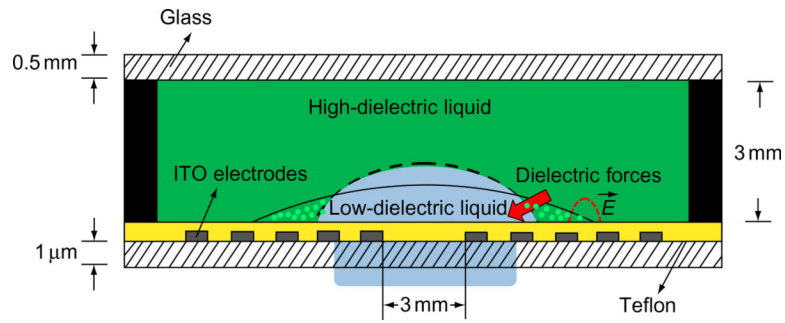


FIGURE 54.

Illustration of a dielectric liquid lens. The droplet shrunk to a new state (dashed line) due to the dielectric force (Cheng & Yeh, 2007).

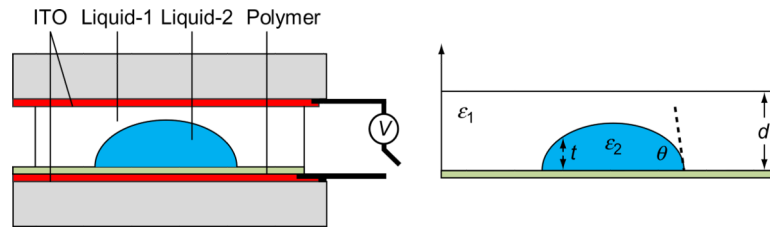


FIGURE 55.

Dielectric liquid lens using two flat electrodes. (a) Side view of the lens. (b) Definition of the parameters (Ren et al., 2008).

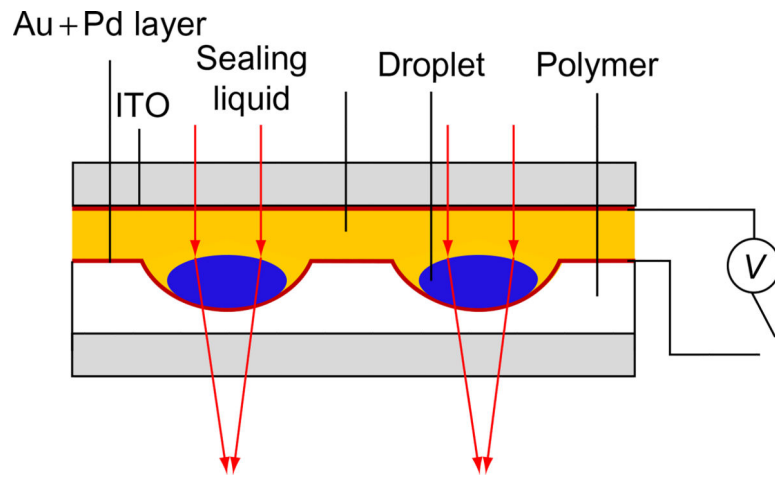


FIGURE 56.

Dielectric liquid lens using a spherical electrode (Xu et al., 2009).

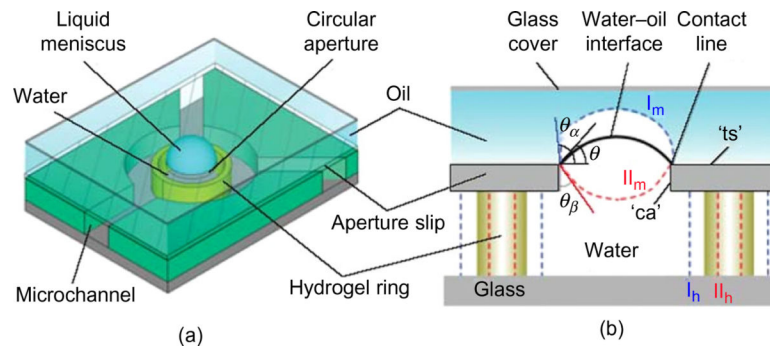


FIGURE 57.

Liquid microlens using stimuli-responsive hydrogel. (a) The water–oil interface forms the liquid microlens. The microchannels allow the flow of fluids to the microlens structure. (b) Smart variable-focus mechanism (Dong et al., 2006).

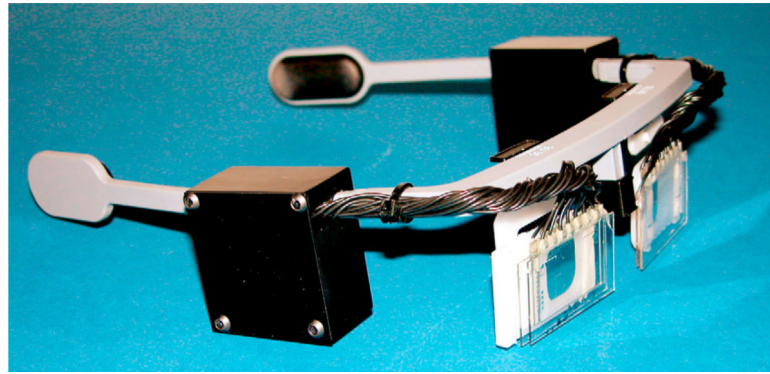


FIGURE 58.

A prototype of the assembled adaptive eyewear whose power can be switched between plano, 1D, and 2D.

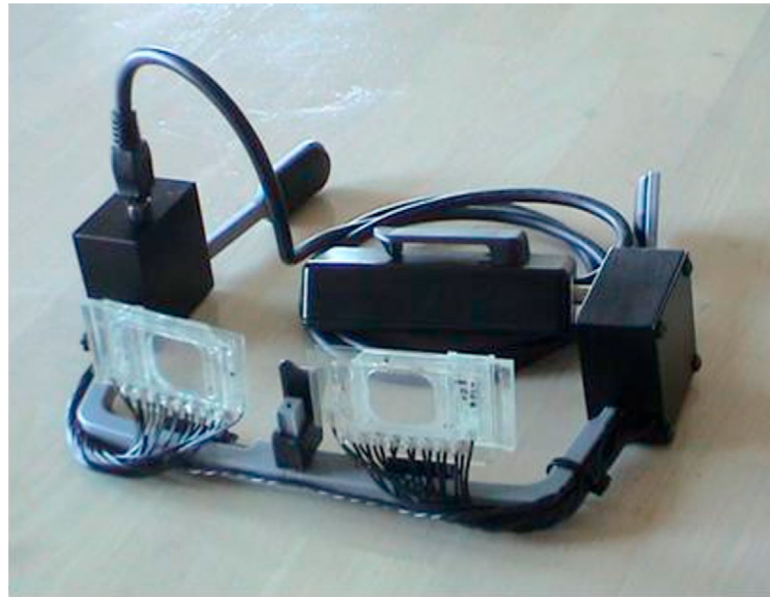


FIGURE 59.

A prototype of the assembled adaptive eyewear whose power can be switched between plano, 2D, and 4D.